CZECH TECHNICAL UNIVERSITY IN PRAGUE
Faculty of Nuclear Sciences and Physical Engineering
Department of Physics

Vacuum Stability of ^{83}Rb/^{83m}Kr Electron Source for the Neutrino Experiment KATRIN

Diploma Thesis

Author: Miroslav Zbořil*
Supervisor: prom. fyz. Drahoslav Vénos, CSc.§
Tutor: Ing. Alojz Kovalík, DrSc.‡

Dubna, Prague and Řež/Prague, 2005–2006

*E-mail: Miroslav.Zboril@gmail.com
§Nuclear Physics Institute, ASCR, Řež/Prague, E-mail: venos@ujf.cas.cz
‡Laboratory of Nuclear Problems, JINR Dubna, E-mail: kovalik@jinr.ru

Prohlášení

Prohlašuji, že jsem svou diplomovou práci vypracoval samostatně a použil jsem pouze podklady uvedené v přiloženém seznamu.

Nemám závažný důvod proti užití tohoto školního díla ve smyslu § 60 Zákona č. 121/2000 Sb., o právu autorském, o právech souvisejících s právem autorským a o změně některých zákonů (autorský zákon).

V Praze dne 12.5.2006

Název práce: Vakuová stabilita elektronového zdroje ^{83}Rb/^{83m}Kr pro neutrinový experiment KATRIN

Autor: Miroslav Zbořil

Obor: Jaderné inženýrství

Druh práce: Diplomová práce

Vedoucí práce: Drahoslav Vénos. ÚJF AV ČR, Řež u Prahy.

Konzultant: Alojz Kovalík. LJAP SÚJV Dubna.

Abstrakt: Předkládaná diplomová práce se zabývá výzkumem vakuové stability radioaktivního zdroje ^{83}Rb/^{83m}Kr zamýšleného jako jeden z monitorovacích nástrojů experimentu KATRIN. Tento typ zdroje bude použit jako neustálá kontrola stability energetické stupnice systému elektronových spektrometrů KATRIN. Ke studiu vakuové stability byly použity dvě metody. Nejdříve byl únik rubidia z neaktivních vzorků zkoumán pomocí analýzy zbytkové atmosféry ultravysokého vakua v SÚJV Dubna. Z rozboru hmotnostních spekter vyplynulo, že žádný únik rubidia ze vzorku nebyl pozorován. Tento výsledek naznačuje, že zamýšlený zdroj ^{83}Rb/^{83m}Kr by mohl být stabilní i v podmínkách ultravysokého vakua. V druhé fázi byl možný únik ^{83}Rb z radioaktivních zdrojů ^{83}Rb/^{83m}Kr, vyrobených v ÚJF Řež, studován metodou jaderné spektroskopie záření gama. Ze změřených aktivit zdrojů vyplynul závěr, že velikost úniku ^{83}Rb je kompatibilní s nulou v rámci jedné standardní chyby. Typická relativní nepřesnost aktivit činila 2 ‰.

Klíčová slova: KATRIN, kalibrace a monitoring, pevný ^{83}Rb/^{83m}Kr zdroj, vakuová stabilita, analýza zbytkové atmosféry, gama spektroskopie

Title: Vacuum stability of ^{83}Rb/^{83m}Kr electron source for the neutrino experiment KATRIN

Author: Miroslav Zbořil

Abstract: This diploma thesis describes the investigation of the vacuum stability of radioactive ^{83}Rb/^{83m}Kr source intended as one of the monitoring tools in the experiment KATRIN. This type of open source is planned to be used in the monitor spectrometer for continuous check of the energy scale stability of the main KATRIN spectrometer. This issue was studied with two methods. Firstly, the Rb release from non-radioactive samples was examined with the help of the residual gas analysis at JINR Dubna. From the analysis of mass spectra it was found that no Rb effect has been observed. Such a result indicate that the intended vacuum evaporated ^{83}Rb/^{83m}Kr source could also be stable in UHV conditions. Secondly, for the studies of the ^{83}Rb escape from radioactive ^{83}Rb/^{83m}Kr samples produced at NPI Řež/Prague the gamma spectroscopy was utilized. From the gamma measurement of the source activities it was concluded that the release of ^{83}Rb was compatible with zero in the frame of one standard uncertainty. The typical relative standard uncertainty of the activities amounted to 2 ‰.

Keywords: KATRIN, calibration and long-term monitoring, ^{83}Rb/^{83m}Kr solid source, UHV compatibility, residual gas analysis, gamma spectroscopy

Contents

1 Introduction

The **Ka**rlsruhe **tri**tium **n**eutrino (KATRIN) experiment is a next-generation tritium beta decay experiment which will improve the ν-mass sensitivity compared to the present direct neutrino mass experiments at Mainz and Troitsk by one order of magnitude. With an estimated ν-mass sensitivity of $0.2\,\mathrm{eV}/c^2$ (90 % C.L.) KATRIN will allow the investigation of the neutrino mass in sub-eV scale, which is of particular interest for particle physics, astrophysics and cosmology. In contrast to other methods such as the search for neutrinoless double beta decay or cosmological ν-mass studies, using large scale structure and cosmic microwave background radiation data, KATRIN will provide a completely model-independent measurement of the ν-mass. The KATRIN result will be based only on kinematic relations and energy-momentum conservation.

The realization of the KATRIN experiment will be a technological challenge being noted for a number of stringent experimental requirements. The energy calibration and long-term monitoring of the energy scale are also of great importance. These tasks will be performed by the use of beta- and gamma ray spectroscopy. For the purposes of the direct energy calibration and the continuous monitoring of the KATRIN spectrometer system suitable electron sources based on atomic/nuclear standards will be utilized.

Among them a solid ^{83}Rb/$^{83\mathrm{m}}$Kr source of conversion electrons from the $^{83\mathrm{m}}$Kr, which is continuously generated by the ^{83}Rb decay, is intended to be used together with the monitor spectrometer as a tool for long-term monitoring of the KATRIN energy scale stability. This type of source was initially investigated at Joint Institute for Nuclear Research (JINR) in Dubna. Since 2005 it is being developed at Nuclear Physics Institute (NPI) ASCR in Řež/Prague by vacuum evaporation of the ^{83}Rb onto suitable backings. One of the issues faced during the development of the ^{83}Rb/$^{83\mathrm{m}}$Kr solid source is its compatibility with the **u**ltra**h**igh **v**acuum (UHV) conditions intended for the KATRIN monitor spectrometer where such a source is to be applied. Obviously, the vacuum stability concerns both isotopes, the parent ^{83}Rb and the daughter $^{83\mathrm{m}}$Kr, but in this work mainly the ^{83}Rb will be considered. For the investigation of the vacuum stability of the ^{83}Rb/$^{83\mathrm{m}}$Kr source two different methods were utilized.

Firstly, the non-radioactive $RbNO_3$ samples—in the form of thin layer prepared by vacuum evaporation—and Rb_2CO_3 samples—in the form of bulk prepared as a drop—were investigated with the help of **r**esidual **g**as **a**nalysis (RGA) at JINR Dubna. The RGA utilizes a **l**inear **q**uadrupole **m**ass **s**pectrometer (LQMS) for determining the partial pressures of volatile species. The gas molecules are ionized and the resulting ions are separated, detected and measured according to their mass-to-charge ratio. Possible escape of the Rb compounds could thus be observed and quantified by the RGA. Secondly, the radioactive ^{83}Rb/$^{83\mathrm{m}}$Kr sources produced at NPI Řež/Prague were examined as well. Gamma spectroscopy was used for extensive testing of the ^{83}Rb and/or $^{83\mathrm{m}}$Kr release from all the sources produced here.

This work describes the RGA release studies of non-radioactive rubidium samples which were performed at JINR Dubna in the period December 2005–February 2006 and were meant as an improvement of the first, rather introductory, series of measurements performed there since August 2004. Further, the examination of four ^{83}Rb/$^{83\mathrm{m}}$Kr sources performed by means of gamma spectroscopy at NPI Řež/Prague is presented.

The thesis is organized as follows. Firstly the basic concepts of the KATRIN experiment are introduced while the emphasis is put on the energy calibration and monitoring methods. The next section discusses in detail the concept of the ^{83}Rb/$^{83\mathrm{m}}$Kr source intended to be used as a monitoring tool of the KATRIN energy scale long-term stability. Further, the RGA release studies of non-radioactive Rb samples in UHV of 10^{-9} mbar at JINR Dubna are summed up.

Then with the help of gamma spectroscopy the ^{83}Rb release from the ^{83}Rb/^{83m}Kr sources is analyzed. Finally, the results of both approaches are compared and the imperfections are discussed. Possible progress of the ^{83}Rb release investigation is discussed as well.

I am indebted to Drahoslav Vénos for his patience, encouragement and help throughout the writing of this diploma thesis. I am also grateful to Alojz Kovalík for his support and help during my stays in Dubna and to Rostislav Mach for supporting the winter 2005/2006 stay. I would like to thank to Otokar Dragoun, Antonín Špalek and Miloš Ryšavý for their helpful ideas and valuable conversations. I wish to express my thanks to Jaromír Kašpar for all the very helpful and stimulating discussions and for his kind help with the computer implementation of the ROOT routines used within this work. All the very helpful conversations with Petr Řepa, Zdeněk Herman and Zbyněk Hůlek are greatly appreciated. I also gratefully acknowledge all the support from Roman Bašta and Jiří Kubáň. I am sincerely grateful to Zdeněk Janout, Ivan Štekl, Jiří Tolar and Vojtěch Petráček for their valuable encouragement and help throughout my studies. I truly appreciate the preparation of samples by Miloslav Vobecký in Prague and by Dmitriy Filosofov in Dubna. I appreciate the collaboration with Alexey Lubashevsky and Lev Perevoshchikov and the help from Anvar Inoyatov and Mahmoud Mahmoud.

Above all, I am indebted to my family and to my amazing Aleksandra and her family for all the support, patience and faith.

Prague, May 12, 2006

2 KATRIN experiment

The Standard Model (SM) of particle physics has long assumed neutrinos to be massless particles, however, the results of ν-oscillation experiments using solar as well as atmospheric neutrinos have provided compelling evidence for flavor transformations of neutrinos (ν-oscillations) and hence for non-zero neutrino masses [1, 2]. These important results have been further confirmed by the observation of neutrino disappearance in experiments using reactor and accelerator neutrinos at long baseline. The parameters of neutrino oscillations, *i.e.* the mass splitting Δm^2_{ij} and mixing amplitudes $\sin^2\theta_{ij}$ of neutrinos are now known to leading order.

Neutrino oscillations imply that a neutrino from one specific weak interaction flavor, *e.g.* a muon neutrino ν_μ, transforms into another weak flavor eigenstate, *i.e.* an electron neutrino ν_e or a tau neutrino ν_τ, while traveling from the source to the detector. The existence of neutrino oscillations requires a non-trivial mixing between the weak interaction eigenstates (ν_e, ν_μ, ν_τ) and the corresponding neutrino mass states (ν_1, ν_2, ν_3) and, moreover, that the mass eigenvalues (m_1, m_2, m_3) differ from each other. Consequently, the experimental evidence for neutrino oscillation proves that neutrinos have non-zero masses. Unfortunately neutrino oscillation experiments are not sensitive to neutrino masses directly.

2.1 KATRIN project overview

The **Ka**rlsruhe **tri**tium **n**eutrino (KATRIN) experiment is a next-generation direct neutrino mass experiment designed to investigate in a model-independent way the fundamental mass scale of neutrinos with sub-eV sensitivity. It combines an ultra-luminous molecular windowless gaseous tritium source with a high resolution electrostatic retarding spectrometer to measure the spectral shape of beta decay electrons close to the tritium endpoint at 18.6 keV (Fig. 1) with un-

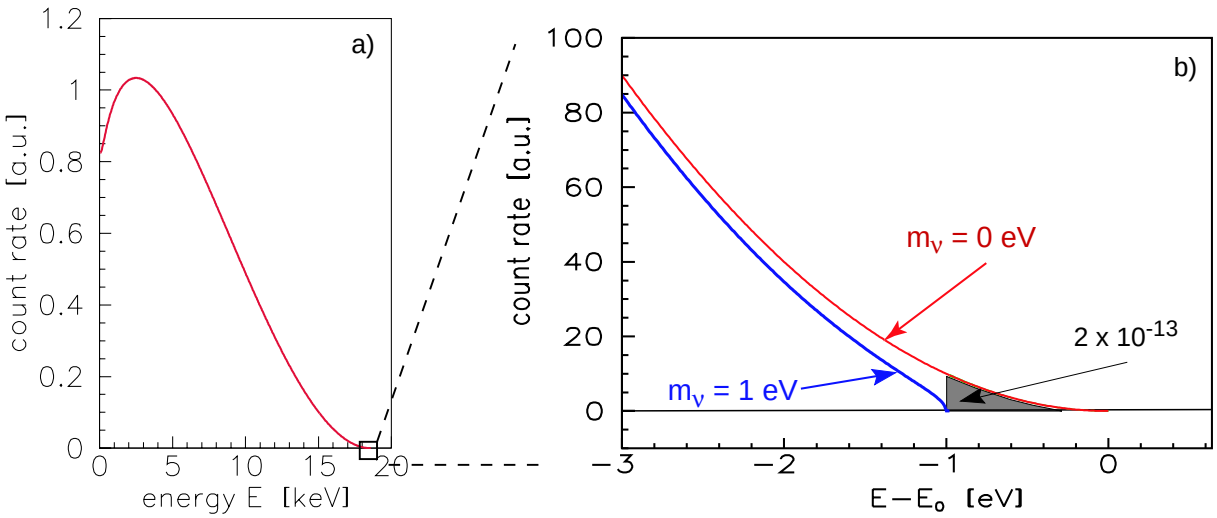

Fig. 1. The electron energy spectrum of tritium β decay $^3\mathrm{H} \rightarrow {}^3\mathrm{He}^+ + e^- + \overline{\nu}_e$ [1]: **(a)** complete and **(b)** narrow region around the endpoint E_0. The β spectrum is shown for neutrino masses of 0 and 1 eV.

precedented precision. If no neutrino mass signal is found, the KATRIN sensitivity after 3 years of measurements is $m(\nu_e) < 0.2\,\mathrm{eV}$ (90 % C.L.); a ν_e-mass signal of $m(\nu_e) = 0.35\,(0.30)\,\mathrm{eV}$ can

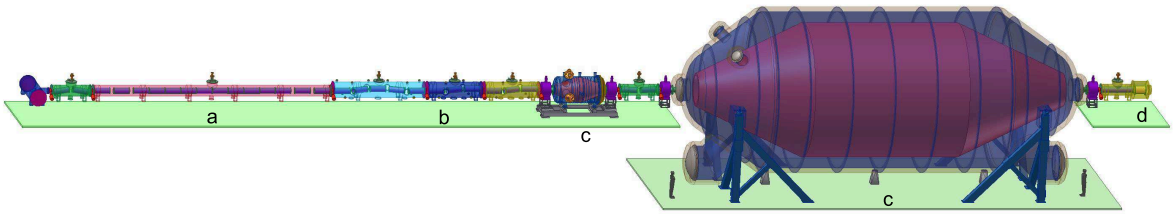

Fig. 2. The 70 m long KATRIN reference setup with its major components: *a)* the windowless gaseous tritium source WGTS, *b)* the transport elements, consisting of an active pumping part and a passive cryotrapping section, *c)* the two electrostatic spectrometers and *d)* the detector for β-counting (not shown is the monitor spectrometer) [1].

be measured with 5 (3) σ evidence. This represents a full order improvement with respect to previous direct neutrino mass experiments—predecessors of KATRIN are Troitsk ($m(\nu_e) < 2.05\,\text{eV}$, 95 % C.L.) and Mainz ($m(\nu_e) < 2.3\,\text{eV}$, 90 % C.L.). It will allow KATRIN to probe all quasi-degenerate neutrino mass scenarios and the full cosmologically relevant neutrino mass range. The experiment is scheduled to start first tritium runs in late 2008. For comprehensive overview of the KATRIN motivations, all the experiment subtasks, ν_e-mass sensitivity considerations as well as an introduction into the theory of beta decay see [1].

The reference setup of KATRIN shown in Fig. 2 corresponds to a $\sim$ 70 m long linear configuration with about 40 superconducting solenoids (the main $\sim$ 70 m long electron beam line), which adiabatically guide β-decay electrons from source to detector.

The experimental configuration of KATRIN can be grouped into following major functional units:

- A high luminosity **w**indowless **g**aseous **t**ritium **s**ource (WGTS) delivering 10^{11} β-decay electrons during the standard operation mode of the experiment – ultra-cold molecular tritium (T_2) gas ($T = 27\,\text{K}$) of high isotopic purity ($> 95\%$) will be injected through a set of capillaries at the middle of the 10 m long WGTS tube. The gas injection pressure p_{in} allows adjustment of the column density ρd.

- An electron transport and tritium pumping section, comprising an *active* differential pumping section and a *passive* cryogenic pumping source – KATRIN sensitivity considerations imply that the tritium flow has to be suppressed by about a factor of 10^{11} between the outlet of the WGTS tube and the entrance of the pre-spectrometer.

- A system of two electrostatic retarding MAC-E-Filters—**m**agnetic **a**diabatic **c**ollimation combined with an **e**lectrostatic **filter**—in a 'tandem setup' with a smaller pre-spectrometer for pre-filtering (a cylindrical tank with the length of 3.38 m and the inner diameter of 1.68 m, working at a fixed retarding energy of approximately 300 eV below the endpoint of the β-spectrum and allowing only electrons with the highest energies to pass into the main spectrometer) and a larger main spectrometer for energy analysis of β-electrons (the diameter of 10 m and the length of 23.3 m analyzing the kinetic energy of electrons with a resolution of 0.93 eV). In a MAC-E-Filter, the isotropic direction of emission of β-electrons at the source is transformed into a broad beam of electrons flying with a

momentum almost parallel to the magnetic field lines. This parallel beam of electrons is energetically analyzed by an electrostatic retarding potential; all electrons having enough energy to pass the electrostatic barrier are re-accelerated and collimated by the upstream spectrometer magnet, electrons with less energy than the retarding potential are reflected, thus the spectrometer acts as an integrating high-energy pass filter.

- A semi-conductor based high-resolution low background detector to count the β-electrons transmitted through the electrostatic filters – downstream of the main spectrometer and separated by a 2-solenoid transport element the electron detector is placed within a detector solenoid, which leaves enough room for an active and passive detector shielding to lower the detector background rate. The detector is a multi-pixel silicon semiconductor detector with ultra-high energy resolution and very thin entrance window.

- A second independent 5 m long beam line—complementing the main beam line—for on-line monitoring of the actual retarding voltage at the main spectrometer, running parallel to the main 70 m long beam line. The monitor beam line comprises the following functional units: *a)* a monitor source emitting monoenergetic electrons in the energy range 17.8–32 keV, *b)* a high resolution MAC-E-Filter (the modified Mainz spectrometer) being fed by the same retarding **h**igh **v**oltage (HV) as the KATRIN main spectrometer and thus providing an on-line monitoring of the retarding HV of the main spectrometer, and *c)* a segmented silicon based PIN-diode array for β-counting.

From thorough considerations of different design requirements [1] it follows that the KATRIN experiment needs to meet the following technical challenges:

- Long term recirculation and purification of tritium on the kCi scale – necessary for the concept of the WGTS.

- 10^{-3} temperature stability at 27 K – in order to keep constant the number of T_2 molecules decaying within the WGTS the T_2 partial pressure and thus the WGTS temperature has to be controlled with high accuracy.

- E**x**treme **h**igh **v**acuum (XHV) of $< 10^{-11}$ mbar in very large volumes of $\approx 1400\,\mathrm{m}^3$ – for the low background rate $\Gamma = 1$ mHz being one of the crucial parameters in the resulting limit on the ν_e-mass limit, reaching and maintaining the XHV conditions in both the pre- and main spectrometers is a must.

- Large number of superconducting magnets (≈ 30) for producing a magnetic field guiding the β-electrons.

- A ppm stability for voltages in the 20 kV range, aim to reach ppm absolute precision as well (see Sect. 2.2).

- Simulations and Monte Carlo studies.

2.2 Energy stability, monitoring and calibration

The determination of the ν_e-mass from the measurement of the tritium β-spectrum near the endpoint by the KATRIN experiment requires for each event the precise knowledge of the energy E_{ret} retarded in the analyzing plane of the main spectrometer. This energy is determined by the

retarding electrostatic potential at the analyzing plane and the scanning potential U_s applied to the source. The high precision spectroscopy of the β-electrons close to the endpoint of tritium at 18 575.0 eV [1] requires a precise absolute calibration of the KATRIN electrostatic spectrometer system. Moreover, as the tritium measurements will take about three years to accumulate the statistics for the announced sub-eV sensitivity the long-term stability of the spectrometer system has to be monitored continuously. In fact, the HV stability check appears to be even more important than the absolute energy calibration: the precise calibration of the spectrometer voltage will be very valuable, of course, but if one would not know about the shift in the energy scale within time, the shift in deduced $m(\nu_e)$ is unavoidable.

2.2.1 Need for HV stability check and energy calibration

To illustrate the precision needed for E_ret the following estimate from [1] (and citations therein) can be used: an unknown smearing of E_ret with the Gaussian variance σ^2 will result in a systematic shift of the squared neutrino mass $m^2(\nu_e)$ as $m^2(\nu_e) = -2\,\sigma^2$. Therefore, requiring the uncertainty of $m^2(\nu_e)$ caused by this smearing to be less than $0.005\,\mathrm{eV}^2$, not only a very high short-term stability of the retarding voltage is needed but also a method to measure it with a 50 mV precision for at least three years data taking. For a retarding voltage of 18.6 kV this corresponds to a long-term relative precision better than 3 ppm. The precise measurement of the scanning voltage U_s which will not exceed 100 V does not represent any problem.

Several methods will be utilized to monitor the retarding potential in the KATRIN experiment to achieve a high degree of redundancy:

- Direct retarding voltage measurement – a high-precision voltage divider will divide the retarding voltage U down to about 10 V, which is then measured with a high-precision digital voltmeter.
- Monitor spectrometer – calibration measurements in the main system cannot take place in parallel to tritium measurements but there is a necessity to monitor the stability of the retarding voltage during tritium runs. The retarding voltage of the main spectrometer will also be supplied to a third electrostatic analyzer of the MAC-E type. The task of this monitor spectrometer is to measure the energy of a well-defined sharp photoelectron- or conversion electron line which is compared to the retarding energy of the KATRIN main spectrometer.
- Direct calibration of the main spectrometer – frequently the spectroscopy of photoelectrons or conversion electrons from suitable sources will be done with the KATRIN main spectrometer to calibrate absolutely the retarding energy E_ret under measurement conditions.

Another very important concepts to be used for the energy calibration and monitoring in the KATRIN experiment are the helium-tritium atomic mass difference $\Delta M\left({}^3\mathrm{He} - {}^3\mathrm{H}\right)$—intended to be compared with the endpoint energy E_0 obtained by fitting the measured tritium β spectrum—and the electron guns (to be employed for various KATRIN systematics investigations like spectrometer system work function measurements *etc.*).

2.2.2 Suitable electron sources

In order to calibrate the KATRIN retarded energy absolutely and to check the stability of the high-voltage measurement setup, energetically well-defined and sharp electron sources are

needed. The electron energy should be defined by atomic or nuclear standards. Three kinds of sources will be applied:

Conversion electrons from ^{83m}Kr – the K-conversion electron line of the 32 keV transition in ^{83m}Kr (denoted K-32) has an energy of 17.8 keV and a natural width of 2.8 eV (FWHM) [3]. As this energy differs by only 0.8 keV from the endpoint energy of the tritium β-spectrum, the K-32 line is well suited for the tasks of absolute calibration and monitoring of the spectrometer energy scale. The half-life of ^{83m}Kr is only 1.83 h. On one side this avoids any danger of a long-term contamination of the apparatus, but this also means that replenishment of ^{83m}Kr is necessary for studies exceeding several hours. The gaseous ^{83m}Kr will be utilized to check the properties of the WGTS as well as for absolute energy calibration of the whole apparatus. For the latter task the energy of this conversion line has to be known with high precision. Previous measurement of the K-32 conversion electron energy of $17\,821.4 \pm 2.0$ eV [4] (gaseous ^{83m}Kr used) is not sufficiently accurate for the KATRIN experiment.

For the ^{83m}Kr atoms in gaseous form, the kinetic energy $E_{e,\mathrm{kin}}$ of the K-32 conversion electrons measured by the KATRIN spectrometer system is given by

$$E_{e,\mathrm{kin}} = E_\gamma + E_{\gamma,\mathrm{rec}} - E^{\mathrm{vac}}_{\mathrm{bin}}(K) - E_{e,\mathrm{rec}}(K) - (\phi_{\mathrm{spectr}} - \phi_{\mathrm{source}}) - C\,, \qquad (1)$$

where E_γ is the γ-ray energy, $E^{\mathrm{vac}}_{\mathrm{bin}}(K)$ is the binding energy of K-shell electrons related to the vacuum level, $E_{\gamma,\mathrm{rec}}(K) = 0.006\,7$ eV is the energy of the recoil atom after γ-ray emission and $E_{e,\mathrm{rec}} = 0.120$ eV is the energy of the recoil atom after emission of the conversion electron. ϕ_{spectr} and ϕ_{source} are the work functions of the retarding electrode of the main spectrometer and of the source, respectively. In the case of a mixture of both ^{83m}Kr and T_2 within the WGTS, the term C will account in addition for possible space and surface charges within the gaseous source. Inserting the latest values, namely $E_\gamma = 32\,151.7 \pm 0.5$ eV [5] and $E^{\mathrm{vac}}_{\mathrm{bin}}(K) = 14\,327.26 \pm 0.04$ eV [6], into Eq. 1 one obtains $E_{e,\mathrm{kin}} + (\phi_{\mathrm{spectr}} - \phi_{\mathrm{source}}) + C = 17\,824.33 \pm 0.50$ eV.

The concept of the ^{83m}Kr source will be applied in different physical states:

- gaseous ^{83m}Kr source – for a precise determination of the distribution of the electric potential within the WGTS,
- condensed ^{83m}Kr source – a quench-condensed film of the sub-monolayer thickness on a **h**ighly **o**rdered **p**yrolytic **g**raphite (HOPG) substrate will be used for different systematic investigations as well as for calibration purposes,
- solid ^{83}Rb/^{83m}Kr source – one way of avoiding the necessity to repeat the ^{83m}Kr film quench-condensation every few hours due to the short half-life of ^{83m}Kr is the solid ^{83}Rb/^{83m}Kr electron source.

The UHV compatibility of the third type of source is the main subject of this work; for a detailed overview of its properties see Sect. 3.

Photoelectrons from ^{241}Am/Co – providing a sharp electron source with an energy very close to the endpoint energy of the tritium β-spectrum is being developed: γ radiation from a ^{241}Am source hits a thin cobalt foil. The photoelectrons ejected by $26\,344.6 \pm 0.2$ eV [7] γ-ray photons of ^{241}Am from the atomic K-shell of metallic Co with binding energy $E^{\mathrm{F}}_{\mathrm{bin}}(K)$

of 7 708.78 ± 0.02 eV [8] have a kinetic energy E_{kin} measured by the KATRIN spectrometer system as

$$E_{e,\mathrm{kin}} = E_{\gamma} - E^{\mathrm{F}}_{\mathrm{bin}}(K) - E_{e,\mathrm{rec}} - \phi_{\mathrm{spectr}}\,, \tag{2}$$

where E_{γ} is the γ-ray energy, $E^{\mathrm{F}}_{\mathrm{bin}}(K)$ is the binding energy of K-shell electrons related to the Fermi level, $E_{e,\mathrm{rec}} < 0.2\,\mathrm{eV}$ is the energy of the Co recoil atom after photoelectron emission, and ϕ_{spectr} is the work function of a retarding electrode of the main spectrometer. This $E_{e,\mathrm{kin}}$ is conveniently close to the endpoint of the tritium β-spectrum. The features of the ^{241}Am/Co photoelectron source can be summarized as:

- the energy of monitoring photoelectrons, 18 636 eV differs from the tritium endpoint E_0 only by about 60 eV and the calibration line will be *above* the β-spectrum,
- the recoil energy and the natural width of exciting γ-rays together with its Doppler broadening at 300 K are less than 0.02 eV, *i.e.* completely negligible for this purpose,
- the natural width of atomic K-shell in Co is 1.28 eV,
- the ^{241}Am half-life of 432 y is practical for long-term monitoring,
- the ^{241}Am/Co source may suffer by physical-chemical changes of the binding energy. Differences of the binding energies of the Co metal component and possible Co oxides are in the range of 1.9–2.1 eV. Photoelectrons corresponding to the metal Co component originate with higher energy than the ones corresponding to Co oxide states. The differences are both well described and observable in the monitor spectrometer. Moreover, the effect may be suppressed by ion etching of the Co foil.

Auger electrons from ^{109}Cd – another useful monitoring source could be ^{109}Cd, decaying by electron capture into ^{109}Ag and emitting KL_2L_3 Auger electrons of the energy 18 511.7 ± 1.3 eV for ^{109}Cd in a particular chemical state.

2.2.3 Monitor spectrometer

For KATRIN the existing Mainz spectrometer upgraded into a high resolution spectrometer with the energy resolution of 1 eV. The idea is to apply the retarding voltage of the KATRIN main spectrometer also to this new monitor spectrometer (Fig. 3). A well-defined electron source will then be measured by varying the voltage of the electron source allowing practically continuous monitoring of retarding voltage. Such low voltages well below 1 kV can be measured very precisely and reliably. The work functions of the monitor spectrometer and the main spectrometer are very similar (practically identical) as in both cases stainless steal under XHV conditions is used. Absolute calibration additionally requires the precise knowledge of the parameters of both sources and the potential distribution in the analyzing plane of both spectrometers. Electron sources which may fulfill the above requirements are the ^{241}Am/Co photoelectron source, the quench-condensed $^{83\mathrm{m}}$Kr source or the solid ^{83}Rb/$^{83\mathrm{m}}$Kr source.

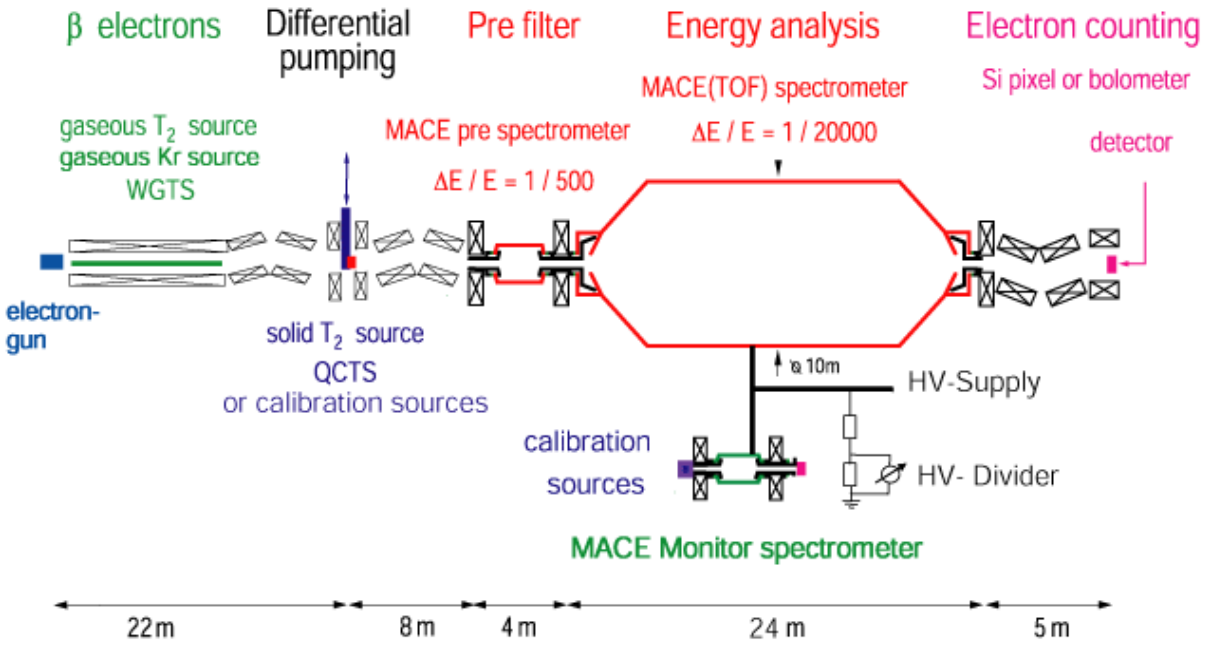

Fig. 3. Setup of the monitor spectrometer beam line—complementing the main beam line—with a calibration source following an atomic/nuclear standard and fed with the main spectrometer retarding potential [1].

3 Solid ^{83}Rb/^{83m}Kr electron source

3.1 Motivation

In the previous section it was stated that one of the methods intended for the monitoring and calibration of the KATRIN spectrometer system will be the use of conversion electrons from ^{83m}Kr. This concept will be applied in three different physical states, as a gas, as a quench-condensed film of the sub-monolayer thickness and as a solid ^{83}Rb/^{83m}Kr source. The latter one avoids the necessity to repeat the ^{83m}Kr film quench-condensation every few hours due to the short half-life of ^{83m}Kr. ^{83}Rb decays with a half-life of 86 days, thereby continuously generating ^{83m}Kr (Fig. 4). Such a source will be more convenient for handling due to its compactness.

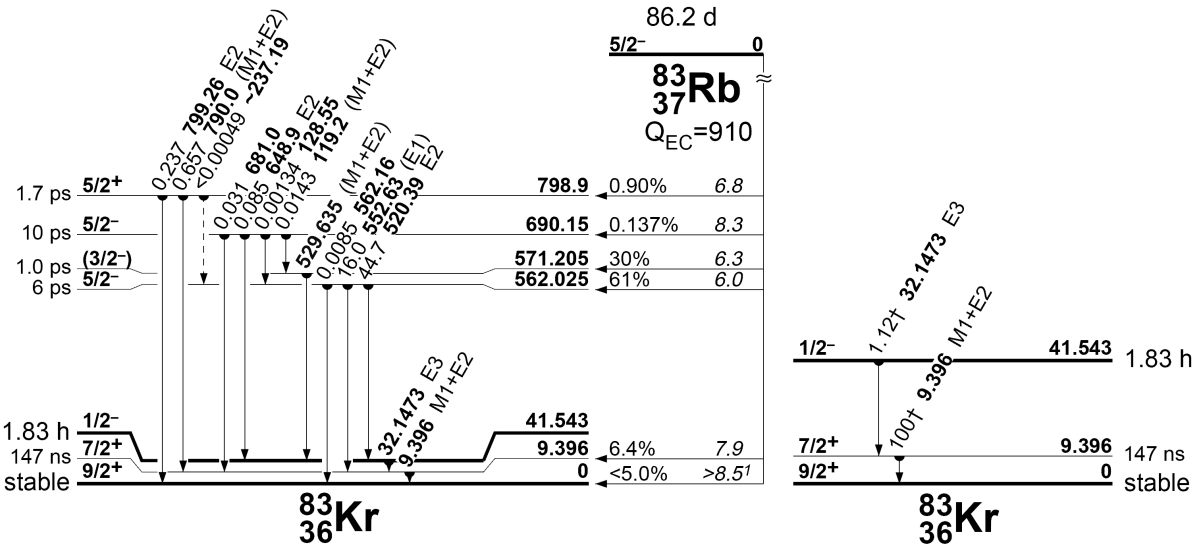

Fig. 4. Decay schemes of ^{83}Rb and ^{83m}Kr [9]. The ^{83}Rb (half-life 86.2 d) decays by pure electron capture (left scheme) with a branching ratio of 77.9 % into the short lived isomeric state ^{83m}Kr (1.83 h). Detail on the right side shows its 32 (intensity 0.055 %, multipolarity E3) and 9.4 keV (4.9 %, M1+E2) gamma transitions.

On the other hand, it is an open source and thus any ^{83}Rb release into the vacuum should be avoided. Due to the long half-life the released ^{83}Rb would increase the background of the KATRIN detectors. For this reason, this ^{83}Rb/^{83m}Kr is not intended for the use within the main KATRIN spectrometer system, but it will be placed in the monitor spectrometer (Sect. 2.2.3) and will serve for the continuous monitoring of the high voltage stability. It is not considered to use this source for energy calibration purposes as the influence of possible chemical effects [10]—production technique, source backing material, residual atmosphere, surface shifts—on the K-32 conversion line energy seems to be inevitable and difficult to investigate. The aim is to assure a reliable long-term stability of the K-32 line energy and to minimize the escape of ^{83}Rb and ^{83m}Kr into the environment before their decay.

The idea of the solid ^{83}Rb/^{83m}Kr source was introduced in the works [11] (KLL and LMX Auger spectra from the ^{83}Rb decay) and [12] (conversion electron investigation of the 9.4 keV transition in ^{83m}Kr decays) where the authors have used the electrostatic spectrometer ESA 50 (JINR Dubna) operated at the vacuum level of 10^{-6} mbar. Here the radioactive ^{83}Rb sources

(activities of $\simeq$ 4.5 MBq) were prepared in the form of rubidium nitrate $^{83}RbNO_3$. A shift of about 13–15 eV of the electron lines energies was found in both works, resulting probably from the shifts of the electron binding energies in ^{83m}Kr atoms generated in the solid source; the electron binding energies in solid ^{83m}Kr could be lower than those for free atoms due to solid-state effects.

For the KATRIN monitoring purposes the activity of the source is planned to be of such a level (up to $\approx$10 MBq) that the one monitoring procedure would take just several minutes. Here the ^{83m}Kr release into the UHV of the monitor spectrometer plays a role – the release would have to be compensated by the accordingly higher activity.

3.2 Main features

The source is intended to be in the form of a thin film prepared by vacuum evaporation onto the HOPG or metal backing of the area of $\simeq 1\,cm^2$. The amount of the ^{83}Rb necessary for the calibration source of activity 10 MBq ($\simeq 0.015\,\mu$g) is by about one order of magnitude less than the amount which would cover the backing with one homogenous monolayer of the material (thickness of $\simeq$ 0.4 nm, area of $1\,cm^2$ *i.e.* weight of the material $\simeq 0.133\,\mu$g). Thus the ^{83}Rb atoms occur in 'islands' (clusters) adsorbed onto the backing. According to a high reactivity of Rb, the ^{83}Rb on the backing is never found in a pure metallic form, rather in the form of some compound(s) reflecting the chemical environment of the source. In addition, during the vacuum evaporation procedure various compounds (oxides *etc.*) spontaneously cover the backing, creating so additional layers on its surface and possibly reacting with Rb compounds. The coverage of the sample with some layers of residual gases is unavoidable—after several tens of hours [13]—even in the in the XHV of $\approx 10^{-11}$ mbar of the monitor spectrometer thus actually a mixture of compounds is always present. Besides the processes of adsorption and desorption, more complicated atomic processes as the surface diffusion, interdiffusion, nucleation and binding [14] can occur.

Obviously, it is desirable to capture both the ^{83m}Kr and ^{83}Rb within the solid ^{83}Rb/^{83m}Kr source:

- the conversion electrons created in an ^{83m}Kr atom escaped from the source are not situated in the right place defined for the source position and thus are useless for the energy calibration,
- the escape of the ^{83m}Kr atoms would have to be compensated by a higher activity of the calibration source,
- a possible release of ^{83}Rb compounds from the source into the UHV or XHV of the monitor spectrometer will naturally reduce the available source activity [15] and increase the background in the electron spectra.

Anyhow, virtually immediately (within $\sim 10^{-10}$ s or less) after the disappearance of a proton in the ^{83}Rb nucleus during the electron capture the rearrangement of the electron shells occurs and the atom behaves chemically as the ^{83m}Kr [16]. Thus the aim is actually to capture a very weakly interacting noble gas in a thin layer adsorbed on a solid. On the other hand, the arrangement of atoms/molecules can possibly support the ^{83m}Kr capture inside the source.

The basic properties of the elements $_{36}$Kr and $_{37}$Rb are summarized in Tab. 1. From their nature (Kr – a noble gas, Rb – an alkali metal) it follows that these two elements are very

different concerning their properties and behavior: Kr has very weak inter-atomic forces of attraction and consequently very low melting point and boiling point, Rb is a highly reactive and easily surface ionized low-density metal igniting spontaneously in air, reacting violently in water and is never found in elemental form in nature. Metallic Rb has a rather high vapor pressure (P_{vap}) in comparison with other elements [17], however, no vapor pressure data were found for *e.g.* Rb oxides. Kr being a gas has still higher P_{vap}. The electron configuration of these two elements differ by one $5s$-electron ('Rb = [Kr] $5s^1$', Kr having fully filled s and p electron shells). For Rb the energetically preferred state of achieving a filled electron shell is to lose one electron to form a singly charged positive ion, thus Rb easily reacts mainly with the elements of the groups 17 (VIIA, Halogens) and 16 (VIA, Chalcogens)—elements of both groups willing to acquire so the noble gas configuration—creating various compounds of halides (RbX, X = F, Cl, Br, I), oxides (RbO_2, Rb_2O, Rb_2O_2, Rb_2O_3), chalcogenides (Rb_2X, X = S, Se, Te), their salts *etc.* [18, 19].

3.3 Current state

In August 2003 the investigation of the UHV compatibility of non-radioactive Rb solid samples has been started with the help of the residual gas analysis at JINR Dubna. The results of these first measurements are presented in Sect. 4 together with the newest results obtained during winter 2005/2006.

Since 2005 the production of non-carrier ^{83}Rb/$^{83\mathrm{m}}$Kr sources proceeds at NPI Řež/Prague. The production of the ^{83}Rb activity is accomplished in collaboration with the Department of radiopharmaceuticals at NPI Řež/Prague on the U-120M cyclotron facility via reaction $^{\mathrm{nat}}\mathrm{Kr}(p, x\,n)^{83}\mathrm{Rb}$ using a krypton gas target. The pressurized krypton gas is exposed to the external proton beam for several hours. Mixture of rubidium isotopes is then washed out of the target chamber by water. The elution efficiency of ^{83}Rb from the target amounts $> 90\,\%$. After the chemical treatment the ^{83}Rb water solution is obtained. For the vacuum evaporation of ^{83}Rb the commercial BAL-TEC MED 020 coating system [20] is used. To achieve the vacuum level of $\approx 10^{-5}$ mbar inside the coating chamber a turbomolecular pump is utilized. The vacuum evaporation efficiency is about 6 %.

The samples are being prepared in the forms of ^{83}RbOH and recently ^{83}RbNO$_3$ as well. According to [16, 21, 22] the overall process of the ^{83}Rb vacuum evaporation (in the ^{83}RbNO$_3$ form) and the consequent storage on air can be described as follows:

$$\underbrace{2\,\mathrm{RbNO_{3\,(s)}}}_{\text{vac. evap. boat}} \xrightarrow{T} \underbrace{2\,\mathrm{Rb_2O_{\,(s)}}}_{\text{adsorp. on backing}} + 2\,\mathrm{NO_{2\,(g)}} + \mathrm{O_{2\,(g)}}\,, \tag{3}$$

$$\mathrm{Rb_2O_{\,(s)}} + \underbrace{\mathrm{H_2O_{\,(g)}}}_{\text{air humidity}} \rightarrow 2\mathrm{RbOH_{\,(s)}}\,, \tag{4}$$

$$2\,\mathrm{RbOH_{\,(s)}} + \underbrace{\mathrm{CO_{2\,(g)}}}_{\text{air, resid. atm.}} \rightarrow \mathrm{Rb_2CO_{3\,(s)}} + \mathrm{H_2O_{\,(g)}}\,, \tag{5}$$

$$\mathrm{Rb_2CO_{3\,(s)}} \xrightarrow{T} \mathrm{Rb_2O_{\,(s)}} + \mathrm{CO_{2\,(g)}}\,, \tag{6}$$

$$\mathrm{Rb_2O_{\,(s)}} \xrightarrow{T} 2\,\mathrm{Rb_{\,(s)}} + \frac{1}{2}\,\mathrm{O_{2\,(g)}}\,. \tag{7}$$

Reaction 3 shows the thermal decomposition of the rubidium nitrate during the vacuum evaporation (Ta boat temperature $\simeq 800$°C) and consequent condensation of rubidium onto the

backing in the form of rubidium oxide. Further, as the samples are usually stored on air, reactions 4 and 5 describe the creation of rubidium hydroxide and carbonate via atmospheric water- and carbon oxide vapors, respectively. Moreover, even the usual UHV residual atmosphere contains a considerable amount of CO_2 [13] thus the reaction of Rb compounds with that are probable in UHV conditions as well. Reactions 6 and 7 describe the possible thermal decomposition of rubidium carbonate and consequently oxide, respectively, when the sample is heated to sufficient appropriate temperatures (cf. Tab. 2). However, as it is not definite that all the ^{83}Rb atoms undergo the whole 'sequence' of reactions 3–5 there is always a mixture of Rb compounds on the backing rather one specific compound, which complicates the problem further. All the sources produced up to now use the aluminum backing.

The ^{83}Rb/^{83m}Kr sources are studied with the help of gamma spectroscopy (Fig. 4: 520, 529 and 552 keV from ^{83}Rb and 9.4 and 32 keV from ^{83m}Kr) and by L_1-9.4 conversion electron measurements in the electrostatic spectrometer ESA 12 (NPI Řež/Prague). The investigation of the ^{83}Rb escape from four sources designated as S4, S7, S8 and S9 is presented in Sect. 5.

The ^{83m}Kr conversion electrons from the source S4 were measured at Institute of Physics (IP) Mainz in June 2005 using the MAC-E-Filter spectrometer [23]. The scans of the ^{83m}Kr K-32, L-9.4 and L-32 lines were performed in UHV of $\approx 10^{-9}$ mbar. All the lines were clearly observed with no disturbing background. Source quality seemed to be superior to monitor the energy scale. On the other hand, on the basis of the K-32 line spectra it was estimated that just 6.6 % of ^{83m}Kr was being kept within the ^{83}Rb/^{83m}Kr source until its decay.

There are three different ways how a better capture of the ^{83m}Kr inside the solid source could be achieved:

- the use of some another Rb compound besides $RbNO_3$ and RbOH which would provide such a chemical environment for the ^{83m}Kr atoms that would not let them escape – a lot of factors can play a role in the resulting mixture inside the solid source like *e.g.* a temperature, pressure and chemical environment during the vacuum evaporation preparation of the sources, chemical treatment after the preparation, storage on air with a certain level of humidity *etc.*,
- 'over-coating' of the vacuum-evaporated source with a thin layer of some suitable compound,
- cooling of the solid source.

The first way seems to be the most efficient and the easiest to handle as no covering (which creates additional layers to be passed by the K-32 conversion electrons) nor cooling (adsorption of compounds coming from the residual UHV atmosphere is probable) would be necessary, however, the influence of the solid-state effects on the resulting K-32 conversion electron energy seems to be inevitable and have to be investigated thoroughly. A few properties of the relevant (possibly encountered in the processes described above) Rb compounds are summarized in Tab. 2, however, rather than thermodynamics (describing bulk volumes) the theory of thin layers (films) on solids has to be considered here.

Tab. 1. Overview of main Kr and Rb properties [9, 17, 18, 24].

Property, quantity	Unit	Kr	Rb
General			
Name, symbol, atomic number		Krypton, Kr, 36	Rubidium, Rb, 37
Atomic mass	u	83.798(2)	85.467 8(3)
Group		18 (VIIIA) – Noble gases: ($_2$He, $_{10}$Ne, $_{18}$Ar, **$_{36}$Kr**, $_{54}$Xe, $_{86}$Rn)	1 (IA) – Alkali metals: ($_3$Li, $_{11}$Na, $_{19}$K, **$_{37}$Rb**, $_{55}$Cs, $_{87}$Fr)
Period, block		4, p	5, s
Characteristics		colorless, odorless, tasteless, nontoxic, nonflammable inert gas	silvery-white, soft, highly reactive metal
Atomic properties			
Electron configuration		[Ar] $3d^{10}4s^24p^6$	[Kr] $5s^1$
Shell structure		2, 8, 18, 8	2, 8, 18, 8, 1
Oxidation states		0 $^{(*)}$	1 (strong base)
Electron affinity	kJ mol^{-1}	–	46.885
Ionization energies (1., 2., 3.)	eV	14.00, 24.36, 36.95	4.18, 27.29, 40.01
Electronegativity (Pauling)		3.00	0.82
Atomic radius (covalent, ionic (Pauling), metallic)	pm	189, 169, –	216, 148, 243
Physical properties $^{(\dagger)}$			
Standard state at (298 K)		gas	bcc crystalline solid
Density	g cm^{-3}	3.708×10^{-3} (293 K)	1.532 (293 K)
Molar volume	cm^3	27.99	55.76
Melting point	K (°C)	115.79 (−157.36)	312.46 (39.31)
Boiling point	K (°C)	119.93 (−153.22)	961 (688)
Critical temperature	K (°C)	209.4 (−63.7)	2 093 (1 820)
Enthalpy of fusion	kJ mol^{-1}	1.638	2.192
Enthalpy of vaporization	kJ mol^{-1}	9.029	72.216
Enthalpy of atomization	kJ mol^{-1}	0	86
Specific heat capacity (298 K)	J g^{-1} K^{-1}	0.248	0.363
Vapor pressure	mbar	4×10^2 (116 K)	1.56×10^{-6} (312 K)
Nuclear properties			
Naturally occurring isotopes, their rel. atomic mass [u] $^{(\bullet)}$, absolute and relative natural abundance [%]		78, 77.92, 0.35(1), 0.6 80, 79.92, 2.28(6), 4.0 82, 81.91, 11.58(14), 20.3 83, 82.91, 11.49(6), 20.2 84, 83.91, 57.00(4), 100.0 86, 85.91, 17.30(22), 30.4	85, 84.91, 72.17(2), 100.0 87, 86.91, 27.83(2), 38.6

$^{(*)}$ Krypton is considered to be chemically inert, however, *e.g.* in krypton fluorine KrF_2 its oxidation number is 2. $^{(\bullet)}$ Here the columns show the designation of the isotope, rounded value of its relative atomic mass [u] and absolute and relative natural abundance [%].

Tab. 2. Overview of several relevant properties of selected Rb compounds [9, 18, 19, 22, 24, 25, 26, 27, 28].

Property	Unit	Rb compounds						
		Rb Rubidium	RbOH hydroxide	RbO_2 superoxide	$RbNO_3$ nitrate	Rb_2O oxide	Rb_2O_2 peroxide	Rb_2CO_3 carbonate
Property								
Molecular mass [(*)]	u	85.5	102.5	117.5	147.5	186.9	202.9	230.9
Density (298 K)	$g\,cm^{-3}$	1.53	3.20	3.8	3.11	3.72	3.65	3.47
Melting point	°C	39	301	432	312	400^{dec}	570	$1\,759^{dec}$
Boiling point	°C	688		$1\,157^{dec}$	578		$1\,011^{dec}$	
Vapor pressure	10^{-6} mbar	1.56 (312 K)	no data found, however, RbX (X = F, Cl, Br, I) have by $\approx 10^2$ lower P_{vap} (at $\sim 1\,300$ K) than metallic Rb					
Molecules (1 ML) per cm^2	$10^{14}\,cm^{-2}$	4.88	7.07	7.24	5.44	5.24	4.90	4.34
1 ML thickness	nm	0.452	0.376	0.372	0.429	0.437	0.452	0.480
1 ML weight	$10^{-7}\,g\,cm^{-2}$	0.69	1.20	1.41	1.33	1.63	1.65	1.67
Ioniz. energy (1st)	eV	4.18			8.89	4.63		

[(*)] For the exact molecular masses taking the two Rb naturally occurring isotopes into account see Tab. 7. ^{dec} = decomposes, ML = monolayer.

4 JINR Dubna: residual gas analysis

As mentioned in Sect. 3.3, the investigation of the UHV compatibility of the non-radioactive Rb solid samples via the **r**esidual **g**as **a**nalysis (RGA) has started at JINR Dubna in August 2003. This section describes the RGA measurements studying the possible Rb escape in the form of any of its compounds. Firstly, the basic notions of the **l**inear **q**uadrupole **m**ass **s**pectrometer (LQMS) will be shortly reviewed as the LQMS actually represents the key part of any RGA [1]. From a number of various mass spectrometers being used today only the LQMS will be considered here as this type was utilized in the presented work. Further, the experimental setup and the procedure used at JINR Dubna will be described. Finally, the quantitative estimates of the Rb release are presented and discussed.

4.1 RGA in UHV by linear quadrupole mass spectrometer

Complete characterization of a vacuum environment requires the detection of all the component gases present, as well as measurement of the total pressure. RGA is a mass spectrometer of small physical dimensions that can be connected directly to a vacuum system and whose function is to analyze the gases inside the vacuum chamber. The principle of operation is the same for all RGA instruments: a small fraction of the gas molecules are ionized (positive ions), and the resulting ions are separated, detected and measured according to their mass-to-charge ratio, m/z. Here from definition m is the dimensionless mass number of a given ion and $z = q/e$ is the number of its elementary charges. RGAs are widely used to quickly identify the different molecules present in a residual gas environment and, when properly calibrated, can be used to determine the concentrations or absolute partial pressures of the components of a gas mixture.

4.1.1 Linear quadrupole mass spectrometer

Here the main features of the LQMS parts are described, the emphasis will be put on the variants and configurations used in the experimental issue of this work [29, 30, 31]:

Ion source – the practical design of an **i**on **s**ource (IS) utilizing the **e**lectron **i**onization (EI) (Fig. 5) is arranged so that an ion generated within an electric field as realized between two oppositely charged plates, will be accelerated towards the plate of opposite charge sign. If the attracting plate has a hole or a slit, a beam of approximately monoenergetic ions is produced. The beam of neutral gaseous molecules of the sample enters the ionization chamber (ion volume) in a line vertical to the paper plane and crosses the electron beam in the center. The beam of ionizing electrons is produced by thermionic emission from a resistively heated metal filament (heated to incandescence) typically made of rhenium (Re), tantalum (Ta), tungsten (W), thoriated iridium (ThO_2/Ir) or yttriated iridium (Y/Ir), the filament temperature usually reaches up to about 2 000°C during operation. In modern instruments the heating current for the filament is emission-controlled, *i.e.* the current of the electron trap (Fig. 5) is used to keep electron emission comparatively independent from actual IS conditions. Typical electron emission currents I_e are in the μA–mA range. Any concrete application of a LQMS requires a specific design of the IS—suitable filament and

[1] The abbreviation RGA will be somehow arbitrarily used for referring to both **r**esidual **g**as **a**nalysis and **a**nalyzer in this work, according to common usage nowadays. The term LQMS usually refers to the mass spectrometer type itself while the term RGA is meant as the LQMS utilized in practice.

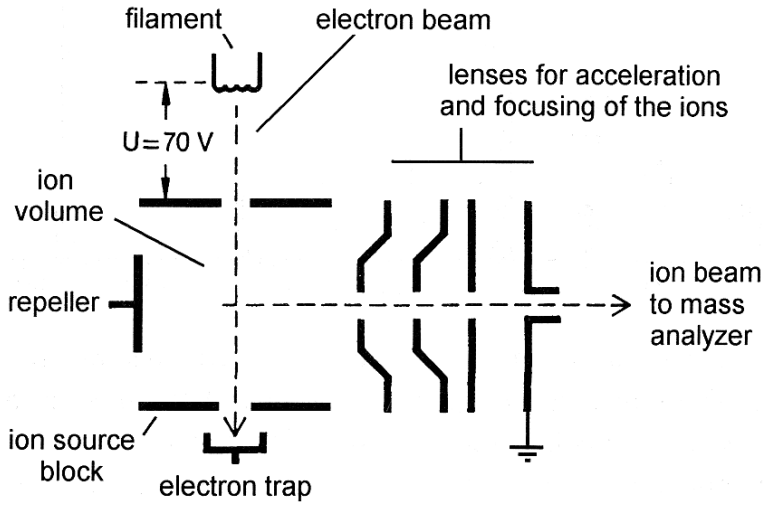

Fig. 5. Schematic layout of a typical EI ion source [29].

electrode material, configuration, ion beam optics and potential characteristic. Common EI types (designs) of IS nowadays are the axial IS, crossbeam IS and grid IS [31, 32].

When generated, ions are usually assumed to have the nominal energy set by the applied accelerating voltage in the IS and their velocity is assumed to be entirely in the direction towards the mass analyzer. In addition, together with this accelerating voltage there can be some low voltage applied to the repeller electrode, pushing out the ions immediately after generation and reducing so the loss of ions by neutralizing collisions with the walls. After being accelerated, the ions are focused towards the mass analyzer. Efficient ionization and ion extraction are of key importance for the construction of IS producing focusable ion currents I in the nA range.

Quadrupole mass analyzer – the actual **q**uadrupole **m**ass **a**nalyzer (QMA) of a LQMS consists of four hyperbolically or cylindrically shaped (in practice a circular approximation of the ideal hyperbolic rods cross section is often used) rod electrodes extending in the z-direction and mounted in a square configuration (xy-plane, Fig. 6). The ions are being separated due to the (in)stability of their path in a linear RF quadrupole field which is obtained by applying a voltage with fixed DC component and alternating AC (RF) component to the set of rods. The pairs of opposite rods are each held at the same potential, one pair of opposite rods at a potential $\Phi_0 = U + V\cos\omega t$ and the second pair on the opposite potential.

Ion detector – the ions which have been separated according to their m/z ratio in the rod system, can be electrically detected by various types of detectors, among which the commonest are [29, 31, 33]:

- **F**araday **c**up collector (FC) measuring the ion currents directly,
- **e**lectron **m**ultiplier (EM) which measures an electron current proportional to the ion current and can be discrete or continuous:
  - discrete dynode **s**econdary **e**lectron **m**ultiplier (SEM),

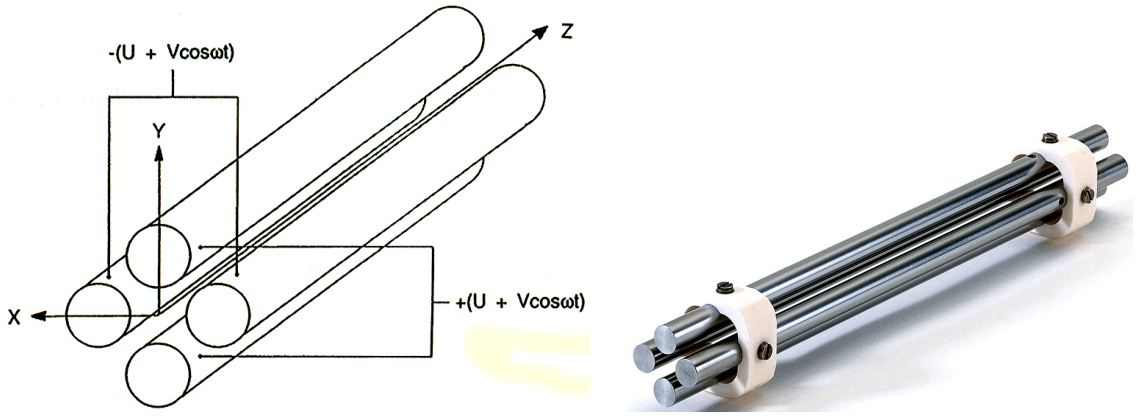

(a) **(b)**

Fig. 6. Rod system of a LQMS on **(a)** schematic [29] and **(b)** photograph [34].

> **c**ontinuous **d**ynode **s**econdary **e**lectron **m**ultiplier (CDEM or C-SEM), also called **c**hannel **e**lectron **m**ultiplier (CEM) or just channeltron.

The choice of detector is primarily based on the required detection sensitivity and the detection speed. It is also determined by other application-specific requirements, such as the required stability, the thermal and chemical stability and the amount of space available.

In the simplest case, but also with the least systematic errors, the ions hit a FC (a simple metal plate or cup-shaped electrode) where they deposit their charge by electron transfer from the metal to the ion. The FC measures the incident ion current directly, *i.e.* the electrons given up in this process establish an electric current that has the same intensity as the incoming ion current. The electric current flowing away from the FC electrode results in a voltage when passing through a resistor of high impedance. The detection limit lies between 10^{-16}–10^{-14} A, depending on the time constant (from couple of s to 100 ms). The FC signal is not affected by degradation or mass-discrimination effects at the detector, *i.e.* all ions are detected with the same efficiency regardless of their mass, however, the sensitivity of a FC is naturally limited by the noise of the amplifier. In addition to the simple and robust design, a FC also has long-term stability and high thermal resistance. The FC is therefore integrated into most of spectrometers as a basic option of detection, often in combination with SEM or CEM.

A SEM is basically a set of discrete dynode stages (usually cup-shaped) held at more positive potential (about 100 V) each. When an energetic particle impinges on the surface of the first dynode (conversion dynode), secondary electrons are emitted from that surface. Due to the more positive potential of the following dynode, all emitted electrons are accelerated towards and hit that surface where they in turn cause the release of several electrons each. In this way an avalanche of electrons is produced which causes an electric current large enough to be detected by a sensitive preamplifier. Because of a certain air sensitivity of the emissive layer and in order to prevent arcing due to **h**igh **v**oltage (HV) applied, EMs generally require operation in high vacuum. The ion currents actually reaching the first dynode are chiefly in the pA range, but may span over 10^{-18}–10^{-9} A. Depending on the applied voltage, SEM provides a gain (signal amplification defined relatively to the

FC signal) G of 10^6–10^8. The resulting current at the SEM electron trap is the input of a nearby preamplifier providing another 10^6–10^9 gain [29]. Preamplifier output current is processed further by an analog-to-digital converter.

The cascade of secondary electrons can be also produced in a continuous tube. In such detectors—CEMs (Fig. 7)—the voltage drops continuously from the ion entrance to the

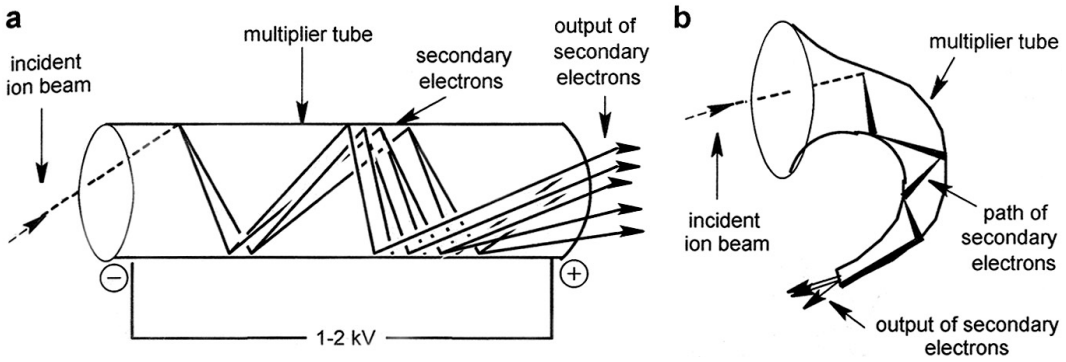

Fig. 7. Schematic of **(a)** linear and **(b)** curved CEM [29].

electron exit of the tube requiring a sufficiently high resistance of the semiconducting material to withstand high voltage of about 2 kV. This is accomplished by an emissive layer (high secondary electron emission yield) of silicon dioxide overlying a conductive layer of lead oxide on the supporting heavily lead-doped glass tube. Straight CEMs are unstable at gains exceeding 10^4 because positive ions created inside by EI of residual gas are accelerated towards the input side of the tube where they randomly contribute to the signal causing spurious output pulses. A curved design (a funnel-shaped input aperture) shortens the free path for ion acceleration thereby suppressing noise from this ion-feedback. Curved CEMs provide gains up to 10^8 [29]. Nevertheless, this amplification ratio is essentially limited by the dark current in the active layer of the CEM, as *e.g.* an utilizable value of the gain approx. 10^6 (at the bias voltage of 2.5 kV) is reported [31].

However, the use of whether SEM or CEM has some disadvantages, bringing uncertainties and sources of error in quantitative analysis. The number of electrons ejected per ion impacting the conversion dynode is dependent on both the mass and the type of an ion, as well as on the energy of the ion. Furthermore, the state of the surfaces and thus the yield of secondary electrons changes during operation. If more accurate quantitative measurements are to be carried out, the amplification must be checked at regular intervals and the unit must be recalibrated if necessary. Comparative measurements with the FC as the detector are suitable for this purpose [33, 35].

The most important operating characteristics of any LQMS are its maximum mass range, ultimate resolution and throughput characteristics. When performing a mass scan (with a given scanning speed) the maximum mass range (maximum mass) determines the maximum m/z value for which the LQMS can be tuned, the ultimate resolution (or resolving power) expresses the ability of the LQMS to resolve ions having different m/z values and the throughput describes the ion transmission through the QMA. With respect to the use of the LQMS as a RGA another very important characteristic, a sensitivity to a particular gas species, must be considered. It

is a well known fact that the sensitivity of any LQMS, likewise to the case of any ionization vacuum gauge, is gas-specific.

The **max**imum mass range $M_{\max}$ of the LQMS is the range of masses defined by the lightest and the heaviest singly charged ions which can be detected by the LQMS. From the fundamental theory [29, 30] it follows

$$M_{\max} = \frac{7\times10^6\, V}{f^2\, r_0^2}\,, \tag{8}$$

where V and f are the amplitude and frequency of the alternating RF component of the voltage applied to the QMA rods, respectively, and r_0 stands for the distance from the center of the quadrupole field to an electrode, *i.e.* the inscribed field radius.

The terms resolution and resolving power both expressing the ability of a QMA to resolve ions having different m/z values should not be confused, the **r**esolving power R is defined as dimensionless ratio

$$R = \frac{m/z}{\Delta(m/z)_{10\%}} \tag{9}$$

between a particular m/z and the resolution $\Delta(m/z)_{10\,\%}$. The width $\Delta(m/z)$ of the peak on this m/z value is measured at a specified height (at 10 % in normal practice) above the baseline. Again, from the fundamental theory it can be deduced that for a given m/z value the resolution $\Delta(m/z)$ can easily be adjusted by variation of the U/V (DC/RF voltages) ratio. It is well established that the resolution attainable by a LQMS cannot be arbitrarily increased but is ultimately limited by the mechanical accuracy of the rods construction as well as by the number of cycles N of RF field to which the ions are exposed before they reach the detector. For this number a simple relation stands [33, 36]

$$N = \frac{f\, L}{v_z}\,, \tag{10}$$

where f again represents the frequency of the RF voltage, L is the length of the QMA rods and v_z is the initial velocity of the ion in the z-direction (towards the ion detector, cf. Fig. 6). From Eq. 10 it follows [30] that the ultimate (**th**eoretical) resolution $\Delta(m/z)_{\mathrm{th}}$ of the LQMS is

$$\Delta(m/z)_{\mathrm{th}} = \frac{4\times10^9\, E_z}{f^2\, L^2}\,, \tag{11}$$

where the ion injection energy $E_z = m\, v_z^2/2 = q\, V_a$, V_a being the accelerating voltage, is assumed to be entirely in the z-direction. It is a common practice in modern LQMS devices to keep $\Delta(m/z)_{10\%}$ constant over the entire m/z range at a value which insures adequate separation of masses that are 1 u apart [2] (unit resolution) [32, 33].

An increase of U/V ratio (higher resolving power R) causes the increase of amplitude of the ion oscillations within the QMA and thus a greater fraction of the ions is lost due to collisions with the QMA rods (lower throughput). Moreover, since the resolution is kept constant during the scan, the resolving power R increases with mass (Eq. 9) reducing the effective QMA

[2] Since 1961 the **u**nified atomic mass [u] is defined as $^1/_{12}$ of the mass of one atom of nuclide ^{12}C which has been assigned to 12 u exactly by convention, thus $1\,\mathrm{u} = 1.660\,55\times10^{-27}$ kg. Prior to 1961 physicists defined the **a**tomic **m**ass **u**nit [amu] based on $^1/_{16}$ of the mass of one atom of nuclide ^{16}O. The definition of chemists was based on the relative atomic mass of oxygen which is somewhat higher resulting from the nuclides ^{17}O and ^{18}O contained in natural oxygen.

throughput for high m/z values and thus causing a mass discrimination[3]. This effect must be taken into account when drawing quantitative conclusions from the ion currents. These two features—1. resolving power versus throughput interdependency and 2. mass discrimination—of a LQMS clearly show the need to find a necessary compromise ('trade-off') for any given application between possible resolution and high throughput, and thus sensitivity.

The exact relationship between resolution and sensitivity is very complex as it depends on the concentration and divergence of the ion beam leaving the IS. It is complicated further by the defocusing action of the fringing fields between the IS and the rods. However, as a general rule of thumb, sensitivity decreases at 1–1.5 times the rate of resolving power increase [33]. Generally, the sensitivity S_g $\left[\mathrm{A\,mbar^{-1}}\right]$ of the RGA to a particular gas species g (sensitivity to partial pressure P_g of gas g) is defined [37] as

$$S_g(P, P_0) = \frac{H_g\left(m/z_{\mathrm{bp}}\right) - H_{0g}\left(m/z_{\mathrm{bp}}\right)}{P - P_0}\,, \tag{12}$$

where $H_g(m/z_{\mathrm{bp}}) - H_{0g}(m/z_{\mathrm{bp}})$ represents the change in principal mass peak—**b**ase **p**eak, *i.e.* the most intense peak of gas g mass spectrum—height [A] in the mass spectrum and $P - P_0$ the corresponding change in total pressure [mbar] due to the change in P_g. $H_{0g}\left(m/z_{\mathrm{bp}}\right)$ and P_0 are the background values. Thus the definition expresses the RGA response in the ion signal [A] to a certain change of P_g [mbar]. From now on the sensitivity S_g will be designated as $S_g = S_g(P_g, P_0)$ as obviously $P - P_0 = P_g$, and also the term RGA instead of LQMS will be used.

The overall RGA sensitivity is a final product of a number of processes occurring in all the RGA parts (IS: EI and focusing, QMA: ion transmission, EM: conversion of the ion beam to the signal output), each showing its own dependencies. Moreover, the EM gain G is usually separated from the intrinsic sensitivity $S_g(P_g, P_0)$ which is originally defined for the FC mode detection [33, 35], *i.e.* the sensitivity factors of the RGA are determined for the FC mode detection (FC mode reading H_g^{FC} of P_g) as $S_g^{FC}(P_g, P_0)$ and the RGA operated in the EM mode shows a different sensitivity $S_g^{EM}(P_g, P_0, \mathrm{HV})$ which can be calculated as

$$S_g^{EM}\left(P_g, P_0, \mathrm{HV}\right) = G_g(\mathrm{HV})\, S_g^{FC}\left(P_g, P_0\right)\,, \tag{13}$$

where the EM gain $G_g = G_g(\mathrm{HV})$. Thus the EM mode sensitivity $S_g^{EM}(P_g, P_0, \mathrm{HV})$ varies strongly with the EM HV applied and depends on the gas g.

In addition, the sensitivity is a strong function of the specific instrument design (IS design and ion beam extraction and focusing geometry, quality of the QMA rods and the FC and/or EM design) and settings (electron emission, electron energy, ion energy, resolution) as well as of operating conditions (surrounding vacuum conditions, previous exposure to active and/or non-active gases, presence of one gas when quantifying another gas, contamination *etc.*). Hence, the sensitivity of a particular RGA instrument to a particular gas species is usually obtained from the calibration data as such an overall sensitivity by given operating conditions and instrument settings. Obviously, the sensitivity factors must be obtained under the same operating conditions that will be used during the common analysis.

Finally, the basic parameters which most especially influence the three important operating characteristics of any RGA—1. the (maximum) mass range M_{max}, 2. the (ultimate) resolution $\Delta(m/z)_{\mathrm{th}}$ and 3. the sensitivity S—are summarized:

[3]Generally, the mass discrimination is defined as the variation of the combination of the efficiencies of the extraction, transmission and detection of ions as a function of the m/z ratio [38].

- L and r_{rod}, the rods length and radius, respectively (usually $r_{\mathrm{rod}} = 1.144\, r_0$ is chosen for well approximating the ideal quadrupole field),
- V, the RF voltage amplitude,
- f, the RF supply frequency,
- U/V, the ratio between the DC voltage magnitude and the RF voltage amplitude,
- I_e, the IS emission current,
- E_e, the electron energy,
- E_z, the ion injection energy ,
- EM HV, high voltage applied in the electron multiplier,
- v_{sc}, the mass **sc**an speed ,

the interdependencies of which join in a complicated way depicted in Fig. 8.

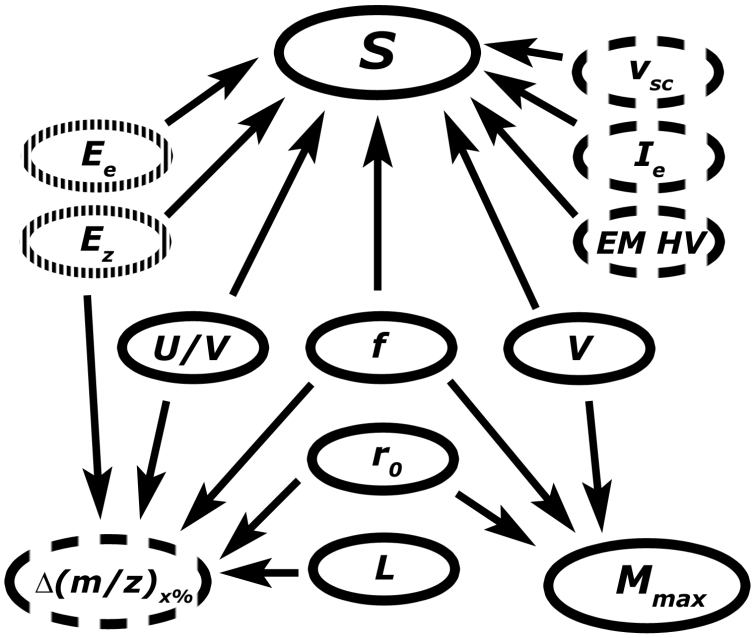

Fig. 8. Schematic of the RGA operating characteristics and parameters interdependencies sketched on the basis of relations gleaned from [30, 36, 37, 39, 40]. The notions in dashed and dotted lines represent the parameters of operation of the RGA Prisma™ QMS 200 M3, used in this work, which can be varied directly and implicitly (via another parameters) [31, 32], respectively.

4.1.2 RGA tuning and interaction with UHV system

In a usual UHV (10^{-7}–10^{-11} mbar) system the following processes and notions are encountered (see Fig. 9) [13]:

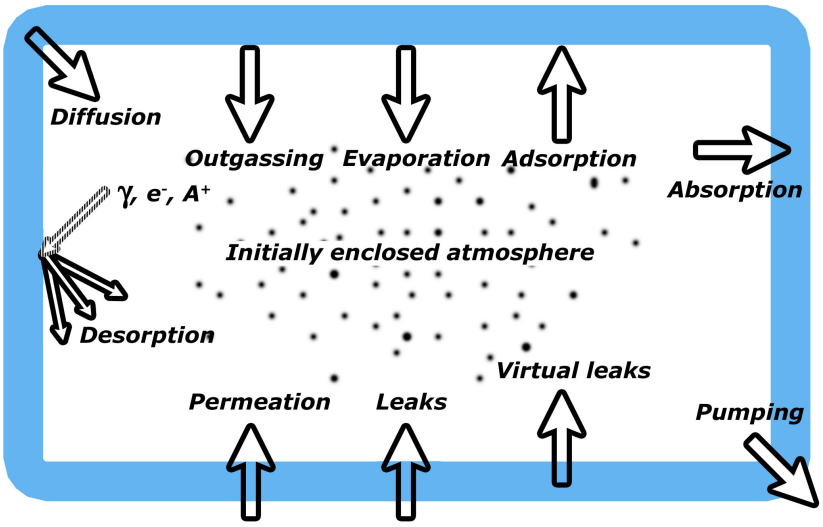

Fig. 9. Common sources of the residual atmosphere in any vacuum system. Based on [13].

- Initially enclosed atmosphere – the composition of the gas enclosed in the chamber changes significantly during the pumping from atmosphere through high vacuum range to the UHV, the most abundant air mixture gases like nitrogen, oxygen, carbon dioxide *etc.* are easily pumped away. The water vapor then makes the biggest part (up to 90%–95%) of the gas in the high vacuum range, however, the further pumping together with an application of heat (bakeout) decreases the desorption rate of water (see below) so hydrogen coming from the bulk of materials of the system is the major gas component. Anyway, whenever the system is opened to air all the internal surfaces are exposed to the water vapor found in the air as humidity and sorption will occur, covering the surfaces with layers being possibly even several hundred monolayers thick.

- Pumping – besides the obvious action of removing the molecules from the gas phase (initially from the atmosphere) or capturing/transfering the molecules randomly coming to the pumping unit (high vacuum and UHV range) the pump also influences the residual atmosphere in the chamber according to its working principle.

- Adsorption – any surface of a solid or liquid (chamber internal surfaces) exhibits forces of attraction normal to the surface, hence gas molecules impinging on the surface are attracted and assume an equilibrium position at minimum potential energy (heat of adsorption, H_a). If the adsorption is purely physical ('physisorption'), it involves relatively weak intermolecular Van der Waals forces. In chemisorption the process is similar to the formation of a chemical compound with transfer of electrons, in this case the attractive forces (and thus the heats of chemisorption, H_c, as well) being much larger than in the physisorption.

- Absorption – similarly to gas dissolving in a liquid, absorption means that the gas enters the bulk of a solid material and is 'taken up' by the volume. It is explained by an adsorption, followed by the penetration of the adsorbed gas into the solid by diffusion.

- Diffusion – the process of the gas molecules transfer into and through a solid due to the concentration gradient. It occurs also in a low vacuum range when two gases intermingle easily because of random motion of their molecules.

- Evaporation – vapor refers to a real gas in a state below its critical temperature (distinction between gas and liquid is possible). When a substance is present, some of the molecules near its surface have sufficient kinetic energy to escape into the atmosphere (evaporate) and exist as a gas. This means that the gas load will emanate from evaporation of the material itself. For each substance in an enclosed space, there is a point when the pressure of its vapor reaches a maximum (saturation) and a dynamic equilibrium between the number of molecules evaporating and the number of molecules being recaptured on the surface (condensation) is established. All the vapors (saturated and unsaturated) in a vacuum system are maintaining their physical state according to the pressure-volume-temperature (P-V-T) conditions existing in the system. There are some elements or compounds able to change (sublimate) from the solid to the vapor without passing through the liquid phase.

- Desorption – when a material is placed in a vacuum the gas which was previously ad- or absorbed (generally sorbed) begins to desorb, *i.e.* to leave the material. This process is influenced by the pressure, the temperature, the shape of the material, and the kind of its surface. The pressure has a basic influence since according to its tendency of increasing over or decreasing below the equilibrium, the phenomenon of sorption or that of desorption appears. Nevertheless the function between the desorption rate and the pressure is not clear at pressures much lower than the equilibrium because of its interdependency with the pumping time. Desorption is endothermic thus the temperature has a clear influence of accelerating the desorption by increasing the temperature. Furthermore, electron, photon or ion bombardment increases substantially the desorption rate as well—**t**emperature/**e**lectron/**p**hoton/**i**on **s**timulated (induced) **d**esorption (TSD, ESD, PSD, ISD) is encountered.

- Outgassing – the release of gas resulting from the spontaneous desorption (*i.e.* no stimulation by an impact of molecules, electrons, ions, and photons or by thermal energy is considered) is known as outgassing. The complete theory of such a process includes both the adsorption and the absorption simultaneously, however, in most cases the rate of diffusion is so small compared with that of desorption of adsorbed gas that the two processes may be analyzed separately and the resulting outgassing rates subsequently added.

- Leaks – an ideal vacuum chamber should maintain forever the vacuum (pressure) reached at the moment of its separation from the pumps. Any real chamber presents a pressure rise after being isolated from the pumping system, the rise being produced by the gas which penetrates through leaks, that which evolves from the walls (outgassing) and that entering by permeation (see below). A perfectly tight vacuum system would have a zero real leak late, but to achieve this is as impossible as to reach zero pressure. The leakage can be avoided as much as possible by careful consideration of seals, welding techniques and general careful handling of demountable seals.

- Virtual leaks – they are not really leaks, however, they act that way. A virtual leak is a source of gas that is physically trapped within the chamber with only a small (very low conductance) path from the trapped 'pocket' (*e.g.* a weld crack, a gap between flanges or

two surfaces) of gas into the chamber. Due to a different nature when compared to the real leaks (constant gas inflow) they can be observed as small bursts of pressure on a fixed time base.

- Permeation – generally all the gases have the possibility of passing trough solids, even if the openings present are not large enough to permit a regular flow. The permeation is the passage of a gas into, through and out of a solid barrier (chamber envelope) having no holes large enough to permit more than small a fraction of the gas to pass through any one hole. The process firstly involves the adsorption of the gas on the surface where the gas pressure is higher. After being dissolved in the outside surface layer the gas slices down the concentration gradient and diffuses to the vacuum side where it is desorbed. In the UHV range the hydrogen permeation is of a high importance as this is the main process responsible for the dominant residual UHV atmosphere component. The reason for such a high permeability is the dissociation of the hydrogen to atoms and their passage through the wall, after which the recombination and desorption occurs. All the materials are permeable to some extent.

The well known practical considerations (gas loads, conductance, pumpdown *etc.*) of vacuum systems which can be found in [13] and elsewhere will be used in practice within Sect. 4.2.1. Similarly to **h**ot **c**athode **g**auges (HCGs) the influence of a RGA on the residual atmosphere composition of a vacuum system is related to a complex set of physical processes on surfaces and is extensively studied and described in vacuum literature. The notions and processes usually encountered with the use of a LQMS as a RGA in UHV system will be reviewed now, arranged according to the way which an ion experiences in the RGA ('IS → QMA → EM').

Grid ion source – for the purposes of a usual UHV RGA the **o**pen **i**on **s**ource (OIS) has become a widespread type of the IS, the open configuration of which provides unrestricted communication between the vacuum environment and the ionizing region. There is a number of variants of OIS design (*e.g.* axial, cross-beam OIS *etc.*), however, here only the grid IS will be considered as the RGA Prisma™ OIS "electrodes configuration and potential characteristic are similar to those of the grid IS" (in detail in Sect. 4.2.2) [31]. In a common grid OIS two circular filaments surrounding the anode grid structure are resistively heated to incandescence and emit electrons to ionize the neutral gas molecules. The grid IS is preferred for very low desorption rates and the ease of cleaning—degassing by electron bombardment. The IS has a complex influence on the RGA performance and on the gas composition of the overall vacuum system itself as well:

- Filament material evaporation – at the common filament temperature of about 2 000°C the tungsten saturated vapor pressure is of the order of 10^{-9} mbar which implies that when measuring very low pressures this evaporation influences the measurement itself. However, this is a problem for hot-filament *total* pressure gauges (HCGs) while for the *partial* pressure gauges—RGAs—it simply means that the W^{+} (and often W^{+2}, W^{+3} and even up to W^{+6} [41]) peaks can be found in the mass spectrum.
- Thermal radiation – in the (ultra)high vacuum most of the energy required to heat the filament in order to establish an electron emission current is dissipated to the surroundings through radiative processes. As a result, the entire IS and the adjacent walls 'run hot' [33]. The elevated temperatures result in increased outgassing from the IS itself and from the adjacent chamber walls.

- TSD – the hot filament emits significant quantities of gas previously ad-/absorbed. This effect is usually seen as a quite rapid rise in the pressure when the RGA is turned on after which the pressure fall even when the heating current is further increased [42]. Such a behavior corresponds to the fact that the desorption rate of any species from a given surface (*e.g.* W) shows a sudden maximum at a certain temperature [43]. In addition, a thermal decomposition of the ad-/absorbed species can occur, thus the RGA operation can actually change the (residual) atmosphere composition. Degassing the IS can help minimize the TSD, however, this usually only works as a temporary solution as the ad/absorption of the molecules from the gas phase then continues [31, 33].
- PSD – the photons coming from other devices and processes in a vacuum system can stimulate the desorption of the ad-/absorbed species as well [44].
- ESD – even after an RGA has been thoroughly baked out, peaks are frequently observed at $m/z\,1\,(H^+)$, $2\,(H_2^+)$, $12\,(C^+)$, $16\,(O^+)$, $19\,(F^+)$, $23\,(Na^+)$, $35\,(^{35}Cl^+)$, $37\,(^{37}Cl^+)$ and $39\,(K^+)$ [33, 40, 44, 45, 46] which are formed by ESD from surfaces within the IS rather than by EI of gaseous species. The distinct origin of the gas-phase and ESD ions results in different energies of the ions—due to a higher initial energy of the ESD ions they can pass the QMA at much lower injection energies than the gas ions—thanks to which they can be distinguished by lowering the appropriate potential in the OIS/QMA [47].
- ISD – due to bombardment with ionized gas molecules the ISD from the extraction plate in the IS occurs, being closely related to physical sputtering and chemical reactions on the plate surface [48].
- Chemical reactions – the RGAs are known to pump and release gases so the phenomena that arise in some particular experimental conditions must be discriminated, otherwise the results can contain a considerable error. Various reactions occur on the hot filaments and surfaces in the IS, actually acting as 'chemical factories' pumping (the gas is a reactant) or producing (final product) the gases in a vacuum system and thus changing significantly the vacuum atmosphere. The reactions with water, oxygen, hydrocarbons *etc.* generating considerable amounts of carbon monoxide, carbon dioxide and methane *etc.* have been often observed [37, 49, 50, 51]. Such reactions also lead to the embrittlement of the filament.
- Potential characteristics – the potentials experienced by an ion created in the IS certainly affects the overall RGA sensitivity in a complex way depending on the IS design.
- Electron emission current I_e – the I_e current from the filament to the grid is regulated by a feedback control loop which dynamically adjusts the operating temperature of the filament(s) to keep the total I_e current constant. Ideally, the rate of formation of ions should be proportional to the I_e, however, in practice the exact dependence between the ion signal and the I_e current in small ISs is complicated by space-charge effects and only general trends can be predicted. Greater ionization efficiency is to be expected as the I_e current increases. I_e is influencing the sensitivity linearity in a complex way according to the IS type [53, 54].
- Ion energy E_z – in any real RGA there is a strong correlation between the sensitivity and ion energy. This correlation appears to be due to two factors [54, 55]: first, as

the ion energy is increased the angular distribution of ions leaving the IS is narrowed, resulting in a better 'match' with the acceptance of the QMA. Second, as the ion energy increases the ions spend less time in the fringing fields between the IS and the QMA, with a consequent reduction in ion loss associated with this region.

Resolution and/versus sensitivity – the compromise between these two LQMS principal parameters has to be always found for any given application, however, as there is often only a small amount of gas available in the vacuum system the most important property of the RGA is the high sensitivity. As a consequence, the mass resolution is usually low, just allowing to resolve two adjacent peaks.

- Resolution ↔ sensitivity – this interdependence is well illustrated in Fig. 10.

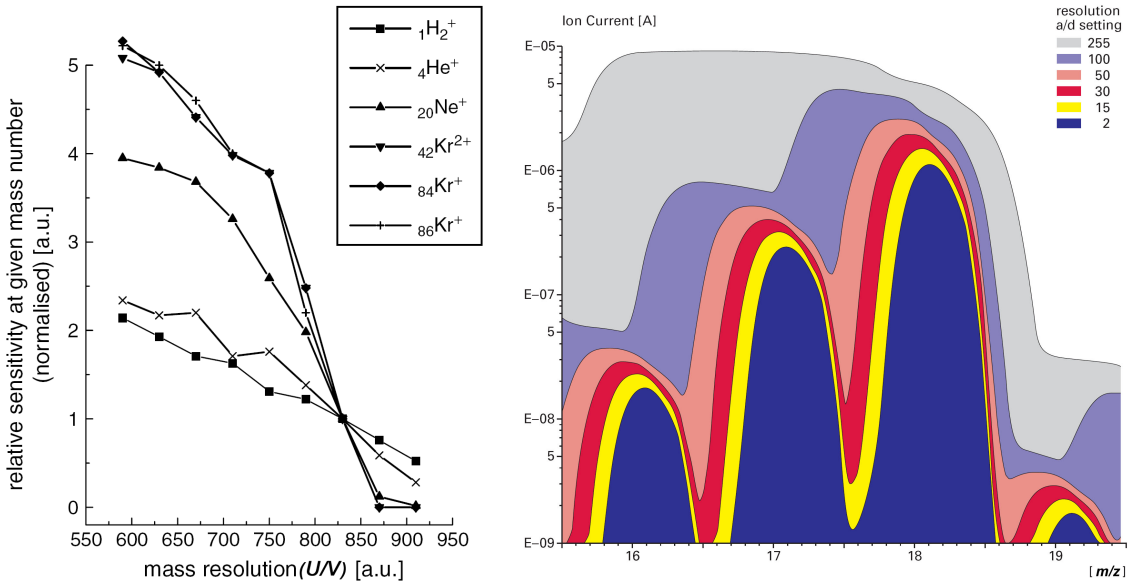

Fig. 10. Variation of the sensitivity with resolution. **(a)** The dependence of the relative sensitivity on the mass resolution—determined by the U/V ratio—is shown for five different m/z numbers, the mass discrimination is obvious (the sensitivity is normalized at the mass resolution setting typically utilized in measurements) [40]. **(b)** RGA Prisma™ scan of the H_2O group peaks with different resolution values illustrates the variation of the detected ion currents [31].

- Sensitivity linearity and stability – a nearly linear relation between the RGA ion current reading $H_g(m/z_{\rm bp})$ and the partial pressure P_g is highly desirable as the linear response simplifies the RGA calibration since the sensitivity S_g need not be determined over the entire pressure range. Even the analysis of relative PPs will be simplified then if corrections do not have to be made for the pressure dependence of relative sensitivities. The linearity is influenced by the operating parameters like the I_e current, E_e and E_z energies, however, each IS design will show its own unique way of such dependencies. Usually some combination of the IS settings can be found to obtain a satisfactory linearity at low pressures 10^{-6}–10^{-9} mbar [54]. Deviations from linearity are to be expected above the pressure 10^{-5} mbar due to space charge effects

in the IS and ion-neutral scattering interactions in the QMA [33]. The stability of an instrument determines how often calibration is required to assure a desired level of accuracy that can be expected as a function of time since the calibration. EMs are the main source of the overall instability of the RGA, anyway, any exposure to active gases (CO_2, CO, CH_4, O_2 *etc.*) can produce a serious instability—due to various reactions—even for the FC mode [54].

- Cross-sensitivity effects ('matrix gas $\leftrightarrow$ trace gas') – the RGA response to a gas can possibly become rather unpredictable when instead of pure gases the mixtures of gases are considered. As stated in text below Eq. 12 $S_g = S_g(P_g, P_0)$ which represents the fact that the sensitivity for gas g can be influenced even by the level and the composition of the background pressure P_0. This is usually observed mainly for exposures to active gases [56, 57] thus for accurate considerations of the RGA readings the composition of the atmosphere being studied has to be taken in to account as well.
- **M**inimum **d**etectable **p**artial **p**ressure change (MDPP change, $\Delta P_{\min}$) – defined as the PP change corresponding to the smallest signal change which can be distinguished from noise [37]. As a general prescription $\Delta P_{\min} \approx \sigma/S_g$, where σ is the noise associated with the reference level with respect to which the change is measured and S_g is the RGA sensitivity for the gas of interest. The value of $\Delta P_{\min}$ is characteristic of the instrument alone, being influenced by the I_e current, E_e and E_z energies, peak width and EM gain as well as the pressure inside the IS and the particular ion species from which the signal is derived.

Mass scan: peak shapes and positions – when performing a mass scan the correct mass scale and non-deteriorated peaks (no peak splitting) are desirable for further analysis:

- Mass scale – the first step in the spectral analysis process is to correctly identify the m/z ratio of all the peaks in the mass spectrum. A well calibrated mass scale is essential to this task. Virtually every vacuum system have detectable amounts of H_2 ($m/z_{\text{bp}} = 2$), H_2O ($m/z_{\text{bp}} = 18$), CO ($m/z_{\text{bp}} = 28$) and CO_2 ($m/z_{\text{bp}} = 44$) so the base peaks of these species can be used to verify the correct performance of the instrument, *i.e.* the mass scale and the mass resolution [31, 32, 33].
- Peak shapes – the shape of a peak in a mass spectrum is virtually determined by the actual resolution and IS potentials settings of the RGA. The ideal peak shape is a 'flat top' shape so that the signal intensity for each m/z can be determined by averaging over the flat section of the top. With too low resolution the tails of the peak end in the peaks on the neighboring m/z values which changes the intensity of this peak. Thus the unit resolution is advised for a usual RGA operation in order to have as low resolution as possible but still resolving the neighboring peaks [33].

EM gain dependence and (in)stability – the RGA S increases with the EM gain, higher sensitivities providing then lower MDPPs and faster spectral scans. However, the increase in sensitivity is obtained at the price of limited dynamic range, mass discrimination effects, gain instabilities and finite lifetime of the device.

- $G = G(\text{EM HV})$ – the EM gain in the RGA is a function of the bias voltage and is measured relative to the FC signal. Fig. 11**a** shows a typical $G = G(\text{EM HV})$ dependence [31, 33, 35].

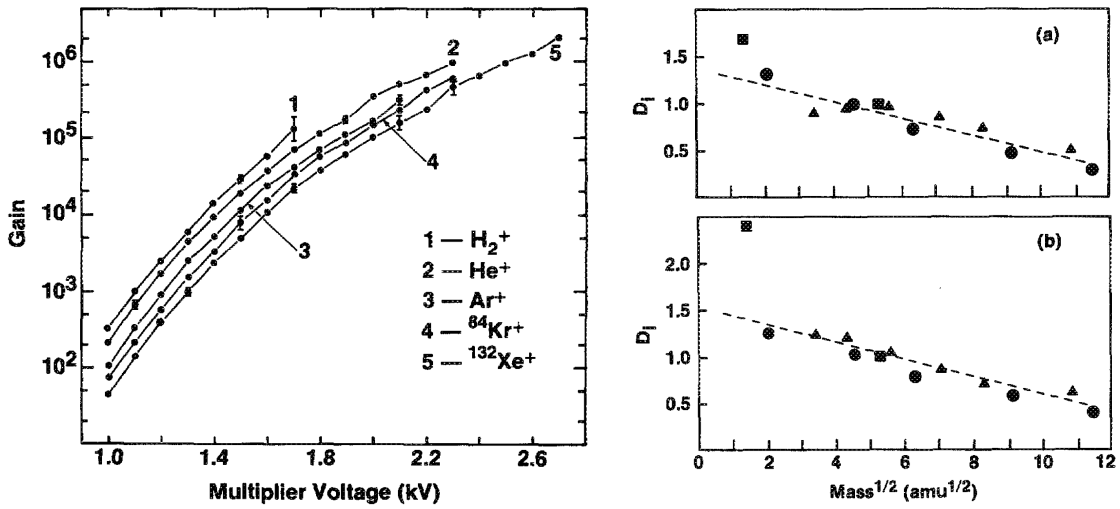

Fig. 11. CEM gain dependencies [35]. **(a)** CEM gain G_i as a function of HV [kV] for H_2^+, He^+, Ar^+, $^{84}Kr^+$ and $^{132}Xe^+$ over the range from 1.0 to 2.7 kV. The error bars shown are representative of all the ions studied, the relative spacings between the curves within the data set were the same for all four examined CEMs. **(b)** Detection factor D_i (reference gas N_2 at m/z 28) versus mass$^{1/2}$ at CEM HV of *a)* 1.3 kV and *b)* 1.7 kV. Symbols: • ions from inert gases (He, Ne, Ar, ^{84}Kr and ^{132}Xe), ■ ions from homonuclear diatomic gases (H_2 and N_2), and ▲ ions from C_2F_6. All data taken with the same CEM, for other CEMs the same trends in chemical nature dependence were observed.

- $G = G(m/z)$ – the total gain of the EM varies as a function of the mass of the incident ions, the gain decreases with increasing ion mass. This mass discrimination effect is caused by the dependence of ion-electron conversion efficiencies on the velocities of the ions entering the detector. An inverse relationship with the square root of the mass has been reported for monoatomic ions of the same energy [35], see Fig. 11**b**. For accurate quantitative measurements, it is essential to calibrate in advance the gain of the EM for the specific ionic species being detected.
- Gain stability – an important problem when working with an EM is that its gain changes with time. Gain degradation is unavoidable, and particularly serious just after the detector has been exposed to air, or after high quantities of reactive gases have been introduced into the vacuum system. Frequent calibration of the EM gain against the FC output is recommended for reliable quantitative measurements [40]. An example of such a long-term variation of the EM mode sensitivity S^{EM} for a given mass is displayed in Fig. 12**a** and of the ratio of sensitivities for two mass numbers in Fig. 12**b**.

4.1.3 Quantitative analysis

For careful quantitative analysis it is important that the sensitivity of the RGA be determined for every gas which may be a component of the system and under the same operating parameters used during the actual measurements. Each gas ionizes differently, and its ions travel through

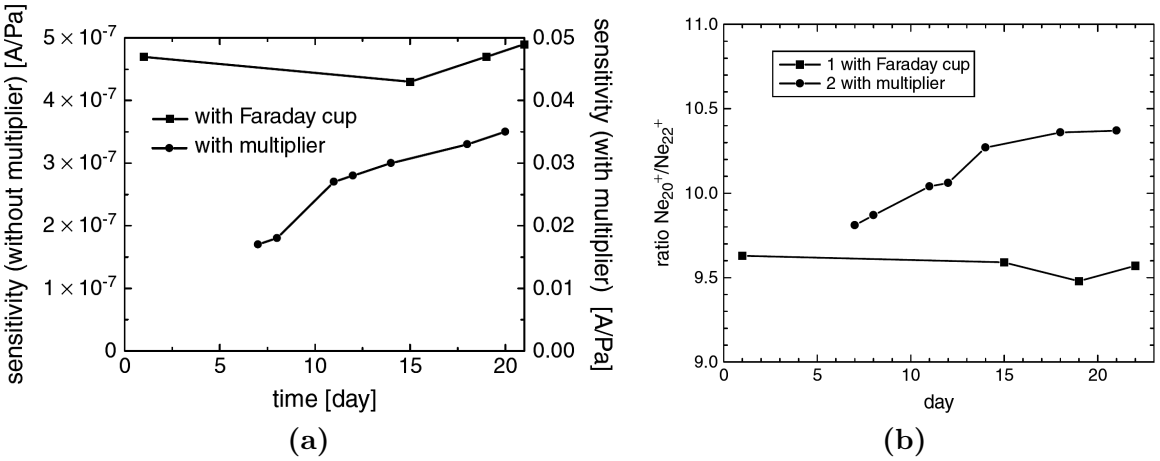

Fig. 12. Long-term stability of detectors [40]: **(a)** stability of the sensitivity of a mass spectrometer with a FC or an EM, **(b)** stability of the ratio of mass spectrometer sensitivities for different mass numbers, an example for Ne isotopes 20 and 22.

the QMA with different efficiencies. As a result the proportionality constant relating the ion current reading $H_g(m/z_{\mathrm{bp}})$ of a gas g to its P_g is very dependent on the specific gas.

Sensitivity factors change as a factor of time due to an aging of the RGA thus a periodic 'recalibration' is necessary. When only a few choices of calibration gases are available then the choice of those that are most likely to be encountered during measurements (*i.e.* usual major components of the residual gas environment of the chamber) is advised [31, 33].

There are several methods of calibrating the RGA [37], namely:

- Direct pressure comparison – this method is based on a direct comparison of the RGA ion signal with a pressure reading on a calibrated transfer standard gauge both connected to a special calibration chamber. Firstly the background scan (RGA) and total pressure reading (gauge) is performed after which a calibration gas is introduced and the scan and pressure reading are repeated. The relation similar to Eq. 12 is then used (now P_0 and P being the total pressure readings prior to and after the gas introduction, respectively).

- Pressure divider method – utilizes an indirect comparison of the RGA output with readings of a transfer standard gauge separated by a flow restriction.

- Orifice flow method – compares the RGA reading with with the calculated pressure generated in an orifice-flow system.

- *In situ* calibration of the RGA in a process application – examines the RGA response to known gas flow rates. This method requires that the pumping speed during the calibration be the same as during the RGA use.

The entire mathematical formalism used to derive the partial pressures of a mixture scanned in a single mass spectrum is based on the assumption that the total spectrum is a linear combination of the spectra of the different species that are present in the mixture, In other words, the total spectrum is equal to the sum of the individual peaks that would be observed if each

constituent were alone in the system:

$$H^{FC,EM}(m/z\,X) = \sum_g H_g^{FC,EM}(m/z\,X)\,, \tag{14}$$

where $H^{FC,EM}(m/z\,X)$ denotes the FC or EM mode reading on a given $m/z\,X$ position and $H_g^{FC,EM}(m/z\,X)$ stands for the contribution of gas g to this peak height. $H_g^{FC,EM}(m/z\,X)$ is related to the fragmentation factor $\mathcal{F}$—which is the relative signal strength of detected ions produced from a given chemical species under specified conditions of pressure, gas composition and instrument operating parameters [37]—as

$$H_g^{FC,EM}(m/z\,X) = \left[\mathcal{F}_g(m/z\,X)\,G_g(\mathrm{HV})\,S_g^{FC}(P_g,P_0)\right]\,P_g\,. \tag{15}$$

Here $\mathcal{F}_g(m/z\,X)$ represents the fraction $\mathcal{F}_g(m/z\,X) = [H_g(m/z\,X)]\,/\,[H_g(m/z_{\mathrm{bp}})]$ from which it directly follows that for the base peak of any gas $\mathcal{F}_g(m/z_{\mathrm{bp}}) \equiv 1$ and the right-hand side of Eq. 15 then means

$$H_g^{FC,EM}(m/z_{\mathrm{bp}}) = S_g^{FC,EM}(P_g,P_0)\,P_g = G_g(\mathrm{HV})\,S_g^{FC}(P_g,P_0)\,P_g \tag{16}$$

which is just a combination of Eq. 12 and Eq. 13 where $G_g(\mathrm{HV}) \equiv 1$ for the FC mode. Eq. 14 and Eq. 15 can be combined into the system of equations

$$H^{FC,EM}(m/z\,X) = \sum_g \left[\mathcal{F}_g(m/z\,X)\,G_g(\mathrm{HV})\,S_g^{FC}(P_g,P_0)\right]\,P_g\,. \tag{17}$$

Since all gases have more than one peak in their fragmentation pattern, the number of peaks (represented by 'X') in a real spectrum is generally larger than the number of gases ('g'). As a result, this system of equations usually has more equations than unknowns. This situation is sometimes simplified eliminating some of the extra equations, however, the best results are obtained using all the equations and a multiple linear regression procedure to calculate the best possible fit to the data [33].

Errors can be introduced in the deconvolution of Eq. 17 due to a number of nonidealities associated with RGAs. For example, the fragmentation factors of CO, CO_2, CH_4 and N_2 have been shown to vary with pressure due to the ESD of ions from the IS surfaces, due to the formation of CO when CO_2 is exposed to the hot filaments and due to the different kinetic energies of the fragment ions [58, 59].

4.2 Experimental setup

The experimental setup being used at JINR Dubna consists of a small UHV chamber to which a commercial RGA is attached. The setup possesses one fixed position where the samples can be placed via an exchange system. The detailed description follows in this subsection.

4.2.1 UHV and fore vacuum system

The vacuum system shown in a scheme (Fig. 13) and photographs (Fig. 14) has been produced by Vakuum Praha and serves for the analysis of the residual atmosphere composition in UHV of 10^{-9} mbar (base pressure). The possible escape of the rubidium compounds from the non-radioactive samples (or ^{83}Rb compounds and/or $^{83\mathrm{m}}$Kr gas in the case of radioactive ^{83}Rb/$^{83\mathrm{m}}$Kr source) can be observed with the help of a commercial RGA. The system allows an exchange of samples with a deterioration of the vacuum to the level of 10^{-4}–10^{-3} mbar. The materials used in the system are reviewed in Tab. 3. It comprises the following parts [31, 32, 60, 61]:

- **S**tainless **s**teel (SS) UHV chamber of a cylinder shape (outer dimensions: height $l = 160\,\text{mm}$, diameter $\phi = 159\,\text{mm}$): total volume $V \simeq 3.6 \times 10^3\,\text{cm}^3$ and internal surfaces total area $A \simeq 1.6 \times 10^3\,\text{cm}^2$ (internal devices and additional space (flanges, pump *etc.*, see below) accounted for in both cases).

- Five DN40CF-F flanges (inner dimensions $\phi_{40} = 40\,\text{mm}$, $l_{40\text{sh}} = 28\,\text{mm}$ (4× '**sh**ort' type) and $l_{40\text{ln}} = 40\,\text{mm}$ (1× '**lo**n**g**')) and three DN63CF-F flanges (inner dimensions $\phi_{63} = 63\,\text{mm}$, $l_{63\text{sh}} = 38\,\text{mm}$ (1× '**sh**ort'), $l_{63\text{md}} = 58\,\text{mm}$ (1× '**me**d**i**um') and $l_{63\text{ln}} = 68\,\text{mm}$ (1× '**lo**n**g**')).

- Two gate valves allowing a 100 % open position: DN63CF-F between the UHV chamber and the pump, DN40CF-F between the UHV chamber and the fore vacuum system.

- **T**riode **s**putter-**i**on **p**ump (TSIP) IPT 25 connected via DN63CF-F (63 × 58) flange and DN63CF-F gate valve: pumping speed $S_\text{p}(\text{N}_2) = 25\,\text{l}\,\text{s}^{-1}$ and $S_\text{p}(\text{Ar}) = 10\,\text{l}\,\text{s}^{-1}$ (both values for $10^{-6}\,\text{mbar}$ and saturated condition), ultimate pressure $10^{-11}\,\text{mbar}$.

- UHV compatible Alkali Borosilicate (Kodial material) sight glass connected via DN63CF-F (63 × 38) flange.

- All the seals and flanges in the UHV chamber are UHV compatible and completely made from metal, except the DN63CF-F gate valve between the chamber and the TSIP which is made from metal and a special cured Viton material (the only non-metal part is the seal between the seat and the counter plate) allowing to operate down to 1×10^{-10}mbar,

- **O**xygen **f**ree **h**igh **c**onductivity copper (OFHC-Cu) sample holder connected via DN63CF-F (63 × 68) flange: clamping system for holding the sample carrier in a fixed position, samples of diameter up to 12 mm can be tested, possibility of cooling down (LN_2) or heating up (up to 250°C) the samples, volume $\simeq 90\,\text{cm}^3$.

- UHV **c**old **c**athode **g**auge (CCG) Pfeiffer Vacuum IKR 270 (inverted magnetron principle) connected via DN40CF-F (40 × 28) flange: 5×10^{-11}–$1 \times 10^{-2}\,\text{mbar}$, accuracy and reproducibility $\approx \pm 30\%$ and $\approx \pm 5\%$ in the range of 1×10^{-9}–$1 \times 10^{-3}\,\text{mbar}$, respectively, internal volume $\simeq 20\,\text{cm}^3$.

- RGA Pfeiffer Vacuum Prisma™ QMS 200 M3 (designated simply as 'Prisma™' hereafter) connected via DN40CF-F (40 × 42) flange: operation with FC: $P_\text{max}^{FC} = 1 \times 10^{-4}\,\text{mbar}$, $\text{MDPP}^{FC} < 2 \times 10^{-11}\,\text{mbar}$, sensitivity $S^{FC} \sim 10^{-4}\,\text{A}\,\text{mbar}^{-1}$, operation with CEM: $P_\text{max}^{CEM} = 1 \times 10^{-5}\,\text{mbar}$, $\text{MDPP}^{CEM} < 4 \times 10^{-14}\,\text{mbar}$, CEM HV = 0–3 000 V, sensitivity $S^{CEM} \sim 10^{-1}\,\text{A}\,\text{mbar}^{-1}$ at CEM HV $\simeq$ 1 100 V, $S^{CEM} \sim 100\,\text{A}\,\text{mbar}^{-1}$ at CEM HV $\simeq$ 2 500 V.

- Sample exchange system connected via DN40CF-F gate valve and DN40CF-F (40 × 42) flange: the sample carrier is electromagnetically guided through the fore vacuum system and the gate valve directly to a fixed position in the sample holder inside the UHV chamber.

- Fore vacuum is achieved by two cryosorption pumps AP 25 (sorbent zeolite CALSIT X5A, operating temperature −196°C (LN_2)), ultimate pressure $10^{-3}\,\text{mbar}$ and pumping capacity 25 l of N_2 (1 000 mbar) each, the pressure $10^{-4}\,\text{mbar}$ can be obtained when the second pump starts after the first pump reaches its ultimate pressure. Pirani gauge Pfeiffer Vacuum

TPR 265: 5×10^{-4}–1 000 mbar, accuracy and reproducibility $\approx 10\%$ of reading and $\approx 2\%$ of reading in the range of 1×10^{-3}–100 mbar, respectively.

- UHV chamber bakeout considerations: Prisma™ maximum bakeout temperature is 300°C (electronics removed), CCG 250°C (magnetic shielding removed), sight glass and other parts up to 400°C, DN63CF-F gate valve (cured Viton seal inside) 250°C with the valve opened and 200°C when the valve is closed. Thus the maximum bakeout temperature applicable to the whole UHV system is 250°C when the TSIP is working.

Several basic vacuum and geometrical considerations of this system follow:

- The criterion of the type of a flow (viscous or molecular) can be assessed with the help of the ratio between the numbers of 'molecules-chamber walls' collisions and 'molecule-molecule' collisions as [62]

$$\frac{N_{\text{mol-wall}}}{N_{\text{mol-mol}}} = \frac{\lambda}{2\,\frac{V}{A}}\,, \tag{18}$$

  where λ is the molecular **m**ean **f**ree **p**ath (MFP) under the given conditions in the system of volume V and internal surface area A. For this system the estimates $V \simeq 3.6 \times 10^3\,\text{cm}^3$ and $A \simeq 1.6 \times 10^3\,\text{cm}^2$ are valid thus in the base pressure of 10^{-9} mbar where the MFP is $\lambda \sim 10^6$ cm the ratio $N_{\text{mol-wall}}/N_{\text{mol-mol}} \sim 10^6$ so the criterion for the molecular flow regime is very well fulfilled. That is true even for the maximum operating pressure of the Prisma™ of 10^{-4} mbar.

- General relationships that govern and explain the performance of any vacuum system are [13, 62]

$$G \equiv PV\,,\;\; Q \equiv \frac{dG}{dt} = \frac{d}{dt}(PV) = P\frac{dV}{dt} + V\frac{dP}{dt}\,,\;\; S_\text{p} \equiv \frac{dV}{dt} \Longrightarrow Q = PS_\text{p} + V\frac{dP}{dt}\,, \tag{19}$$

  where G [mbar l] is defined as the amount of gas inside the chamber, Q $\left[\text{mbar}\,\text{l}\,\text{s}^{-1}\right]$ as the gas load (also understood as the 'throughput' of a vacuum pump or 'mass flow' representing the total number of molecules flowing per unit time) [4] and S_p $\left[\text{l}\,\text{s}^{-1}\right]$ as the pumping speed ('volume flow'). The last relation is the basis for usual vacuum system calculations, *e.g.* for an isolated vacuum container (the 'pump/chamber' valve is closed) the S_p is zero thus the pressure rise (dP/dt) due to various gas loads (permeation, outgassing, diffusion *etc.*) is observed. However, the gas loads resulting from common vacuum processes (see Sect. 4.1.2) enter the system all the time.

- Anyway, the pumping speed S_p experienced by the chamber—the **eff**ective pumping speed—connected to the pump by a conductance C is given by [13, 62]

$$\frac{1}{S_\text{eff}} = \frac{1}{S_\text{p}} + \frac{1}{C} \Longrightarrow S_\text{eff} = \frac{S_\text{p}\,C}{S_\text{p} + C}\,, \tag{20}$$

  thus the effective pumping speed S_eff can be considerably limited by the conductance C when $C \ll S_\text{p}$.

[4] From the definition follows that $Q = Q(T)$.

- A tube with dimensions ϕ and l connecting the vacuum chamber with the pump has a certain conductance C which in the **m**olecular **f**low **r**egime (C_{mfr}) can be calculated as [13, 62]

$$\frac{1}{C^{\mathrm{sh}}_{\mathrm{mfr}}} = \frac{1}{C^{\mathrm{ln}}_{\mathrm{mfr}}} + \frac{1}{C^{\mathrm{orif}}_{\mathrm{mfr}}}\,, \quad C^{\mathrm{orif}}_{\mathrm{mfr}} = \sqrt{\frac{R_0\,T}{2\,\pi\,M_{\mathrm{m}}}}\,F\,, \quad C^{\mathrm{ln}}_{\mathrm{mfr}} = \frac{\pi}{3}\sqrt{\frac{R_0\,T}{2\,\pi\,M_{\mathrm{m}}}}\,\frac{\phi^3}{l}\,, \tag{21}$$

  where $C^{\mathrm{sh}}_{\mathrm{mfr}}$, $C^{\mathrm{ln}}_{\mathrm{mfr}}$ and $C^{\mathrm{orif}}_{\mathrm{mfr}}$ stand for the conductance $\left[\mathrm{cm^3 s^{-1}}\right]$ (V/t units generally) of a **sh**ort and **lon**g tube and an **orif**ice, respectively, F $\left[\mathrm{cm^2}\right]$ is the orifice cross-section. For 'air' (usual residual atmosphere) at 20°C the simple relations $C^{\mathrm{orif}}_{\mathrm{mfr}} \simeq 115\,F$ and $C^{\mathrm{ln}}_{\mathrm{mfr}} \simeq 121\,\phi^3/l$ are valid, C $\left[\mathrm{m^3 s^{-1}}\right]$, F $\left[\mathrm{m^2}\right]$ and ϕ, l [m].

- According to Eq. 21 the tube with the dimensions $\phi_{63} = 63\,\mathrm{mm}$ and $l_{63\mathrm{md}} = 58\,\mathrm{mm}$ connecting the UHV chamber with the TSIP has the conductance $C^{\mathrm{sh}}_{\mathrm{mfr}} \simeq 21.25\,\mathrm{m^3\,s^{-1}} = 21.25 \times 10^3 \mathrm{l}\,s^{-1}$ thus from the Eq. 20 follows that the TSIP effective pumping speed S_{eff} is practically the same as the speed S_{p}, *i.e.* the pump performance is not limited anyhow by the tube. Eq. 19 can then be used for detailed considerations.

- Due to the fact that the fore vacuum system is frequently exposed to air—it is a part of the analysis of every single sample—the water adsorption on the fore vacuum system walls in unavoidable. Further, certainly some part of the water molecules enters the UHV chamber through the gate valve DN40CF-F thus prolonging the pumpdown down to pressure of 10^{-9} mbar and even possibly influencing the Rb compounds samples.

- "The discharge in the TSIP is an intense source of UV light and X-rays and the pump throat should therefore be kept out of line-of-sight with any region where ionization or free photoelectrons is to be avoided" [63]. As can be assessed from Fig. 14 the sample holder can be easily 'seen' by the TSIP and thus some influence of the samples by the photons being emitted from the TSIP is possible. In addition, (T)SIPs are well known for their memory effect which is caused by regurgitation of prepumped gas when pumping a new gas [13, 62].

- TSD and ESD, both significant problems in HCGs, are negligible in the case of CCG [64], however, every ionization gauge may act as low speed pump (via generating ions and capturing them). Modern inverted magnetron CCGs show the pumping speeds in the range 0.01–0.1 $\mathrm{l\,s^{-1}}$. The error caused by the pumping speed of an ionization gauge can be estimated using the following expression [64] $P/P_{\mathrm{gg}} = S_{\mathrm{gg}}/S_{\mathrm{eff}} + 1$, where P, P_{gg} are the pressures in the system and in the **g**au**g**e and S_{eff}, S_{gg} the (effective) pumping speeds of the system and the gauge, respectively. This effect can thus be neglected for this UHV system.

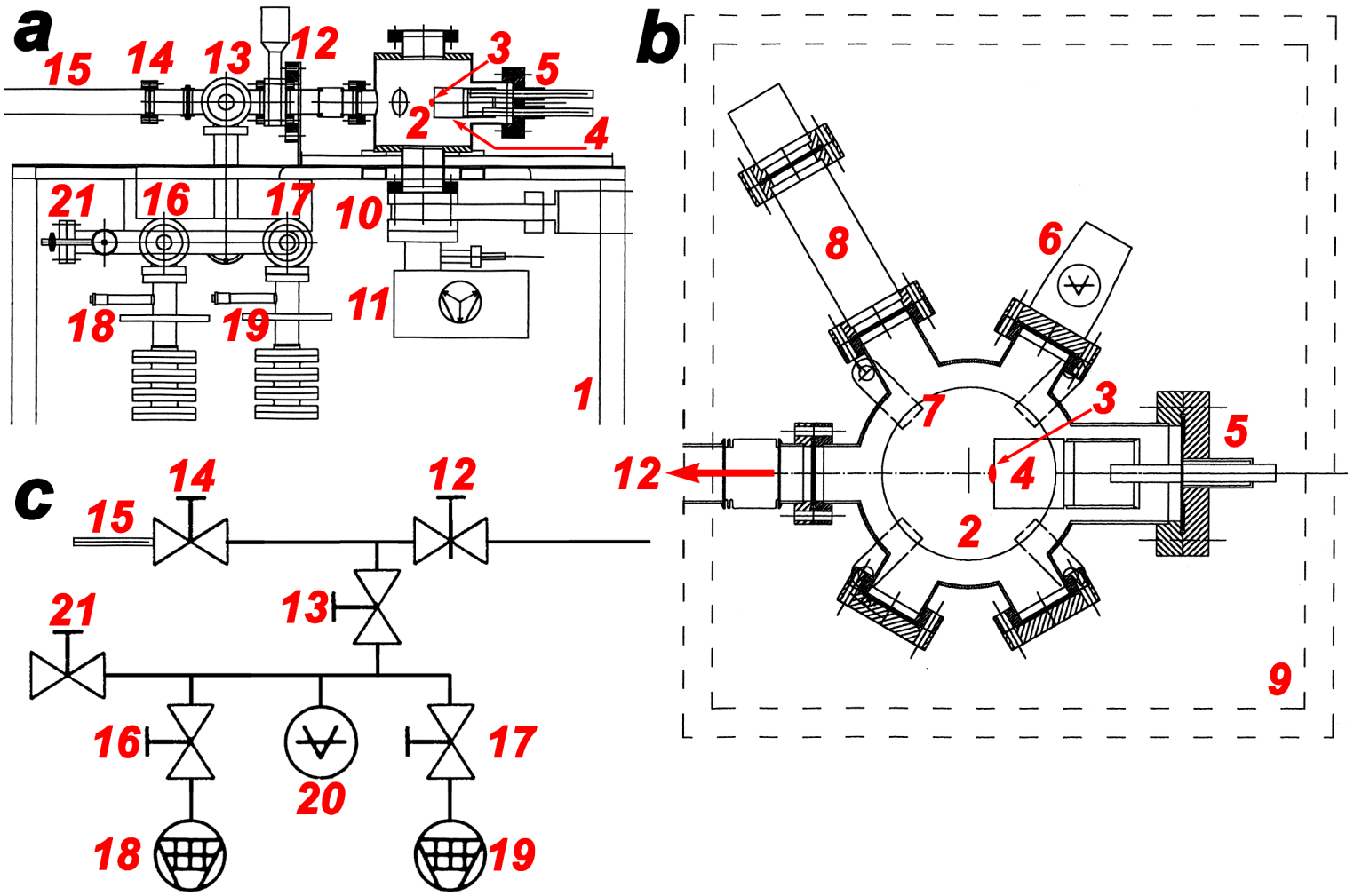

Fig. 13. Drawings of the UHV system at JINR Dubna made by Vakuum Praha Co. [60, 61] (cf. Fig. 14 and Tab. 3): **(a)** side view of the overall vacuum system, **(b)** top view of the UHV chamber, **(c)** scheme of the fore vacuum system. Main components: 1—bench, 2—3.6 l UHV SS six-way cross chamber, 3—sample embedded in the sample carrier, 4—sample holder (DN63CF-F flange) inside the chamber, 5—sample holder electronics system for heating up/cooling down the sample, 6—CCG IKR 270 (DN40CF-F flange), 7—approximate position of the Prisma™ OIS inside the chamber (DN40CF-F flange), 8—Prisma™ rod system, 9—bakeout area indicated by dashed lines, 10—DN63CF-F gate valve, 11—sputter-ion pump IPT 25 (10^{-11} mbar), 12—DN40CF-F gate valve UHV/fore vacuum, 13—HV35 Viton sealed valve, 14—KF40 clamp flange fore vacuum/air atmosphere, 15—sample exchange system, 16, 17—HV35 valves, 18, 19—cryosorption pumps (together 10^{-4} mbar), 20—Pirani gauge TPR 265, 21—HV6 valve fore vacuum/air atmosphere.

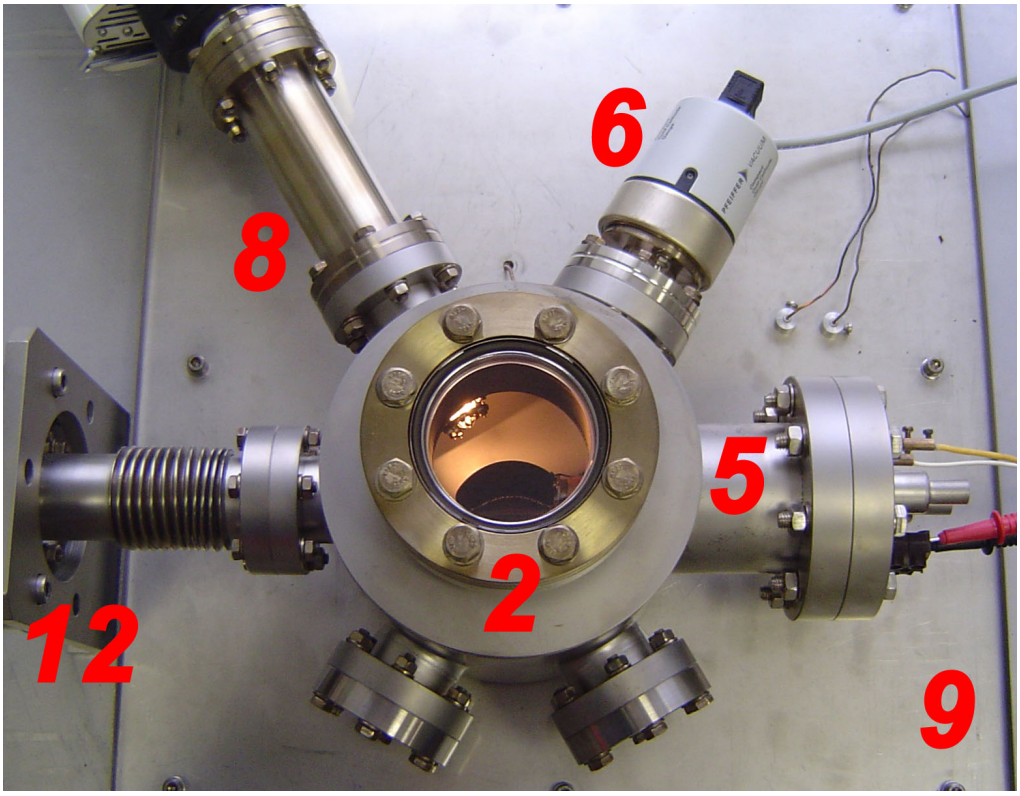

(a)

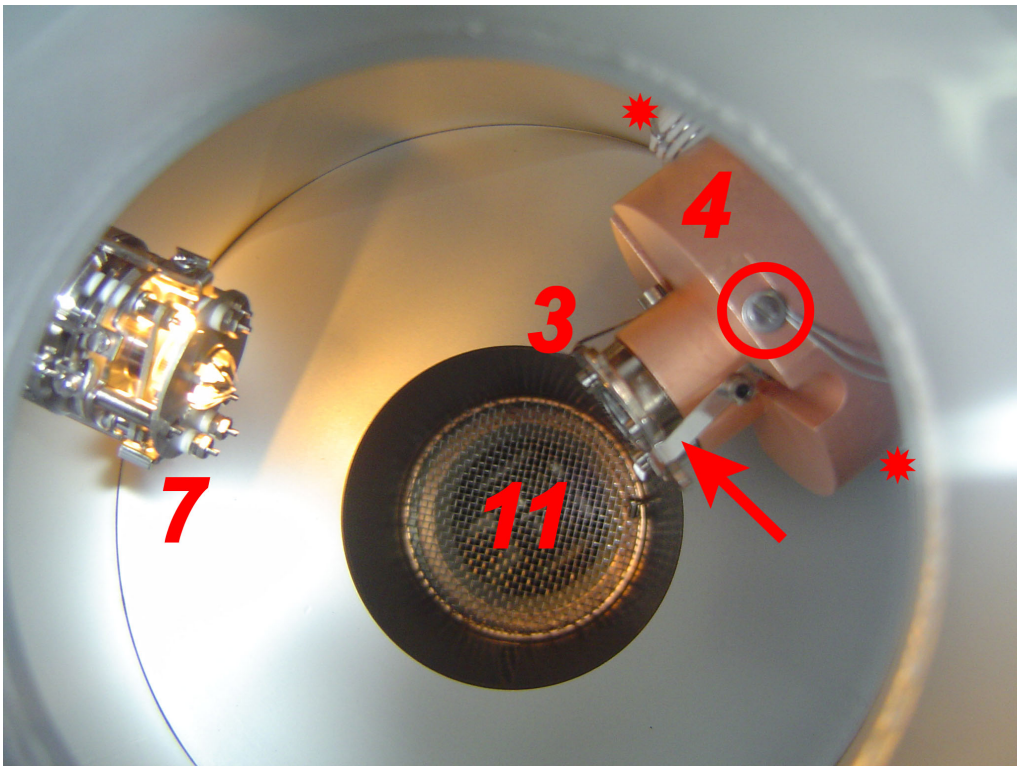

(b)

Fig. 14. Top view of the UHV system at JINR Dubna made by Vakuum Praha Co. [60, 61], the numbers of the indicated components correspond to Fig. 13. **(a)** Inside the UHV chamber there is partly seen the Prisma™ OIS heated to incandescence. **(b)** Detail of the chamber interior shows the mutual positions of the sample and the Prisma™ OIS. The OIS filament 'Fil 2' is in operation. One of the three clamping springs holding the source carrier is pointed by an arrow. Further, the positions of the thermocouple and of the pair of insulants with spiral filaments are indicated by circle and stars, respectively.

Tab. 3. Overview of materials exposed to vacuum in the setup at JINR Dubna [32, 61, 65].

Setup part	Component	Composition
Main vacuum system, pumps and gauges		
UHV chamber and fore vacuum system		
	walls and other parts	SS (*) 1.4301/304, 1.4311/304LN, 1.4541/321
	sight glass	'Alkali Borosilicate' (Kodial)
Sample holder		
	main body	OFHC-Cu (†) 1787/2.0040
	insulants	Macor (46 % SiO_2, 17 % MgO, 16 % Al_2O_3, 10 % K_2O, 7 % B_2O_3, 4 % F)
	spiral filaments	Kanthal (86 % Fe, 12 % Cr, 2 % Al)
Sample carrier		
	main body	OFHC-Cu (†) 1787/2.0040
	clamping springs	Duratherm 600 (Co-Ni-Cr-Mo-W based alloy)
	annular thrust ring	SS
TSIP IPT 25		
	cathodes (strips)	Ti
	anode	SS
	vacuum envelope	SS
Cryosorption pumps AP 25 (LN_2 77 K)		
	vessel body	Al
	sorbent	zeolite (CALSIT X5A)
CCG IKR 270 (all-metal)		
	flange	SS (*) 1.4306/304L
	feedthrough isolation	ceramic (Al_2O_3)
	internal seal	Ag
	anode	Mo
Pirani gauge TPR 265		
	flange	SS
	feedthrough	glass
	filaments	W
RGA Prisma™ QMS 200 M3		
OIS		
	filaments	W
	electrodes and other parts	SS
Rod system		SS
CEM		SiO_2 on a PbO_2 layer
Non-radioactive Rb sample		
Backing		HOPG SPI-2 (C; impurities (ash) ≈ 10 ppm) *or* Al foil

(*) DIN/AISI standard, (†) DIN/Material Number.

- With the DN63CF-F gate valve between the chamber and the TSIP closed a quite rapid rise in the pressure can be observed. This is the result of the outgassing mainly of the Viton seal. The SS outgassing is probably much lower than the one caused by the Viton seal, anyhow, the **i**solation **p**ressure **r**ise (IPR) technique [49, 51] can be easily used to measure the outgassing rates.

- Prisma™ OIS inside the UHV chamber [31, 61]: $r_{\text{OIS}} \simeq 5\,\text{mm}$ (OIS ionization chamber radius), $l_{\text{sm–OIS}} \simeq 45\,\text{mm}$ ('**sam**ple–OIS' distance), $l_{\text{chc–OIS}} \simeq 39\,\text{mm}$ ('**ch**amber **c**enter–OIS' distance), $l_{\text{sm–chc}} \simeq 13\,\text{mm}$ ('**sam**ple–**ch**amber **c**enter' distance) and $\measuredangle(\text{sm–OIS}) \simeq 46°$ (angle between the perpendicular to the **sam**ple surface and the line-of-sight of the OIS).

4.2.2 Linear quadrupole RGA Prisma™

Pfeiffer Vacuum Prisma™ is a common commercial LQMS designed for the partial pressure analysis at pressures below $10^{-4}\,\text{mbar}$. The main technical data of this RGA are summarized in Tab. 4, whereas the results of its factory calibration procedure are shown in Tab. 5. Throughout this work one example of the Prisma™ performance was already depicted in Fig. 10**b**.

The principal parameters which can be tuned by the user—via the system programme QUADSTAR [32]—are the following ones (cf. Fig. 8 where the LQMS parameters interdependencies are sketched with the operating parameters adjustable for Prisma™ highlighted) [5] [32, 66, 67]:

- Electron emission current I_e – the available I_e current range is 0–10 mA with the minimum increment of 0.1 mA, a typical value for obtaining a high RGA sensitivity is 2 mA.

- OIS potential characteristics – the OIS (Fig. 15) potential characteristics experienced by any ion created within the formation chamber by the EI can be directly controlled by the following five voltages (see Tab. 6 and Fig. 16):

  > Ion Ref (V1) – that is the nominal potential on which the ions are formed. The actually effective potential is somewhat lower because of the penetration of the extraction field and the electron volume charge. It is the reference potential for all the other potentials. In general, the V1 potential should be set slightly higher ($\approx 20\,\text{V}$) than the electron energy ('Cathode (V2)' potential). The cathode is thus on a positive potential with regard to ground so that no electrons are emitted to the environment. This prevents interference with the FC of the system and nearby measurement equipment (*e.g.* ionization gauge). Moreover, gases adsorbed in the environment could be emitted through the ESD which could influence the measurement. The following effects of the V1 setting are also influenced by the mechanic tolerances, *e.g.* by the exact cathode position:
  >
  > * at low values (25–40 V) the sensitivity for lower masses is higher, whereas the maximum sensitivity for higher masses is reached with higher values,
  > * the higher the V1 setting the lower the mass discrimination, *i.e.* the sensitivity decreases with higher mass numbers,

[5] The highlighted parameters in Fig. 8 which can be varied for Prisma™ are distinguished as those tuned directly, *i.e.* the programme allows to set these quantities via a direct input (*e.g.* the resolution), and those tuned 'implicitly', *i.e.* they are varied via related quantities (the ion and electron energies via OIS potentials).

  - these relationships become even clearer with higher mass ranges and smaller QMA dimensions,
  - for the purpose of minimizing the mass discrimination, it is advised to select a peak with the highest possible mass for optimizing the ion source parameters.
- Cathode (V2) – the cathode voltage determines the acceleration voltage of the electrons and thus the nominal ionization energy. The actual ionization energy deviates slightly from that value, *e.g.* due to the extraction field. Calibration measurements are required for applications for which the exact ionization energy has to be known. The reference data in spectra libraries are usually referenced to 70 eV.
- Focus (V3) – allows to adjust the maximum peak level for the given conditions. When the V3 potential is modified the V5 potential must be optimized accordingly (if applicable).
- Field Axis (V4) – this is the potential difference between the ionization area (V1) and the QMA. The V4 voltage therefore defines the kinetic energy (velocity) of the ions in the rod system. The higher the value, the higher the peaks. However, the resolution is lower and the peak shape deteriorated. The combined optimization of the V4 potential and resolution should result in a maximum peak level with the desired resolution and a sufficiently good peak shape.
- Extraction (V5) – it accelerates the ions from the ionization area towards the rod system. If the V5 voltage is modified, the V3 potential must also be optimized.

- Resolution – the mass scan over the entire mass range is carried out a with constant resolution set directly by the user, thus the mass discrimination occurs. The resolution can be set by the values 1–255, where the peak width is approximately proportional to the set number, *i.e.* the lower the set number the narrower peaks are observed (well resolved), however, for the better sensitivity and stability of the measured values the wider peaks are advised. Unit resolution usually suffices, *i.e.* the adjacent peaks are just resolved. The value 0 ('OFF') can be also set allowing to measure an integral mass spectrum (DC voltage is turned off).

- RF cable polarity – the resolution and peak shape might be improved by interchanging the RF cables at the QMA. If by reversing the polarity the sensitivity is improved or deteriorated by more than 50% there is a contamination or a mechanic fault.

- Mass scan speed v_{sc} – the speed at which the RGA scans through a range of successive mass numbers, for the 'Scan analog' mode the v_{sc} can take the values 0.200–60 $\mathrm{s\,u^{-1}}$ while for the 'Scan bargraph' mode the values 0.020–60 $\mathrm{s\,u^{-1}}$ are available.

- CEM HV – the high voltage in the range 0–3 000 V can be applied to the CEM, resulting in the amplification of the detected ion current when compared to the FC detection mode. However, there are certain limits above which the CEM detection mode is forbidden to avoid the CEM damage: the maximum operating pressure $P_{\mathrm{max}}^{CEM} = 1 \times 10^{-5}$ mbar, the maximum output current $I_{\mathrm{max}}^{CEM} = 1 \times 10^{-6}$ A [6] and the maximum operating temperature

[6] The CEM output current is directly influenced by the CEM HV applied thus during the application of the CEM HV the care must be taken not to exceed the maximum output current safe for the CEM operation. Anyhow, the Prisma™ possesses an automatic protection against such a CEM overflow.

Tab. 4. RGA Prisma™ QMS 200 M3 (Product No. PT M03 321 121) datasheet [31, 32, 34].

Property	Unit	Specification and values
Operational		
Mass range	u	1–300
Detector type		**F**araday **c**up (FC) / **c**hannel **e**lectron **m**ultiplier (CEM)
Rod system, material,		stainless steel,
radius r_{rod} / length L	mm	3 / 100
Resolution $\Delta(m/z)$		
at the valley, full mass range,	%	< 10,
at 10 % peak height	u	0.5–2.5,
		adjustable to const. peak width $\Delta(m/z)$ throughout entire mass range
Contribution to neighboring peak	ppm	^{4}He / 5 100,
		^{40}Ar / 41 50
Peak ratio reproducibility (*)	%	± 0.5
Sensitivity for Ar (†) S_{Ar}	A mbar^{-1}	FC 1.5×10^{-4},
		CEM 100,
		adj. impl. via parameters setting
Minimum **d**etectable	mbar	FC $< 2 \times 10^{-11}$,
partial **p**ressure (MDPP) (†)		CEM $< 4 \times 10^{-14}$
Maximum operating pressure P_{max}	mbar	FC 1×10^{-4},
		CEM 1×10^{-5}
Ion source		
Design		open type, cylindr. symm., 2 filaments, EI, 'electrodes configuration and potential characteristic ≈ grid IS'
Filament material		tungsten (W)
Electron emission current I_e	mA	0.10–2.00 (0.01 mA)
Potentials	V	'Ion Ref', 'Cathode', 'Focus', 'Field Axis' and 'Extraction', all programmable
Electron energy E_e	eV	adj. impl. via Cathode (V2) potential
Ion energy E_z	eV	adj. impl. via Field Axis (V4) potential
Degassing		via electron bombardment (recomm. at 10 mA, 300 V, $\leq 10^{-7}$ mbar)
Electronics		
CEM arrangement,		off-axis
operating voltage,	V	0–3 000 (1 V)
amplification		10^6 at 2 500 V
maximum permissible current	A	10^{-6}
HF generator frequency f	MHz	1.7
Electrometer amplifier	A	10^{-5}–10^{-12} (full scale),
		fix and autorange
Measurement modes		Scan analog, Scan bargraph, MID, MCD
Meas. cycles		1 / 1–9 999 cycles / repeat
Meas. speed, Scan analog v_{sc},	s u^{-1}	0.200–60,
Scan bargraph, MID dwell	s u^{-1}	0.020–60, 0.010–60
Signal filter		**f**inite **i**mpulse **r**esponse (FIR) filter

All the main accessible technical data are stated. (*) Determined at constant conditions while 8 hours, Ar and N_2 from air, FC detector, 100 u mass range type of Prisma™. (†) No definite conditions of the MDPP nor the sensitivity determination are given.

Tab. 5. RGA Prisma™ QMS 200 M3 (Product No. PT M03 321 121) test report [68].

Property, quantity	Specification and values	
Test gas mixture:	10 % He, 10 % N_2, 60 % Ar, 10 % Kr, 10 % Xe	
P_{residual}	5.00×10^{-9}	mbar
P_0 (total)	1.00×10^{-6}	mbar
P_{Ar}	6.00×10^{-7}	mbar
$P_X, X = \text{He}, \text{N}_2, \text{Kr}, \text{Xe}$	1.00×10^{-7}	mbar
Ion source settings		
Electron emission current I_e	2.00	mA
Filament Fil 1	Fil 2	
Electrodes – potentials [V]:		
(V1) Ion Ref 150	150	
(V2) Cathode 73.0	71.0	
(V3) Focus 11.00	10.25	
(V4) Field Axis 6.38	6.38	
(V5) Extract 40	41	
Mass scan parameters		
CEM HV	1 130	V
Scan mode	SCAN-F	
Scan speed v_{sc}	1	s u^{-1}
Resolution	53	
Amplifier	Offset ON	
RF supply polarity	inverse	
FC mode sensitivity for Ar (*)		
$H^{FC}_{\text{Ar}}(m/z\ 40)$	4.10×10^{-10}	A
$S^{FC}_{\text{Ar}}(P_{\text{Ar}}, P_0) = \left[H^{FC}_{\text{Ar}}(m/z\ 40)\right] / P_{\text{Ar}} =$	6.83×10^{-4}	A mbar^{-1}
FC mode sensitivities for other gases		
N_2 $(m/z\ 28)$	5.50×10^{-4}	A mbar^{-1}
Xe $(m/z\ 132)$	8.43×10^{-5}	A mbar^{-1}
CEM mode sensitivity for Ar at HV 1 130 V (*)		
$H^{CEM}_{\text{Ar}}(m/z\ 40)$	7.90×10^{-7}	A
$S^{CEM}_{\text{Ar}}(P_{\text{Ar}}, P_0) = \left[H^{CEM}_{\text{Ar}}(m/z\ 40)\right] / P_{\text{Ar}} =$	1.32	A mbar^{-1}
CEM mode sensitivities for other gases at HV 1 130 V		
He $(m/z\ 4)$	1.00×10^{-1}	A mbar^{-1}
N_2 $(m/z\ 28)$	1.58	A mbar^{-1}
Kr $(m/z\ 84)$	5.60×10^{-1}	A mbar^{-1}
Xe $(m/z\ 132)$	1.80×10^{-1}	A mbar^{-1}
CEM mode gain at HV 1 130 V		
N_2 $(m/z\ 28)$	$\approx 3 \times 10^3$	
Ar $(m/z\ 40)$	$\approx 2 \times 10^3$	
Xe $(m/z\ 132)$	$\approx 2 \times 10^3$	

(*) Only the case of S^{FC} (and S^{CEM}, resp.) for Ar is originally included in the report. Sensitivities for the other gases are calculated in the same way as in the case of Ar, all the accessible data from the test report are considered. The values of gain are the ratios of CEM mode readings to FC mode readings.

$T_{\max}^{CEM} = 120°C$ (during the **bake**out when the Prisma™ is turned off the maximum temperature $T_{\text{bake}}^{CEM} = 300°C$ can be applied). The amplification ratio is limited by the dark current in the active layer. The FC operation reduces the system related conversion errors (instability, m/z dependence *etc.*) of the CEM. The value of CEM gain G of 10^6 at 2.5 kV reported in [31, 32] is in good agreement with the general $G = G(\text{CEM HV})$ tendency found in literature, cf. Fig. 11**a**.

- Several automated tuning procedures are built-in:
  - > Mass scale calibration – the peak maxima of a few defined masses are accurately determined and the positions of the remaining masses are interpolated or extrapolated linearly.
  - > Background measurement ('Zero gas') – enables to determine the residual gas background that is found in any analysis chamber. The ion currents determined this way can be then subtracted in all subsequent measurements.
  - > RGA-offset calibration – determines all necessary correction values to eliminate offsets of the measure amplifier under different conditions. For that, the ion current is measured on a specified m/z value (m/z 5.5 default).
  - > Gas specific sensitivity calibration – a typical calibration procedure is carried out, after which the concentrations of the individual gas components from the recorded mass spectrum are automatically calculated.
  - > Peak shape optimizer – it allows to shape peaks by varying the ion source voltages, to compare the shapes of two peaks close to their maximums and to determine mass number and relative intensity precisely.
  - > Degas control – for degassing the current filament ('Fil 1' or 'Fil 2', see Tab. 6) of the OIS.

Tab. 6. RGA Prisma™ OIS main parameters settings [31, 32, 34].

Property, quantity			Unit	Range of values	
Filament #				Fil 1 / Fil 2 / Fil 1+2	
Electron emiss. curr. I_e			mA	0.1–2	(0.01 mA)
I_e for degassing			mA	0–10	(0.1 mA)
Electrode name		Ref. direction			
V1	Ion Ref	0–V1	V	105–150	(1 V)
V2	Cathode	V1–V2		0–100	(0.5 V)
V3	Focus	V1–V3		0–30	(0.13 V)
V4	Field Axis	V1–V4		0–15	(0.13 V)
V5	Extraction	V1–V5		0–150	(1 V)

The minimum incremental values are quoted in the parentheses.

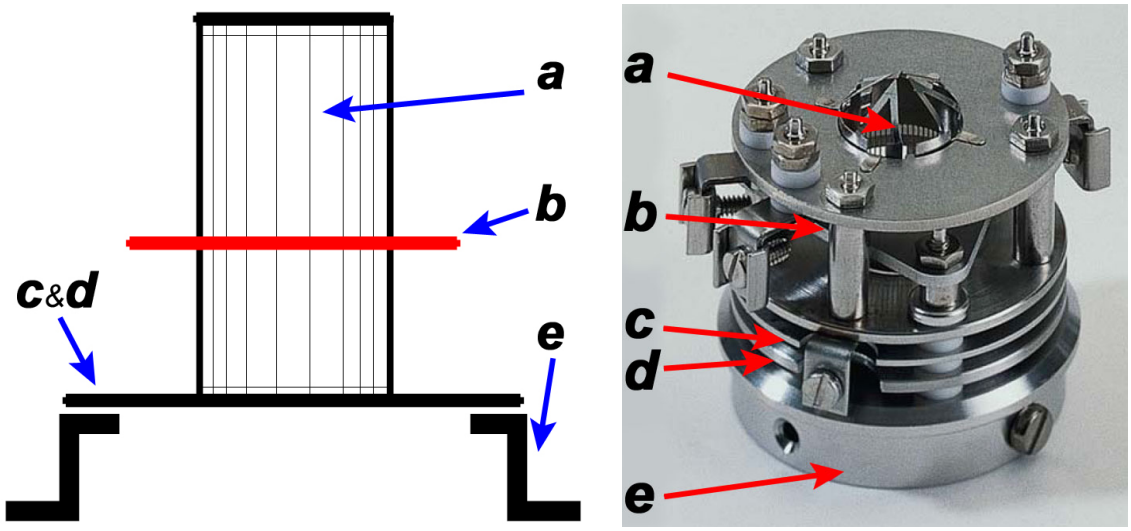

(a) (b)

Fig. 15. RGA Prisma™ grid OIS [31, 32, 34]. Schematic drawing **(a)** and photograph **(b)** show the main parts: *a)* ion formation chamber (open to environment), *b)* filaments around the grid structure (hidden on the right figure), *c)* extraction lens system, *d)* focus lens system, *e)* base plate, connection to the QMA.

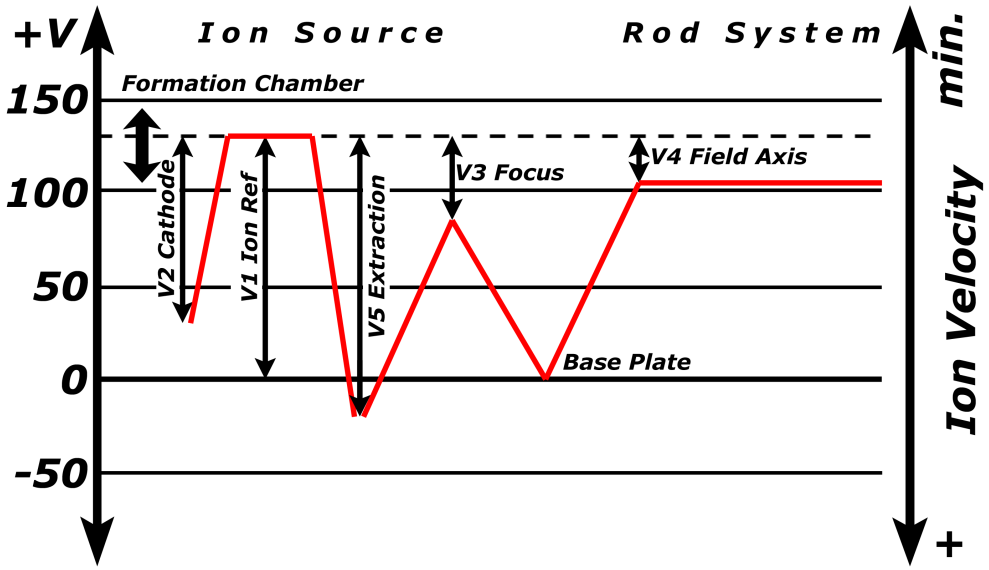

Fig. 16. Prisma™ OIS potential arrangement [31, 32, 34]. The potential V1 (the range 105–150 V indicated by bold arrow) is the reference (dashed line) for the other potentials V2–V5. The maximum ranges of these potentials are depicted as thin arrows, cf. Tab. 6. The red full line shows the resulting overall potential characteristics. A qualitative dependence of ion velocity as acquired by an ion created and accelerated in the OIS is indicated on the right.

4.3 Non-radioactive Rb release investigation

The timetable of the measurements carried out at JINR Dubna can be summarized as follows:

1. after the transport from Prague in August 2003 the whole vacuum system with the devices has been assembled at place,
2. first, rather introductory, RGA investigations of the non-radioactive Rb samples prepared by vacuum evaporation onto a HOPG backing proceeded,
3. some attempts to analyze the possible escape of ^{83m}Kr and ^{83}Rb from small radioactive ^{83}Rb/^{83m}Kr sources were made in spring 2005,
4. at 15.12.2005 new measurements with massive non-radioactive Rb samples in the form of drops on Al foils have started,
5. at 2.2.2006 the malfunction of the first Prisma™ OIS filament occurred,
6. further, till 20.2.2006 the second filament 'Fil 2' was used instead 'Fil 1'.

The first **m**easurements of the vacuum evaporated samples will be further designated as 'M1' while the second series of the measurements of the samples in the form of drops will be called 'M2'.

Both the M1 and M2 results will be presented and compared in this subsection. As the M1 measurements have not yielded satisfactory answer to the question of the Rb release, the M2 series was meant as an improvement of the first investigations. Initially, the M2 series was meant to examine the Rb escape from vacuum evaporated samples as well but with much better reliability. Anyhow, as the investigation of the M2 samples prepared from drops has not given yielded any Rb signal, the vacuum evaporation was not attempted further. The measuring procedure in both cases—M1 and M2—was the same, the only difference were the samples and the operating parameters of the Prisma™ used for scanning the UHV atmosphere. The resolution, mass scanning speed and the CEM gain were optimized. Thus preferentially the M2 results will be shown and where appropriate, compared to M1 results.

The whole sequence of the non-radioactive Rb samples handling and measurement can be summed up as follows:

- sample preparation and storage on air in Petri dishes,
- transport of the sample fixed in a sample carrier through the fore vacuum system into the UHV chamber via the sample exchange system (Fig. 13):
  1. connection of the sample exchange system to the fore vacuum via the KF40 clamp flange 'fore vacuum/air atmosphere',
  2. pumpdown of the fore vacuum system by two cryosorption pumps to a pressure of 10^{-4}–10^{-3} mbar (about 2 hours),
  3. connection of the fore vacuum system and the UHV chamber via the DN40CF-F gate valve,
  4. insertion of the sample carrier into a fixed position in the holder (Fig. 14),
  5. separation of the UHV chamber from the fore vacuum system,

6. pumpdown of the UHV chamber by the TSIP from the pressure 10^{-4}–10^{-3} mbar to the base pressure of 10^{-9} mbar (about 10 hours).

- residual atmosphere analysis with the help of the Prisma™ during which the UHV chamber is continuously pumped by the TSIP,
- transport of the sample out of the UHV chamber via the sample exchange system after the fore vacuum system pumpdown.

4.3.1 Solid Rb samples

The M1 samples have been prepared at JINR Dubna by vacuum evaporation onto a HOPG backing of 10 mm in diameter [65] at temperature of about 800°C and vacuum of 10^{-5} mbar produced by an oil-sealed pump.

The rubidium nitrate $RbNO_3$ water solutions of the Rb^+ cation concentrations $1\,\mathrm{mg\,ml^{-1}}$ have been prepared and placed on molybdenum (Mo) or tantalum (Ta) boats with the help of a micropipette. The boats made from Mo have been chosen as the Mo is considered as the most suitable material for the vacuum evaporation of the metallic Rb, though, in this case Rb compounds are involved. The boats made from Ta have also been used as this type has been utilized in works [11, 12] where a negligible ^{83}Rb and ^{83m}Kr escape has been observed from the ^{83}Rb/^{83m}Kr sources (≈ 1 ng) prepared by the vacuum evaporation from Ta boats.

Three different amounts of $0.5, 5$ and $50\,\mu$l have been produced in this way in order to obtain $0.5, 5$ and $50\,\mu$g of Rb on the boats. The evaporation of water was supported by an IR-lamp. Finally, the vacuum evaporation technique was accomplished to achieve HOPG backings coated with Rb films. The samples have been then stored in an atmosphere with a certain level of a humidity so according to reactions 3, 4 and 5 quoted in Sect. 3.3 the 'final' form of the Rb compounds is ('should be') the rubidium carbonate Rb_2CO_3. However, the 1 monolayer (residual gases) formation time in the vacuum of 10^{-5} mbar is of the order 0.1 s [13]. Thus certainly a number of other compounds is making additional layers on the backing.

From the geometrical considerations it follows that the vacuum evaporation efficiency was (7 ± 2) % thus the amounts of about $0.035, 0.35$ and $3.5\,\mu$g of Rb have been deposited on the backings. These correspond to the amounts of 23 MBq, 230 MBq and 2.3 GBq of the radioactive ^{83}Rb.

The M2 samples have been prepared from rubidium carbonate Rb_2CO_3 water solutions of various Rb^+ cation concentrations [16] of 6.6, 33.0, 179.3, 206.2, 325.9 and $362.0\,\mathrm{mg\,ml^{-1}}$, respectively. The purity of the Rb_2CO_3 powder (Fluka Co.) was better than 99.0 % and redistilled water was used. One $30\,\mu$l drop of the solution was placed on a clean disc of Al (diameter of 10 mm, thickness of 0.05 mm) with the help of a micropipette. The evaporation of water was supported by an IR-lamp. In this way, firstly the samples of the highest concentration of $362.0\,\mathrm{mg\,ml^{-1}}$ were produced and examined in the UHV. The net weights of two such samples were determined as 11.8 and 12.4 mg, respectively, thus the samples contained about 8.7 and 9.2 mg of Rb^+ cations. The difference between the stated values and the expected value of about 11 mg of Rb^+ cations, which one would expect after the drying of $30\,\mu$l drop of the solution, can be ascribed to the fact that during the manipulation between the drying and weighing some crystals of the substance have simply 'fallen off'.

Obviously, the M1 samples were not discernible on the HOPG backings, however, the massive M2 samples were easily visible on the Al foil. Its form, thick layer consisting of white crystals, remained the same in UHV as on air. No abrupt change of the appearance was observed during

the whole exposure of the M2 sample to the UHV, anyhow, accidentally some material could fall off during the inserting of the sample to the UHV chamber via the fore vacuum system.

4.3.2 Mass spectra

The M2 series proceeded in this way:

1. A thorough 49 h bakeout at about 250°C of the UHV chamber was performed.
2. After cooling down of the system the Prisma™ and CCG were mounted and the composition of the UHV ($\approx 4 \times 10^{-9}$ mbar and better) was mass scanned—M2-1 spectra—with default as well as with various settings (for both Fil 1 and Fil 2, but each in operation separately) of the Prisma™ operating parameters. The default Prisma™ OIS settings are stated in Tab. 5.
3. An empty sample carrier was inserted into the UHV chamber and again the residual atmosphere was analyzed (M2-2 spectra). The effect 'M2-2 − M2-1' was obtained by a simple subtraction of typical M2-1 spectrum from the M2-2 one measured with the same parameters.
4. The Rb sample embedded in the sample carrier was inserted into the system and any 'Rb signal' was looked for in the mass spectra—M2-3—taken for various Prisma™ settings, *i.e.* any mass peaks due to any Rb compound were looked for in the effect 'M2-3 − M2-2'.
5. Malfunction of the Prisma™ OIS filament Fil 1 occurred and further the Fil 2 was used instead, however, from M2-1 it was deduced that the Fil 2 was not working properly due to possible misalignment or severe contamination [67].
6. The Rb sample was resistively heated in the holder up to $\simeq 250$°C in order to support its desorption (TSD) and thus any Rb release, however, the spectra—M2-4—were obtained using the Fil 2 thus the reliability of these data is disputed. In the effect ascribed naturally to the increased desorption rates, supported by the heat, no Rb signal was found. M2-4 spectra are not taken into account hereafter.

It should be noted that no calibration procedure of the whole UHV setup was done so all the data were obtained in the form of ion currents [A] in the dependence of the m/z values. The mass scale was calibrated prior to every measurement series. For the mass scans of the UHV composition mainly the Prisma™ CEM operating mode was used as in the 10^{-9} mbar range there were very low ion currents to be detected. The optimum value of the CEM HV was found to be about 2 500 V, providing efficient amplification of the ion currents but still causing reasonable noise at the baseline. The FC operating mode was used to check the CEM gain stability on the major peaks discernible in the spectra taken with the FC. All the spectra were obtained using the built-in FIR filter in order to eliminate the superimposed noise from the raw electrometer signal [32, 67]. In order to obtain the minimum noise, the 'slowest' scanning ($60\,\mathrm{s\,u^{-1}}$) was chosen.

In addition, the resolution was set to the value of 40 or lower (from the available range of 1–255). At higher values of resolution the neighboring mass peaks are not well resolved and rather than individual peaks the fluctuations of the baseline are detected [67]. In this way, a reasonable compromise between the resolution and the sensitivity was chosen. The Prisma™ OIS parameters settings (I_e and V1–V5) were varied in order to obtain some higher sensitivity

Tab. 7. Rb compounds which may occur in the UHV system and be detected by the Prisma™.

Molecular masses, rel. nat. ab.'s		^{85}Rb	$^{85\,\&\,87}$Rb	^{87}Rb
$RbNH_2$	u	100.9		102.9
	%	100		38.6
$RbOH$ (*)	u	101.9		103.9
	%	100		38.6
RbO_2	u	116.9		118.9
	%	100		38.6
$RbNO_3$	u	146.9		148.9
	%	100		38.6
Rb_2O (*)	u	185.8	187.8	189.8
	%	100	77.1	14.9
Rb_2O_2	u	201.8	203.8	205.8
	%	100	77.1	14.9
Rb_2CO_3 (*)	u	229.8	231.8	233.8
	%	100	77.1	14.9

(*) The most probable compounds are RbOH, Rb_2O and Rb_2CO_3 [16, 21, 69].

than the one determined by the default settings, anyhow, the values stated in Tab. 5 were found to be optimum. The V4 (Field Axis) potential was set to zero when looking for the 'surface molecules' (ESD ions). Substantial changes of the ion output were naturally obtained with varying the V2 (Cathode) potential and thus the ionization energy of the electrons emitted from the OIS filament. However, the default value of the potential V2 was used. As the area of a mass peak is strongly dependent on the actual RGA settings and is thus hardly reproducible, it is a common practice [67] to take only the peak height into account.

The following examples of the M2-1 spectra are depicted: Fig. 17 shows a mass scan performed under typical operating parameters of Fil 1 and Fil 2, in Fig. 18 the ESD ions detected during the (separate) operation of Fil 1 and Fil 2 are seen. Fig. 19 illustrates the effect of various CEM HV values. The typical 'M2-2 − M2-1' effect is presented in Fig. 20 while the typical 'M2-3 − M2-2' effect is shown in Fig. 21. For comparison of the M1 and M2 series, Fig. 22 illustrates the typical scans of Rb samples in both cases.

In the M2-3 spectra obtained all the Rb compounds listed in Tab. 7 were looked for. This search is made substantially easier by the help of the isotopic composition of any 'RbXY' and 'Rb_2XY' compound as there are two naturally occurring Rb isotopes ^{85}Rb and ^{87}Rb. The ratio of their natural abundances is (Tab. 1) 100 : 38.6 thus the ions of any '$RbXY^+$' and 'Rb_2XY^+' ions should be revealed in the mass spectrum (neglecting the isotopic effect of other elements present in the Rb compounds) by the presence of the two peaks on positions $m/z\,X$ and $X + 2$ with the heights [A] in the ratio 100 : 38.6 in the case of the '$RbXY^+$' ion or of the three peaks on $m/z\,X, X + 2$ and $X + 4$ positions with the heights ratio of 100 : 77.1 : 14.9 in the case of the 'Rb_2XY^+' ion. In this second case of the 'Rb_2XY^+' there is simply a double probability of the combining the two Rb isotopes, '^{85}Rb & ^{87}Rb' and '^{87}Rb & ^{85}Rb'. This manner of peak

identification actually omits the m/z-dependencies of the ionization, transmission and detection processes within the LQMS, on the other hand, the difference of several m/z values can be considered insignificant.

In all the mass spectra the major component is the H_2^+ peak ($m/z\,2$), followed then by the peaks on $m/z\,28$ (CO^+, CO_2^+ and N_2^+ contributions [24, 31]), $m/z\,16$ (O_2^+, H_2O^+, CO^+ and CO_2^+), $m/z\,18$ (H_2O^+), $m/z\,12$ (CO^+ and CO_2^+) *etc.*, representing a typical residual atmosphere of a well baked SS UHV system. From the ratio $H_{H_2}(2)/P_0 \simeq 6 \times 10^{-7}\,\mathrm{A}/5 \times 10^{-9}\,\mathrm{mbar} \simeq 100\,\mathrm{A\,mbar^{-1}}$ (Fig. 17)it can be seen that the CEM mode sensitivity at CEM HV = 2 500 V corresponds well with the reported value [31].

Further, in Fig. 17 the groups of W^+ peaks ($m/z\,180\,(0.4\,\%)$, $182\,(86.5\,\%)$, $183\,(46.7\,\%)$, $184\,(100\,\%)$, and $186\,(92.8\,\%)$) and W^{+2} (m/z 90–93 with ratios corresponding to the W^+ group) resulting from the tungsten filament evaporation are easily discernible. Some interference of the W^+ group with possible Rb_2O^+ signal (Tab. 7) could be distinguished on the basis of a different origin of the peaks—heating the sample would probably support the release of Rb_2O^+ (among others) but the filament temperature would not be influenced in any way thus the 'constant W^+ background' could be subtracted from the both scans ('cold' and 'hot' sample) in order to reveal the possible Rb_2O^+ signal [66]. As the usual practise in modern RGA ISs is to keep the total I_e current constant by dynamically adjusting the operating temperature of the filament(s), the heights of the W^+ and W^{+2} peaks may possibly fluctuate.

From Fig. 17 it was deduced that the Fil 2 is not working correctly due to some misalignment or severe contamination [67]. The OIS filaments are heated up to about 2 000°C and thus the observation of the W^+, W^{+2} and even W^{+3} mass peak groups with Fil 1 is normal. On the other hand, the absence of those peaks during the Fil 2 operation indicates some problem. It is also interesting that the Fil 1 and Fil 2 scans of the Prisma™ OIS surfaces differ Fig. 18 as well. The noise (baseline) is higher in the case of Fil 2.

Fig. 19 clearly illustrates that increasing the CEM HV produces higher ion signals and thus improves the Prisma™ sensitivity, however, the higher the CEM HV the higher noise and instabilities are encountered [32, 67]. An optimum CEM HV value of about 2 500 V was chosen for further use.

The 'M2-2 − M2-1' effect can be ascribed to the deterioration of the vacuum during the introduction of the empty sample carrier and to the outgassing of the carrier itself. The 'M2-3 − M2-2', where any Rb signal was looked for, was similar to the 'M2-2 − M2-1' one. In all the spectra taken with various Prisma™ settings *no signal on any Rb compound m/z position* has been observed when compared to the background (M2-2), *i.e.* no doublet nor triplet of peaks with the appropriate height ratios has been found. The search was not restricted only to the m/z positions quoted in Tab. 7 but the whole mass spectrum has been examined, however, no Rb compound signal has been found.

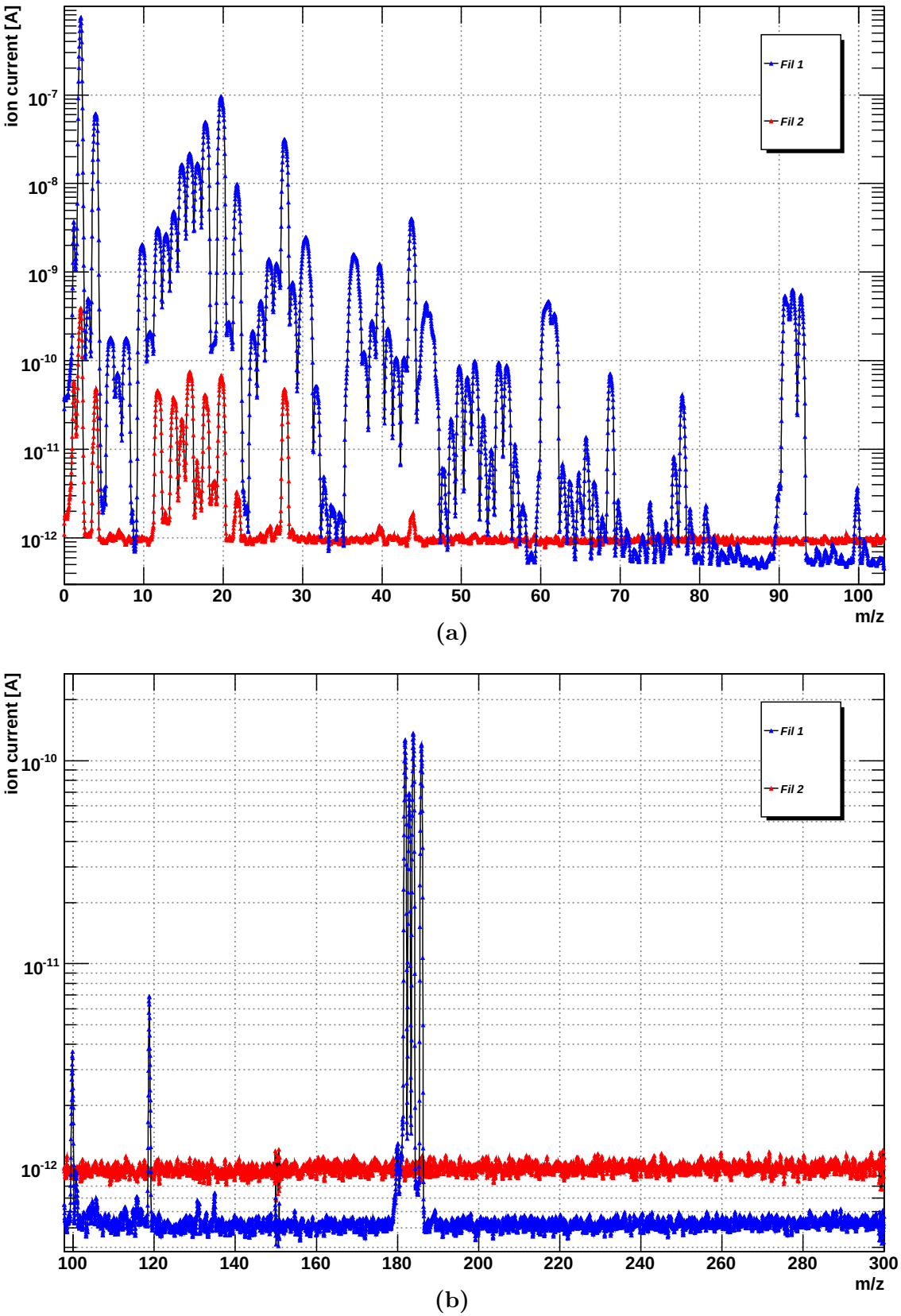

Fig. 17. Mass scan of the UHV chamber after 49 h bakeout measured with Prisma™ set to default values of OIS parameters, resolution 40, scan speed 60 s u^{-1} and CEM HV 2 500 V. Blue color – Fil 1, red – Fil 2. Part **(a)** shows m/z 0–100 region, part **(b)** m/z 100–300. Note the increased noise and the absence of W^{+}, W^{+2} and W^{+3} groups of peaks at about m/z 184, 92 and 61, respectively, for the case of Fil 2.

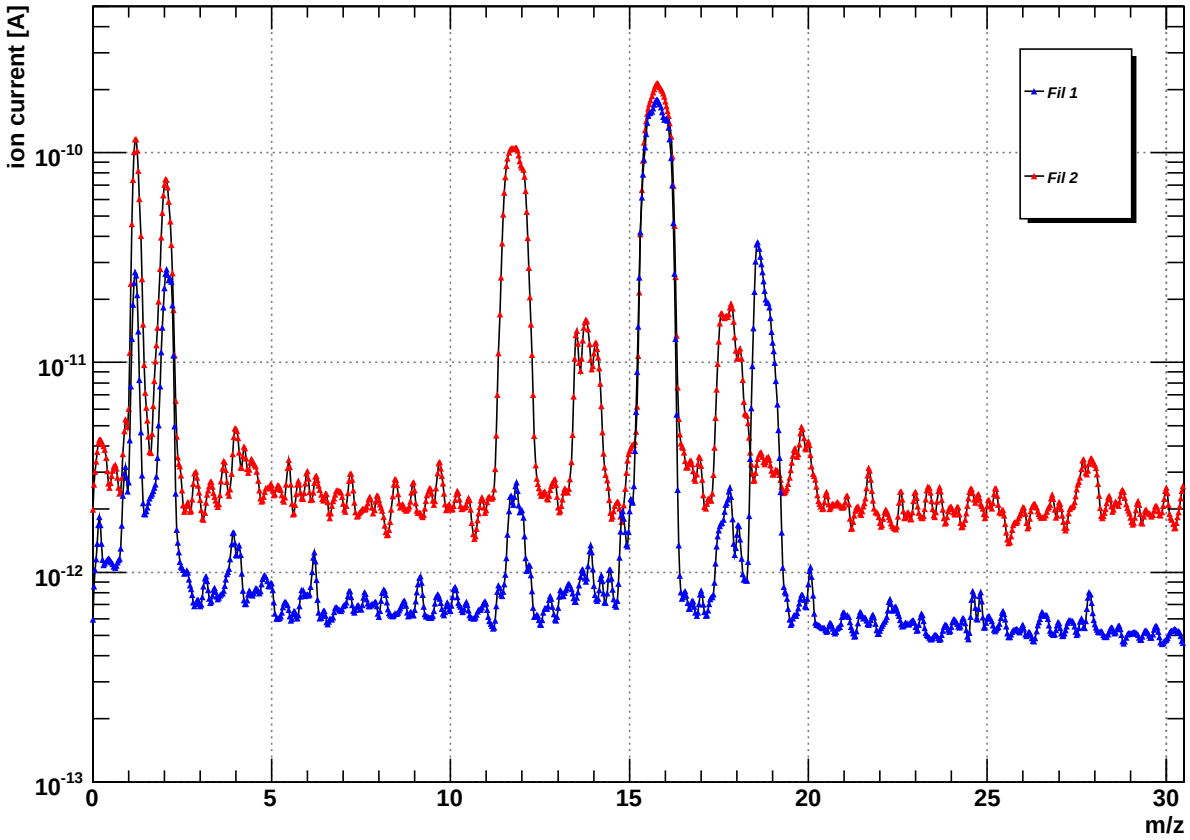

Fig. 18. ESD ions observed during the operation of Fil 1 (blue) and Fil 2 (red), respectively, corresponding to the molecules adsorbed on the OIS surfaces. Potential V4 was set to zero while all the remaining parameters were kept unchanged. Above m/z 30 no peaks were observed. Cf. Sect. 4.1.2.

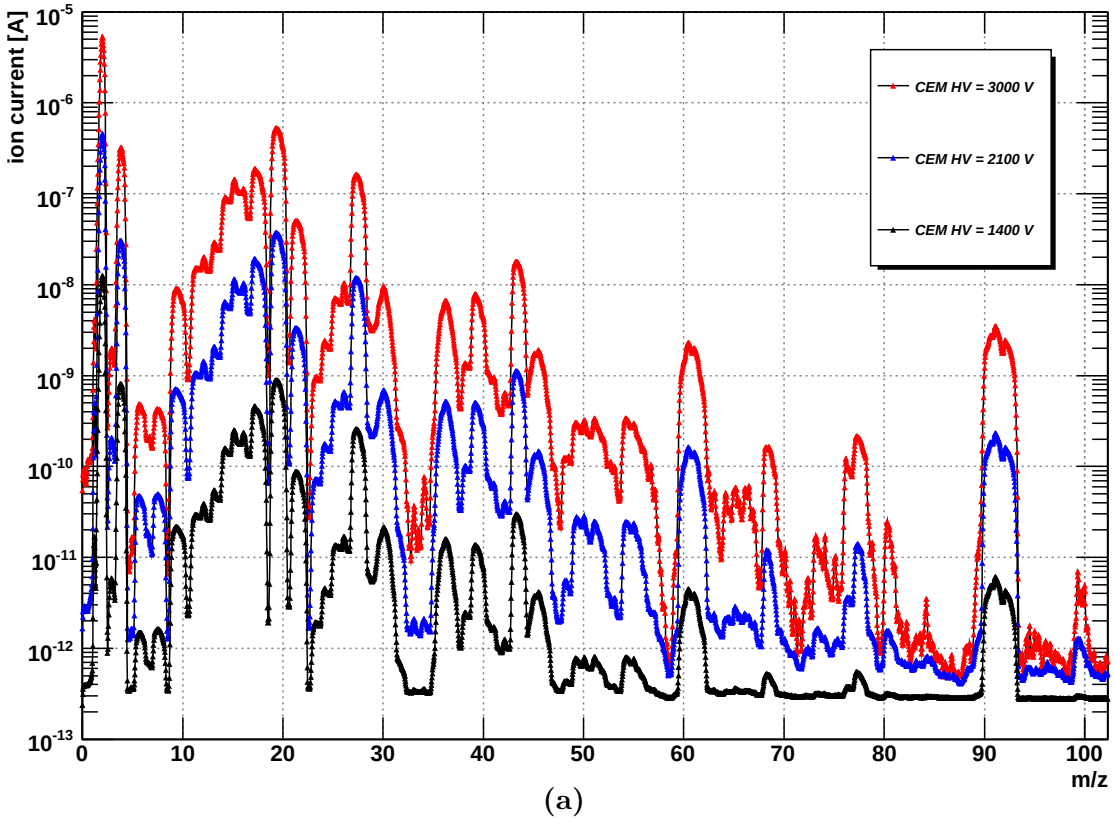

(a)

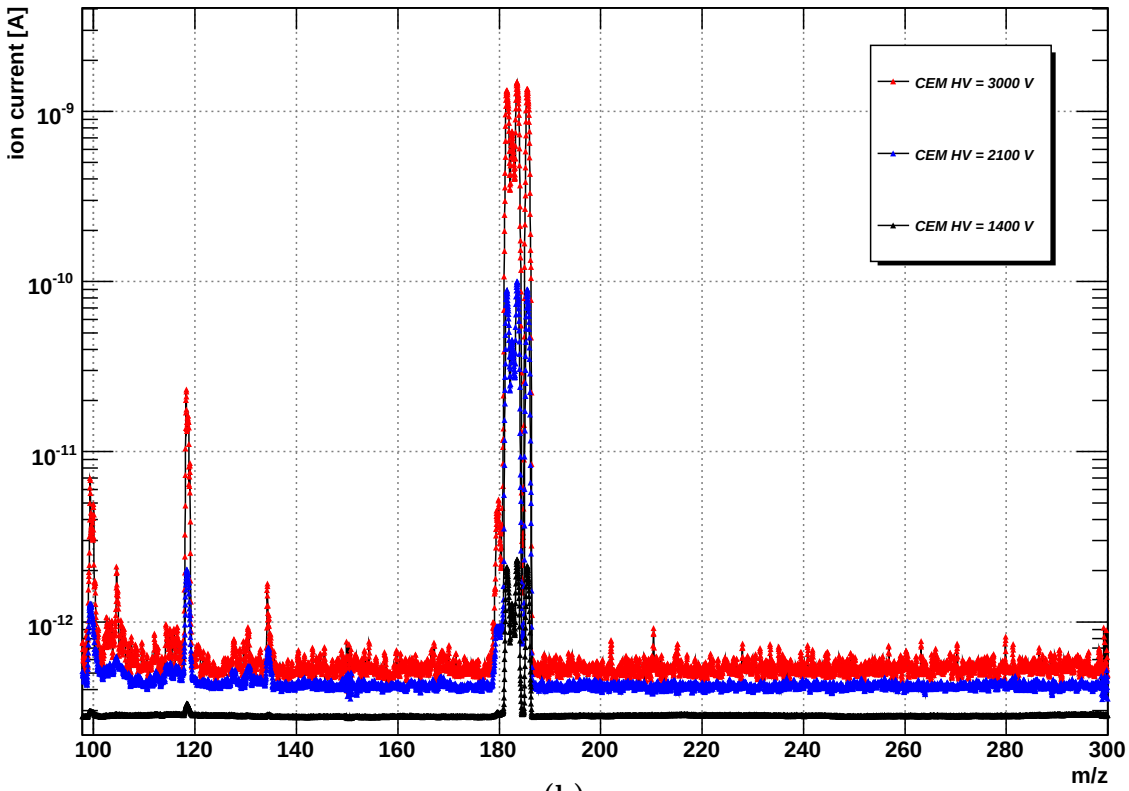

(b)

Fig. 19. Mass scan of the UHV chamber after 49 h bakeout measured with Prisma™ set to default values of OIS parameters, resolution 40, scan speed 60 s u^{-1}, operation with Fil 1. CEM HV 1 400 V – black color, 2 100 V – blue, 3 000 V – red. Part **(a)** shows m/z 0–100 region, part **(b)** m/z 100–300. The increase of the signal as well as of the noise is clearly seen.

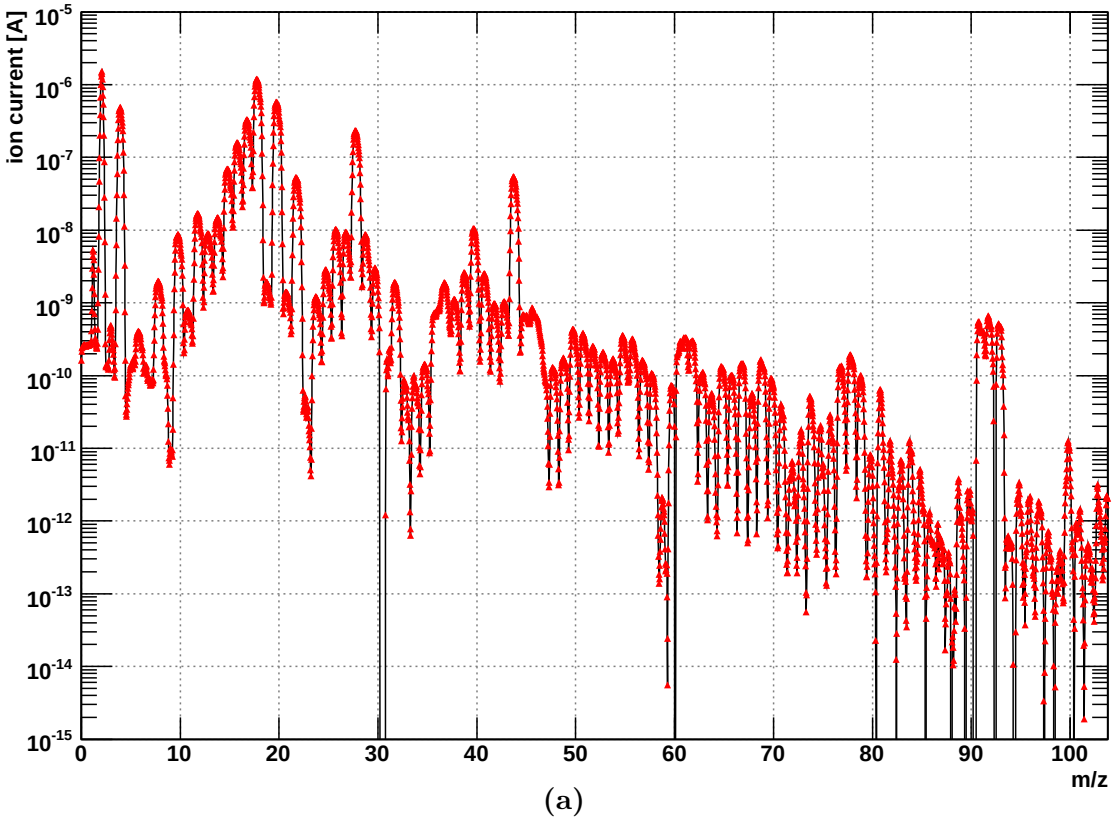

(a)

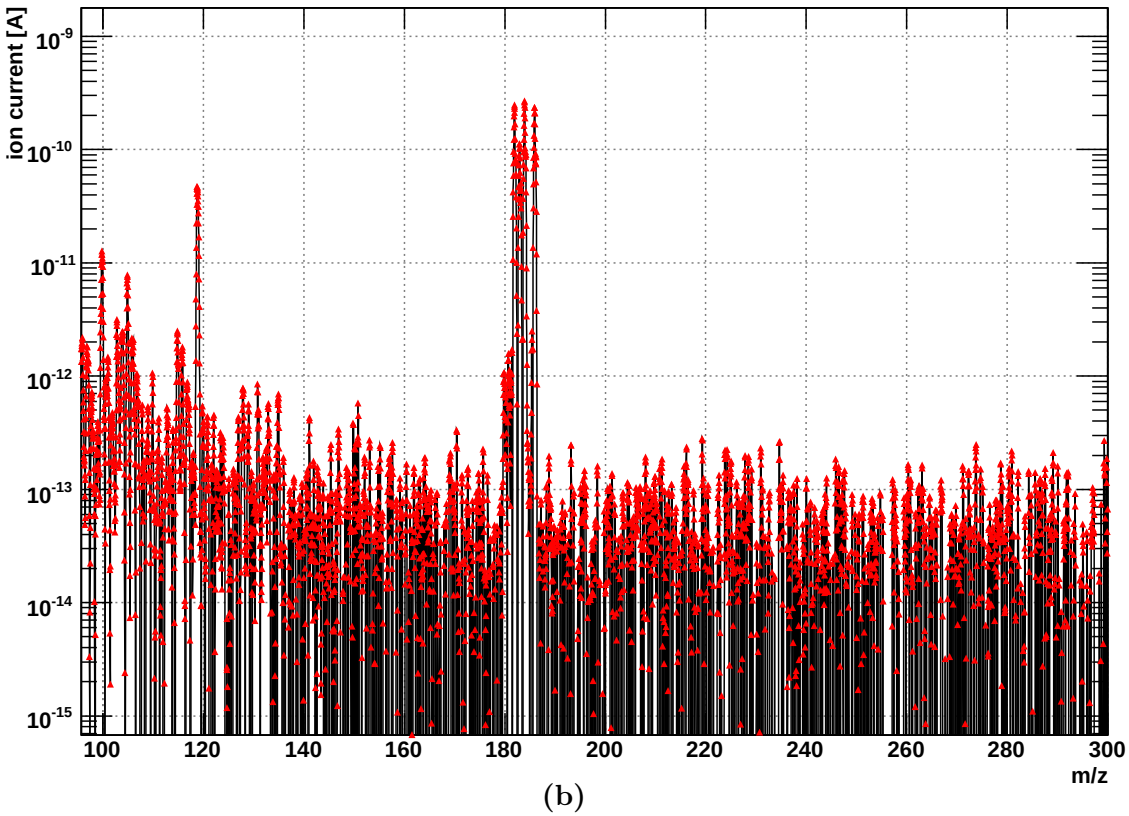

(b)

Fig. 20. The 'M2-2 − M2-1' effect—obtained as a simple subtraction of M2-1 spectrum from M2-2 one—showing the difference between the composition of chamber with sample carrier and empty chamber. Measured with Prisma™ set to default values of OIS parameters, Fil 1 in operation, resolution 40, scan speed 60 s u^{-1} and CEM HV 2 500 V. Part **(a)** shows m/z 0–100 region, part **(b)** m/z 100–300.

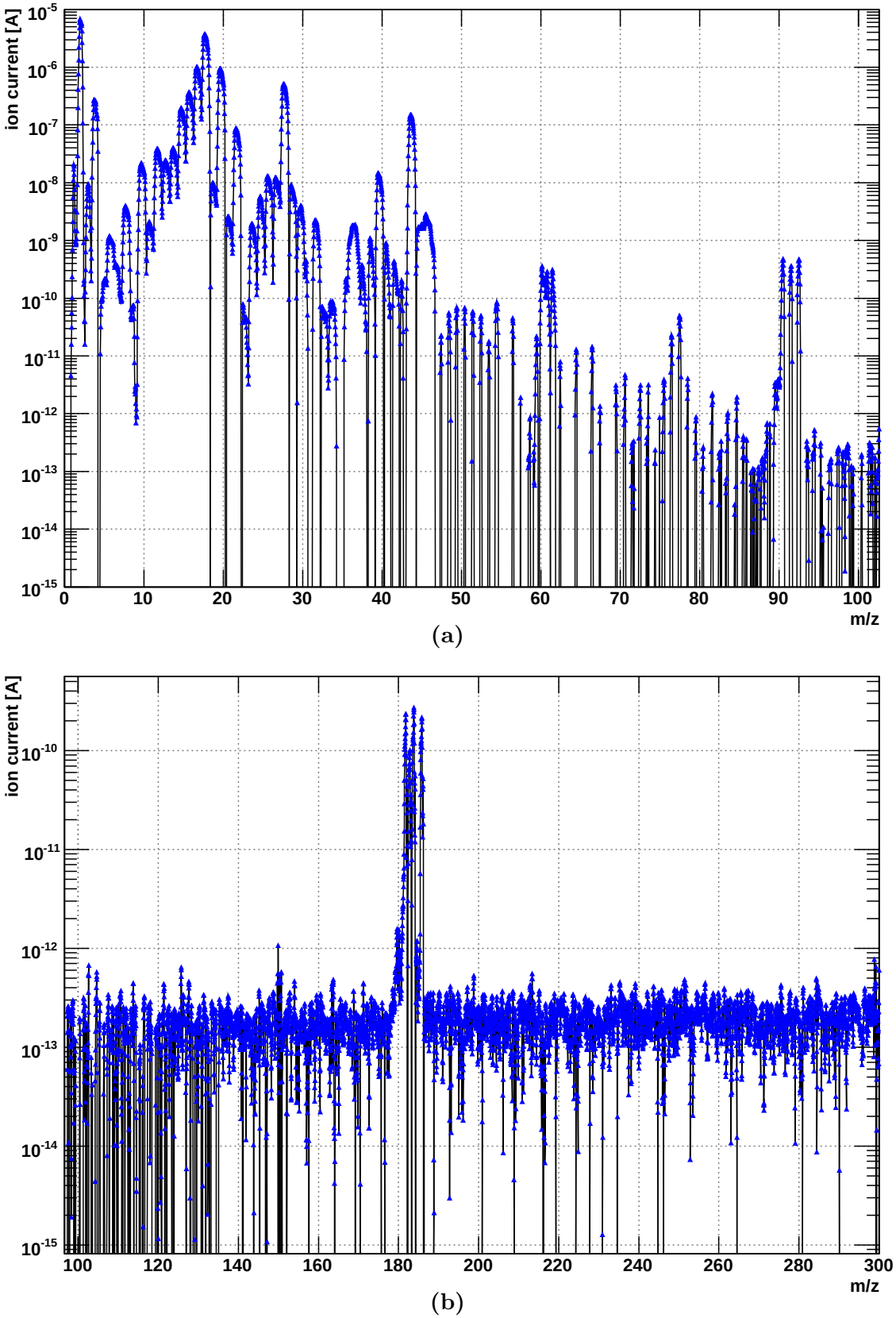

Fig. 21. The 'M2-3 – M2-2' effect showing the difference between the composition of chamber with Rb sample inside the sample holder and the composition of chamber where an empty sample carrier is placed in the holder. Measured with Prisma™ set to default values of OIS parameters, Fil 1 in operation, resolution 40, scan speed $60\,\mathrm{s\,u^{-1}}$ and CEM HV 2 500 V. Part **(a)** shows m/z 0–100 region, part **(b)** m/z 100–300. No Rb signal was found.

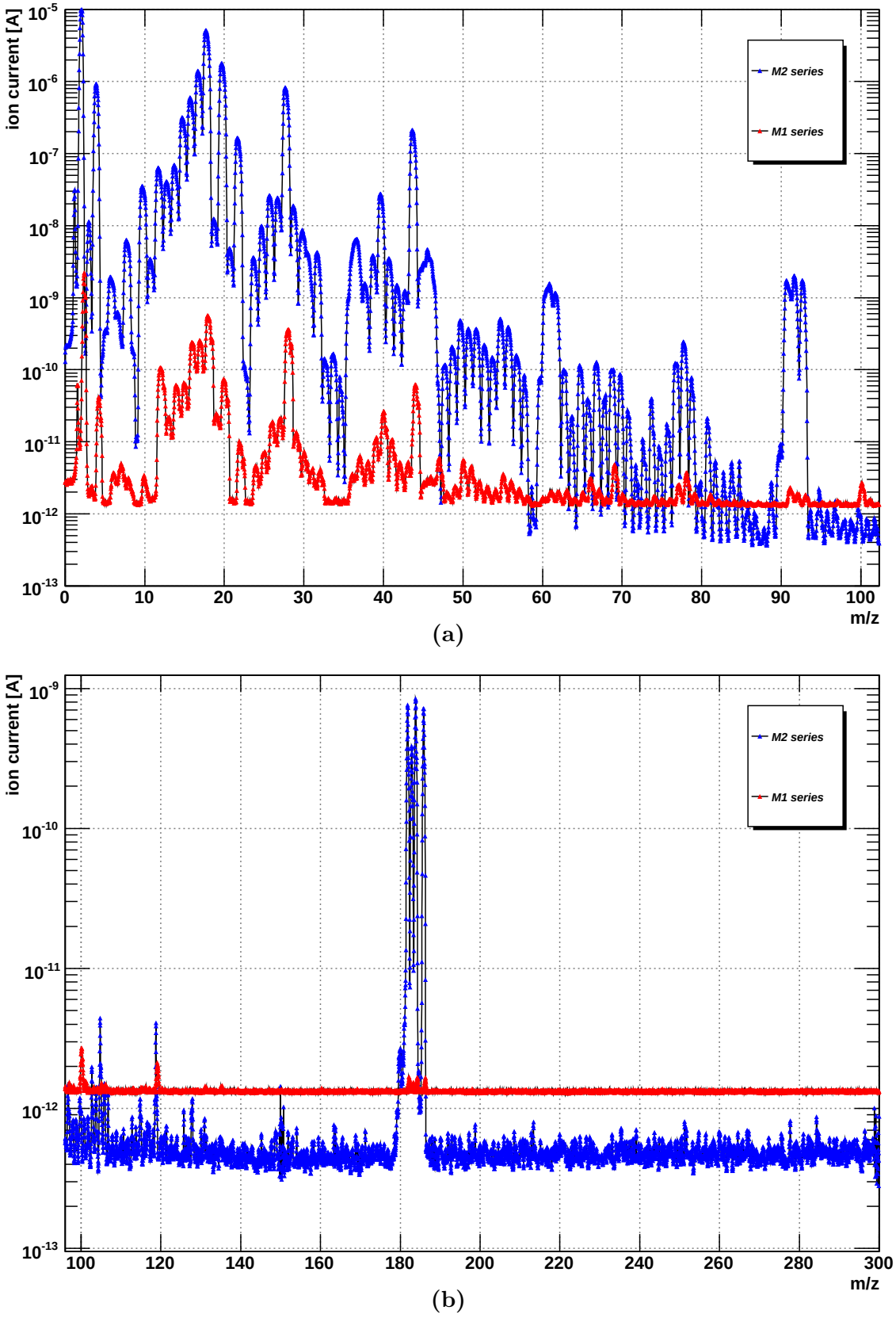

Fig. 22. Comparison of the M1 (red) and M2-3 (blue) typical spectra taken for the Rb sample inside the chamber. The influence of the better M2 operating parameters is seen in lower noise and much higher sensitivity.

4.3.3 Results

In neither M1 nor M2 series any Rb signal has been observed. The limits on the Rb escape which the Prisma™ is capable to reliably detect will be inferred here.

Generally, in the **s**ample containing m_s grams of some compound there are $N_\mathrm{s} = m_\mathrm{s}\, N_A/M_\mathrm{m}$ atoms inside. Designating the fraction of the atoms escaped from the sample as X_out (**out**gassing), the total number of the escaped atoms $N_\mathrm{out} = X_\mathrm{out}\, N_\mathrm{s}$ is obtained. This N_out in turn produces the **p**artial **p**ressure PP in the chamber,

$$PP = \frac{N_\mathrm{out}}{N_\mathrm{tot}}\, P_\mathrm{tot} = \frac{N_\mathrm{out}}{N_\mathrm{out} + N_\mathrm{rg}}\, P_\mathrm{tot}\,, \tag{22}$$

where the **tot**al number of molecules enclosed in the system $N_\mathrm{tot} = N_\mathrm{out} + N_\mathrm{rg}$ equals to the sum of the atoms/molecules resulting from the sample **out**gassing and of the number of molecules making all the remaining **r**esidual **g**ases. Accordingly for the pressures $P_\mathrm{tot} = PP + P_\mathrm{rg}$.

The baseline level of the Prisma™ when properly set is of the order of 10^{-12} A, see Fig. 17, Fig. 19 and Fig. 22. This limit of recognizing any peak in the mass spectrum can be related to the lower limit of the escape of a given compound. Recalling the definition of the RGA sensitivity (Eq. 12) one gets

$$PP = \frac{H^{CEM}(m/z_\mathrm{bp})}{S^{CEM}}\,, \tag{23}$$

where S^{CEM} is the Prisma™ CEM mode sensitivity for the compound and $H^{CEM}(m/z_\mathrm{bp})$ originally designating the height [A] of the compound base peak but now actually having the value of 10^{-12} A representing the noise. Thus from Eq. 23 follows $PP = 10^{-14}$ mbar $\equiv PP_\mathrm{min}$ which has the same meaning as the MDPP value of 4×10^{-14} mbar reported by manufacturer (Tab. 4). Using now Eq. 22—and neglecting N_out against N_rg— the minimum release detectable by the Prisma™ is $N_\mathrm{out} = (PP/P_\mathrm{tot})\, N_\mathrm{tot} \simeq (10^{-14}/5 \times 10^{-9})\, 4 \times 10^{11} \approx 10^6$, where the typical values of total pressure and total number of molecules were taken.

However, the considerations up to now assumed that in the chamber there is a compound which obeys such 'usual' concept of the partial pressure, *i.e.* which outgasses from the sample and is in a thermodynamical equilibrium with the inside of the chamber. Then the partial pressure PP of the substance is the same in every point of the system. In contrast to this, the metallic Rb actually behaves in a quite different manner. The sticking coefficient of Rb on SS chamber walls ('f(Rb@SS)') is close to one [62]. Thus when a Rb atom reaches the SS wall surface it gets easily chemisorbed on and into the SS. Such a sorbed Rb atom then remains in its position till the bakeout of the UHV chamber is performed. It also implies that the Rb is pumped away from the chamber quite difficultly, moreover, the vacuum pump operation has no significant effect upon Rb [62]. Consequently, the sensitivity of the Prisma™ to Rb is considerably decreased as only a small fraction of the desorbed Rb atoms reaches the Prisma™ OIS ionization volume. The rest of the atoms are 'lost' from the analysis as they adsorb on the wall and remain there. So instead of the 'concept of partial pressure' rather some 'concept of flux' would be more appropriate.

The importance of the sticking coefficient was supported by supplementary RGA studies which have been carried out with samples of $ZnCl_2$ and Cd [70]. These substances possess partial pressures P_vap of 10^{-6} mbar (450 K) and 10^{-6} mbar (393 K) [17], respectively. A clear signal on Cd^+ m/z positions really *has been observed* during its heating to $\simeq 100$°C while *no signal* from the $ZnCl_2$ sample has been obtained when heating up to $\simeq 210$°C. This contrast

can be explained by the fact that $f(\text{Cd@SS}) \rightarrow 0$ while $f(\text{ZnCl}_2\text{@SS}) \rightarrow 1$ like in the case of Rb [13, 62].

The M2 data are more reliable as the optimum Prisma™ settings were used throughout this series of measurements, however, several points can be disputed:

- Rb has a considerably high P_{vap} so the consequent evaporation from the surface is possible and the atom gets sorbed on its new position where it reaches the SS wall again. This possibility of the 'Rb atoms re-evaporation' from the SS walls means that actually a somewhat higher fraction can reach the OIS ionizing region since the re-evaporated Rb atoms which have not been initially desorbed from the sample surface in the line-of-sight direction to the Prisma™ OIS can reach it as well. For the sake of simplicity no re-evaporation is assumed.
- As stated above (Sect. 3.2) rubidium is never in the pure metallic form in the UHV system, rather in some Rb compound having considerably lower P_{vap} and thus the N_{out} value.
- The sticking coefficient 'f(RbXY@SS)' factor can vary significantly due to distinct nature of pure rubidium and Rb compounds.
- The contamination by the residual gases (during the preparation and storage on air) creating additional monolayers on the samples probably plays a role and complicates this problem.

5 NPI Řež/Prague: gamma spectroscopy

In order to investigate the ^{83}Rb release from ^{83}Rb/^{83m}Kr solid sources being developed at NPI Řež/Prague for the KATRIN experiment by vacuum evaporation (see Sect. 2.2 and Sect. 3.3), gamma spectroscopy was used. Altogether four sources designated as S4, S7, S8 and S9 have been tested, differing in the amount of the initial activity at the moment of production, in quality of the substance and in the sample 'history'.

The basis of the investigation lies in a precise determination of gamma ray peak area. The whole analysis will be carried out in the units of counts per seconds and the release will be stated in the units of percents—any conversion of peak areas to activities through efficiency calibration and gamma transition intensities would introduce additional errors.

Firstly, the experimental setup will be briefly described, then the methods used for the determination of the peak areas will be introduced and discussed. At last, the complete analysis of the peak areas obtained from ^{83}Rb spectra will be shown and the ^{83}Rb release from the sources S4–S9 will be deduced quantitatively.

5.1 Experimental setup

The following gamma-spectrometer system was used for measuring the ^{83}Rb spectra:

- n-type HPGe detector EGCN 20 Schlumberger with vertical cryostat:
  - active volume of 97.5 cm^3 and surface area of 21 cm^2 (diameter 51.8 mm, length 49.4 mm), end cap distance of 5 mm,
  - relative efficiency of 22.3 % at 1 332 keV (relative to that of a standard 3×3 inch NaI(Tl)),
  - resolution (FWHM) of 850 eV at 122 keV and 1.80 keV at 1 332 keV,
  - FWTM/FWHM and FWFM/FWHM ratios of 1.86 : 1 and 2.42 : 1 (1 332 keV), respectively,
  - peak-to-Compton ratio of 53 : 1 (1 332 keV),
  - working high voltage of −4 000 V,
- **h**igh **v**oltage **s**upply HVS ND 360,
- **s**pectroscopy **am**plifier SAM ND 591,
- **a**nalog-to-**d**igital **c**onverter ADC ND 581 set to 8192 channel resolution,
- **l**oss-**f**ree **c**ounting LFC module ND599 for dead time correction of the system,
- PC with AccuSpec card.

The detector was situated in a shielding box made of lead bricks with the wall thickness of 5 cm.

5.2 Peak area determination methods

5.2.1 Functional description of spectral gamma line

Initially, a many parameter function for the fit of the test spectra was attempted using a least-square fitting routine in the ROOT framework [71]. The weights for the least-square fitting were taken in accordance with the Poisson character of the gamma ray emission, *i.e.* as the inverse values of the number of counts. Single 662 keV peak of ^{137}Cs was very well fitted with the combination of the functions commonly used for the description of gamma ray **f**ull-**e**nergy **p**eaks (FEPs) observed with semiconductor detectors. The following functions were used in the fit [72, 73, 74, 75]:

- For an ideal detector a monoenergetic radiation with a negligible natural width gives rise a sharp peak which is broadened by the statistical and electronic noise into a symmetric distribution which can be best approximated by a Gaussian curve,

$$G(x) = a_0 \exp - \left(\frac{x - a_1}{\sqrt{2}\, a_2} \right)^2 , \tag{24}$$

  where the free parameters a_0, a_1 and a_2 represent the amplitude, centroid and width of the FEP, respectively. In application of the formula the variable x represents the energy or the channel number. The **f**ull **w**idth at **h**alf **m**aximum (FWHM) is then given by the relation $\mathrm{FWHM} = 2\sqrt{2 \ln 2}\, a_2$.

- The effect of incomplete charge collection in the detector and pile-up in the electronic chain can remove pulses from the central Gaussian part, producing an exponentially decreasing distribution, a **l**ow energy **t**ail, below the FEP:

$$LT_1(x) = a_3 \exp \left(\frac{x - a_4}{a_5} \right) \operatorname{erfc} \left(\frac{x - a_4}{a_6} + \frac{a_6}{2\, a_5} \right) , \tag{25}$$

  where the parameters a_3, a_4, a_5, a_6 stand for the amplitude, centroid, slope and width of the tail, respectively, and erfc is the complementary error function. The amplitude of this component usually does not exceed 1–10 % that of the central Gaussian.

- For strong peaks one can observe a much longer exponential tail on the low energy side of the FEP due to defects on the detector surface,

$$LT_2(x) = a_7 \exp \left(\frac{x - a_8}{a_9} \right) \operatorname{erfc} \left(\frac{x - a_8}{a_{10}} + \frac{a_{10}}{2\, a_9} \right) , \tag{26}$$

  where the parameters a_7–a_{10} retain their meanings from Eq. 25. This is usually reduced two or three orders of magnitude in amplitude relative to that of the central Gaussian.

- To account for the distortion of the ideal Gaussian detector response on the high energy side of the FEP, a **h**igh energy exponential **t**ail is sometimes used as well:

$$HT(x) = a_{11} \exp \left(\frac{a_{12} - x}{a_{13}} \right) \operatorname{erfc} \left(\frac{a_{12} - x}{a_{14}} + \frac{a_{14}}{2\, a_{13}} \right) . \tag{27}$$

  This term is similar in form to the low energy tailing terms, except reflected about the peak centroid.

- For the FEP one can observe a significant step or ledge below the peak which is produced mainly by small-angle Compton scattering of the radiation from the surrounding materials into the detector. Neglecting the broadening due to the detector resolution, this distribution can be considered flat and extending to the centroid of the peak, however, the discontinuity of the **s**tep is broadened in the same manner as the monoenergetic gamma ray line, *i.e.* the step function is convoluted with a Gaussian, resulting in

$$S(x) = a_{15}\,\mathrm{erfc}\left(\frac{x - a_{16}}{\sqrt{2}\,a_{17}}\right), \tag{28}$$

  where the parameters a_{15}, a_{16} and a_{17} characterize the amplitude, centroid and width of the step, respectively.

- Finally, the **b**ackground term for the continuum within a small range containing the peak is usually sufficiently well represented by a first order polynomial,

$$B(x) = a_{18}\,x + a_{19}\,. \tag{29}$$

The total function describing the FEP is

$$T(x) = G(x) + LT_1(x) + LT_2(x) + HT(x) + S(x) + B(x)\,, \tag{30}$$

having thus altogether 20 free parameters a_0–a_{19} per one FEP. This expression is very non-linear and to circumvent this fact one has to constrain or set limits on some of the parameters. The parameters characterizing the non-Gaussian peak shape, *i.e.* a_3–a_{17}, are usually slowly varying functions of the photon energy and it is a common practice to determine for these functions approximate analytical expressions from fits of spectra containing strong, well-resolved peaks at suitable energies. Such a peak shape calibration was not carried out with our fitting routine, only the following constraints [72] of the selected parameters were implemented: a_4, a_8, a_{12} and a_{16} were fixed equal to the FEP centroid a_1 or shifted by a fixed number of channels to an appropriate side of the peak (or just constrained in a reasonable range), a_6 a_{10}, a_{14} and a_{17} were fixed equal to peak width a_2 and the amplitudes of the tails and the step a_3, a_7, a_{11} and a_{15} were set proportional to the Gaussian amplitude a_0. Eventually there are eight free parameters: a_0–a_2 of the Gaussian, slopes a_5, a_9 and a_{13} of the three tails and a_{18} and a_{19} representing the background.

From the fitted parameters a_0, a_2 the FEP area, defined as the integral of the Gaussian function, can be calculated as

$$A_{\mathrm{fit}} = \sqrt{2\,\pi}\,a_0\,a_2\,. \tag{31}$$

Its variance then follows from an error propagation law as

$$\sigma^2(A_{\mathrm{fit}}) = 2\,\pi\,\left(a_2^2\,\sigma^2(a_0) + a_0^2\,\sigma^2(a_2) + 2\,a_0\,a_2\,\sigma(a_0\,a_2)\right)\,, \tag{32}$$

where $\sigma^2(a_0)$, $\sigma^2(a_2)$ and $\sigma(a_0\,a_2)$ are the variances of the Gaussian amplitude and width and their covariance, respectively.

A typical result of the fitting routine is shown in Fig. 23 together with the residuals normalized to statistical errors taken as square root of counts. Some quantitative considerations of the results obtained with this routine are postponed to Sect. 5.2.4 where they are compared with the results of summation methods.

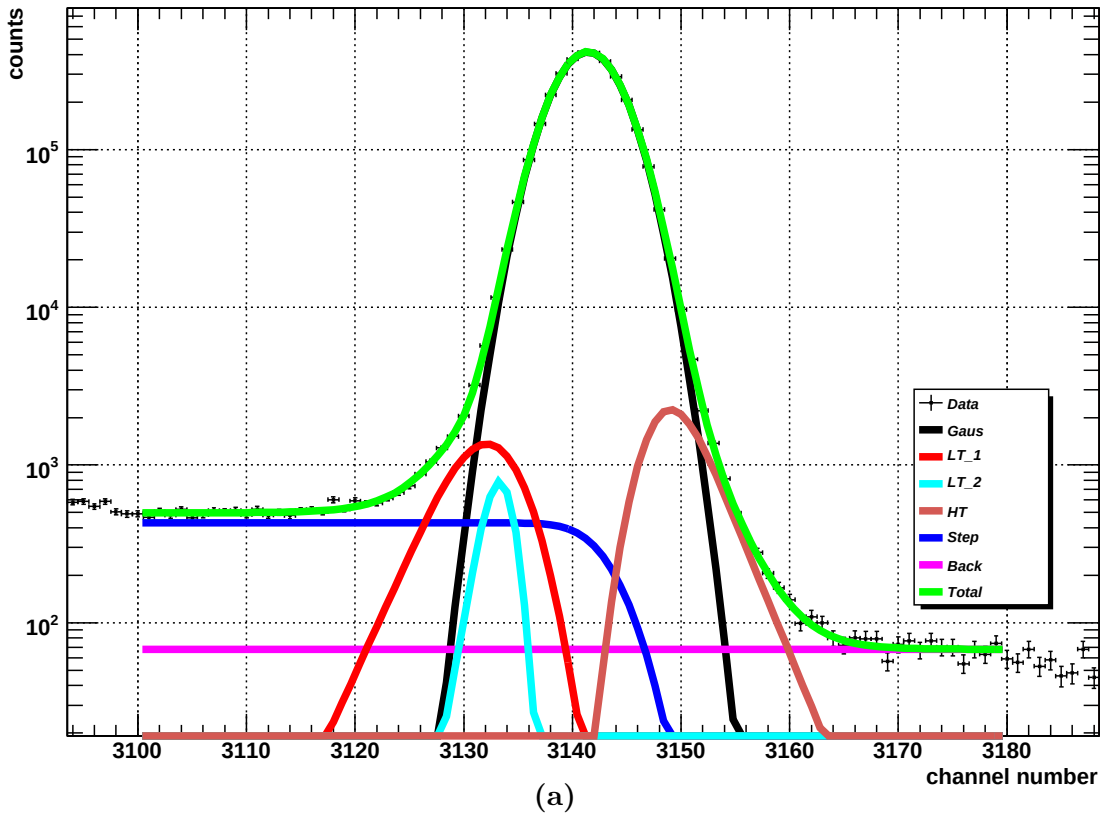

(a)

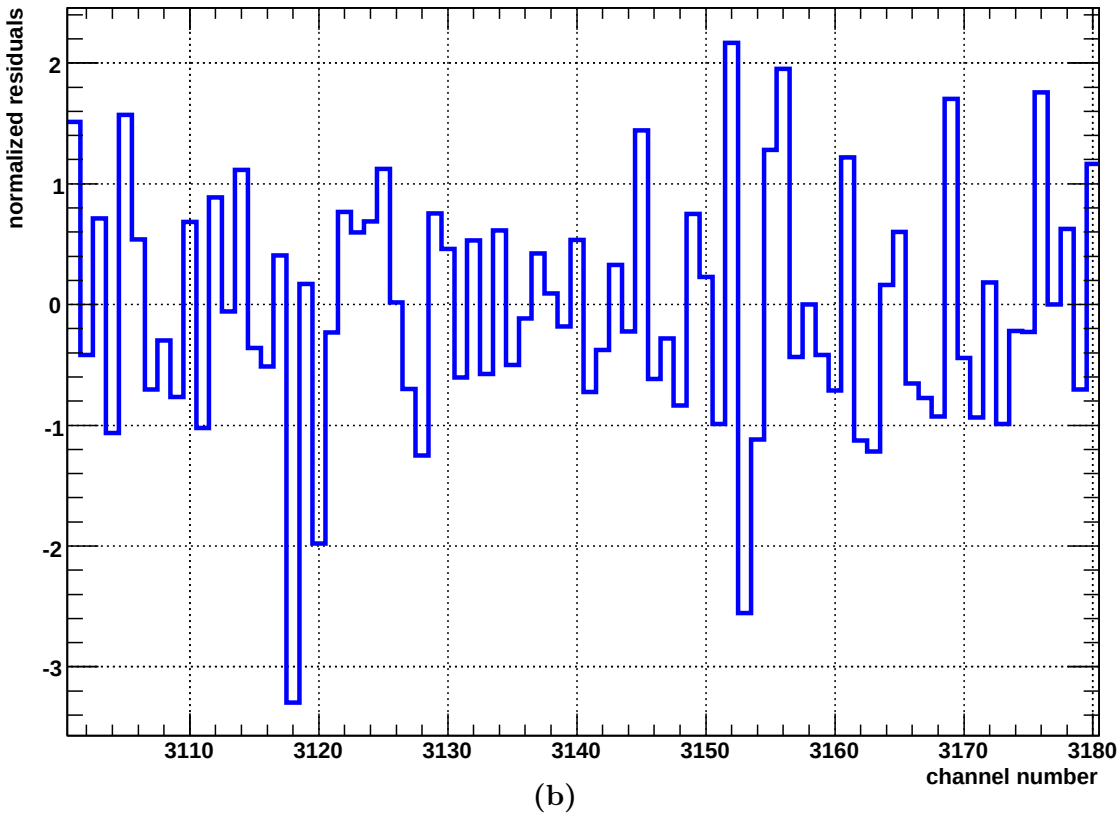

(b)

Fig. 23. Example of a fit of a single 662 keV ^{137}Cs peak with high statistics, $\chi^2_{\text{norm}} \simeq 1.2$. **(a)** For the description of individual components of the total fitted function see text. The deviation from the FEP ideal Gaussian shape (black line) due to low and high energy tails is clearly seen. **(b)** Plot of normalized residuals ('(fit − data)/error of data') indicates that a reasonable fit was achieved.

5.2.2 Common summation methods

Besides the methods which fit the function of known form to the data and then integrate the resulting functions to determine the peak area there is also a second group of methods which treats the spectral data more directly. There is a number of summation methods [76, 77, 78, 79], all differing more or less in the definition of the area, summing the counts in all the channels of the peak (the tails in- or excluded) or taking into account only several channels about the centermost one, approximating the background by averaging the channels (one or several) immediately on the left and right of the peak region or fitting polynomials of the second or third order to the channels surrounding the peak *etc.*

The basic method from which a lot of others is derived is the **t**otal **p**eak **a**rea (TPA) method firstly calculate the total sum ('peak + background')

$$A_{\mathrm{tot}} = \sum_{i=S_l}^{i=S_r} N_i \,, \tag{33}$$

N_i, S_l and S_r being the number of counts in ith-channel and the **l**eft and **r**ight channel limit of **s**ummation, respectively. An average of the counts in n_B channels immediately on the left and right (approximation of the background) is then subtracted, thus getting the net area

$$A_{\mathrm{TPA}} = A_{\mathrm{tot}} - \frac{(S_r - S_l + 1)}{2\,n_B} \sum_{i=1}^{i=n_B} (N_{S_l - i} + N_{S_r + i}) \tag{34}$$

and its variance as

$$\sigma^2(A_{\mathrm{TPA}}) = A_{\mathrm{tot}} + \frac{(S_r - S_l + 1)^2}{4\,n_B^2} \sum_{i=1}^{i=n_B} (N_{S_l - i} + N_{S_r + i}) \,. \tag{35}$$

A somewhat modified TPA method was developed in the computer programme AREA [80]. Here besides the range of **s**ummation, $\langle S_l, S_r \rangle$, two ranges $\langle L_l, L_r \rangle$ and $\langle R_l, R_r \rangle$ of data are chosen on the **l**eft and **r**ight side of the peak, respectively, serving for averaging the background on each side of the peak separately. Thus one gets two points $\left[x_l, \overline{L}\right]$ and $\left[x_r, \overline{R}\right]$, where

$$x_l = \frac{(L_l + L_r)}{2} \,, \quad x_r = \frac{(R_l + R_r)}{2} \,, \quad \overline{L} = \frac{\sum_{i=L_l}^{i=L_r} N_i}{L_r - L_l + 1} \,, \quad \overline{R} = \frac{\sum_{i=R_l}^{i=R_r} N_i}{R_r - R_l + 1} \,, \tag{36}$$

with variances being

$$\sigma^2(x_l) = \sigma^2(x_r) \equiv 0 \,, \quad \sigma^2\big(\overline{L}\big) = \frac{\sum_{i=L_l}^{i=L_r} N_i}{(L_r - L_l + 1)^2} \,, \quad \sigma^2\big(\overline{R}\big) = \frac{\sum_{i=R_l}^{i=R_r} N_i}{(R_r - R_l + 1)^2} \,, \tag{37}$$

from which an expression of the line for the description of the background under the peak is obtained as

$$B(x) = k\,x + q \,, \quad k = \frac{\overline{R} - \overline{L}}{x_r - x_l} \,, \quad q = \frac{x_r\,\overline{L} - x_l\,\overline{R}}{x_r - x_l} \,, \tag{38}$$

where k and q have variances and covariance as

$$\sigma^2(k) = \frac{\sigma^2(\overline{L}) + \sigma^2(\overline{R})}{(x_l - x_r)^2}\,,\;\; \sigma^2(q) = \frac{x_r^2\,\sigma^2(\overline{L}) + x_l^2\,\sigma^2(\overline{R})}{(x_l - x_r)^2}\,,\;\; \sigma(kq) = -\frac{x_r\,\sigma^2(\overline{L}) + x_l\,\sigma^2(\overline{R})}{(x_l - x_r)^2}\,, \tag{39}$$

so the variance of the background function at a given x is

$$\sigma^2(B(x)) = x^2\,\sigma^2(k) + \sigma^2(q) + 2\,x\,\sigma(kq)\,. \tag{40}$$

Finally the net area A_{AR} (**AR**EA) is calculated as

$$A_{\mathrm{AR}} = A_{\mathrm{tot}} - \sum_{i=S_l}^{i=S_r} B(i) \tag{41}$$

and its variance as

$$\sigma^2(A_{\mathrm{AR}}) = A_{\mathrm{tot}} + \sum_{i=S_l}^{i=S_r} \sigma^2\left(B(i)\right)\,. \tag{42}$$

The 'background' ranges $\langle L_l, L_r\rangle$ and $\langle R_l, R_r\rangle$ can be chosen as immediately surrounding the summation range $\langle S_l, S_r\rangle$, intersecting it or can be separated from it by arbitrary number of channels (*e.g.* in the presence of some adjacent peak). For a concrete situation all the ranges have to be chosen appropriately after a visual inspection of the spectrum.

5.2.3 Summation after background subtraction

The summation methods explained above do not take into account the step of the background (approximated by Eq. 28) usually observed on the low energy side of the spectral peak. This led to the development of a computer routine SBS (**s**ummation after **b**ackground **s**ubtraction) written in the ROOT framework. It is based on the assumption that enough far away from the single FEP there is only such a step, *i.e.* a difference between constant background levels on the low and high energy side of the FEP. This step is assumed to be proportional to the area of the peak. However, this simplification is valid only partly if the nonconstant Compton continuum from other peaks is present.

This method of the peak area determination can be summarized as follows. Similarly to 'AR' method the ranges $\langle S_l, S_r\rangle$, $\langle L_l, L_r\rangle$ and $\langle R_l, R_r\rangle$ have to be defined before the calculation, in addition, one more range $\langle B_l, B_r\rangle$ defining the **b**ackground to be fitted has to be set. Thus firstly the fit of background is carried out,

$$B(x) = k\,x + q\,,\;\; x \in \langle B_l, B_r\rangle\,, \tag{43}$$

from which the values k, q, $\sigma^2(k)$, $\sigma^2(q)$ and $\sigma(kq)$ are obtained. Then the channel-by-channel subtraction proceeds,

$$N_i^{\mathrm{new}} = N_i - (k\,i + q)\;,\;\; i = L_l, \ldots, R_r\,, \tag{44}$$

where the term in brackets represents the counts of the background in the ith channel. The error of each new number of counts has to be increased according to

$$\sigma^2(N_i^{\mathrm{new}}) = N_i + i^2\,\sigma_k^2 + \sigma_q^2 + 2\,i\,\sigma_{kq}\,. \tag{45}$$

Further, while the whole peak region is excluded, the background on both sides of the region is fitted with the function

$$SB(x) = a_0 + a_1 \operatorname{erfc}\left(\frac{x - a_2}{\sqrt{2}\, a_3}\right) , \quad x \in \langle L_l, L_r\rangle \cup \langle R_l, R_r\rangle , \tag{46}$$

where the term a_0 represents the constant, as the slope of the background was already 'subtracted' from the data, and the terms a_1, a_2 and a_3 retain their meaning from expression Eq. 28 of the step function. The parameters a_2 and a_3 were kept fixed equal to the values of peak centroid and width, respectively, which were obtained from a previous fit of Gaussian (Eq. 24) to the central part of the peak. This approach gives reasonable values for the parameters a_2 and a_3. Thus the only parameters to be fitted in expression Eq. 46 were a_0 and a_1.

Similarly to Eq. 33 the total sum

$$A_{\mathrm{tot}}^{\mathrm{new}} = \sum_{i=S_l}^{i=S_r} N_i^{\mathrm{new}} \tag{47}$$

of the new data is calculated and finally the net area is obtained as

$$A_{\mathrm{SBS}} = A_{\mathrm{tot}}^{\mathrm{new}} - a_0 \, (S_r - S_l + 1) \, . \tag{48}$$

The variance of the net area

$$\sigma^2 \left(A_{\mathrm{SBS}}\right) = \sum_{i=S_l}^{i=S_r} \sigma^2 \left(N_i^{\mathrm{new}}\right) + \left(S_r - S_l + 1\right)^2 \, \sigma_{a_0}^2 \, , \tag{49}$$

takes the errors of new data correctly into account.

The SBS method is demonstrated in Fig. 24 for the case of 662 keV ^{137}Cs FEP. The detailed discussion of the results is again postponed to Sect. 5.2.4.

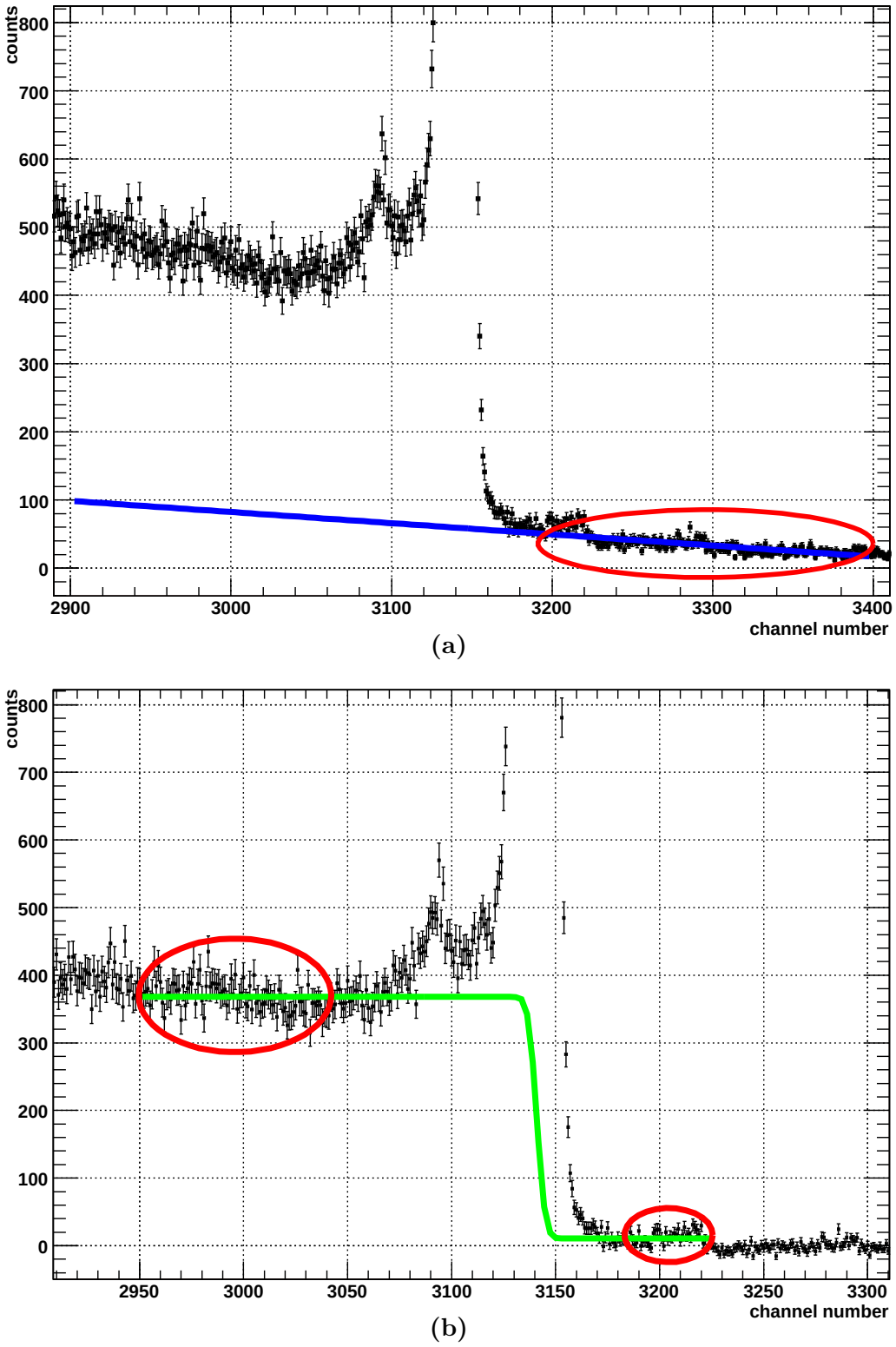

Fig. 24. Principle of the SBS method demonstrated on 662 keV ^{137}Cs gamma line (clipped in the figure). The channel 3142 represents the peak centroid. At channel 3090 the KX(Ge) escape peak is discernible. **(a)** The background on the high energy side of the peak is fitted with a linear function. The ellipse indicates the range of data used for this background fit, all the other points are excluded for this moment. The blue line shows the background, underlying the peak, to be subtracted. **(b)** After the background subtraction the combination of a constant and step functions is fitted to the background on both sides (the ranges again indicated by ellipses) of the peak simultaneously while all the points from the peak are not taken into account.

5.2.4 Comparison of methods

The comparison of all the methods for the peak area determination, fit with functional description and three summation methods TPA, AR and SBS, was carried out with two series of ^{137}Cs spectra. These spectra were obtained with the same spectrometer system and the same operating parameters like the ^{83}Rb spectra measured for the ^{83}Rb release investigation.

The first series—TS1—consists of twenty 'identical' ^{137}Cs spectra (exposition of 2 hours live time, dead time about 5.5 %) which was acquired via an automatic 20 times execution of a stream of commands for the measurement and storage of the spectrum. The relevant AccuSpec system mode is called AUTOSEQUENCE. The ^{137}Cs source was not moved nor touched in between any of these measurements.

The second series—TS2—represents eight spectra of ^{137}Cs source measured in the presence of various ^{60}Co activities. The ^{137}Cs source was not moved nor touched and the various 'additional' detector loads were realized by a ^{60}Co source placed at different positions in the shielding box. Here the exposition was 5 hours live time and the ^{60}Co source was positioned in such a way that the dead times of approximately 5 %, 10 %, 15 %, 20 %, 25 % and 30 % were obtained. At the beginning of the series and then between '25 %' and '30 %' measurements the ^{60}Co source was absent thus two '3 %' spectra were obtained. The effect of different detector loads in vicinity of 662 keV gamma line is seen in Fig. 25.

TS1 was intended to test the inherent consistency of the peak-area methods. Here all the methods were set to use the same region of spectral data, the fit routine used the same region for fit as the TPA, AR and SBS methods for the total summation (channels 3100–3180). In addition, the TPA method was set to use $n_B = 20$ channels immediately surrounding the peak on both sides, the AR and SBS methods were set to use the same $\langle L_l, L_r\rangle = \langle 2950, 3040\rangle$ and $\langle R_l, R_r\rangle = \langle 3185, 3226\rangle$ background regions. Moreover, the SBS method used $\langle B_l, B_r\rangle = \langle 3190, 3400\rangle$ range for the fit of the high energy side background. The dependence of areas on spectrum order number for all methods is presented in Fig. 26.

From the plot of the normalized residuals (owing to the weighted mean) of the TPA, AR and SBS methods it was found that within the interval $\langle -1, +1\rangle$ (68 % confidence interval) there are 70 %, 85 % and 85 % of all 20 cases for the TPA, AR and SBS methods, respectively, indicating rather smaller scatter of the data. In addition, the ratios $\overline{\sigma}^{\mathrm{w}}_{\mathrm{sc}}/\overline{\sigma}^{\mathrm{w}}_{\mathrm{err}}$ of the errors of the weighted means due to **sc**atter and **err**ors of the individual summation methods, shown in the last column of Tab. 8, indicate that the errors of individual areas obtained by the summation methods are realistic [73], more precisely they are slightly larger. It can be shown that in the case of the data obeying normal distribution the value of $(\overline{\sigma}^{\mathrm{w}}_{\mathrm{sc}}/\overline{\sigma}^{\mathrm{w}}_{\mathrm{err}})^2$, representing actually the ratio of 'external' and 'internal' variances of the weighted mean of the series, is equal to the χ^2_{norm} value of a fit of constant to the series of n data [73]. Indeed, the χ^2_{norm} values of such fits to the TS1 results (represented by the lines in Fig. 26) were equal to the squares of the values in the last column of Tab. 8.

The χ^2_{norm} values of the fits when the fitting routine was used were in all cases in range 0.9–1.9 indicating good fits, however, the resulting peak areas were inconsistent and their errors were about twice the errors of summation methods. Such a poor performance is surely caused by the absence of a proper peak shape calibration of the fitting routine since in the existing conditions (possible improper constraints of the parameters) the variance of the Gaussian amplitude obtained from the fit varied significantly due to amplitudes of the tails and the step. This naturally disqualifies this method for its use for ^{83}Rb release investigation. From now on only the summation methods are considered.

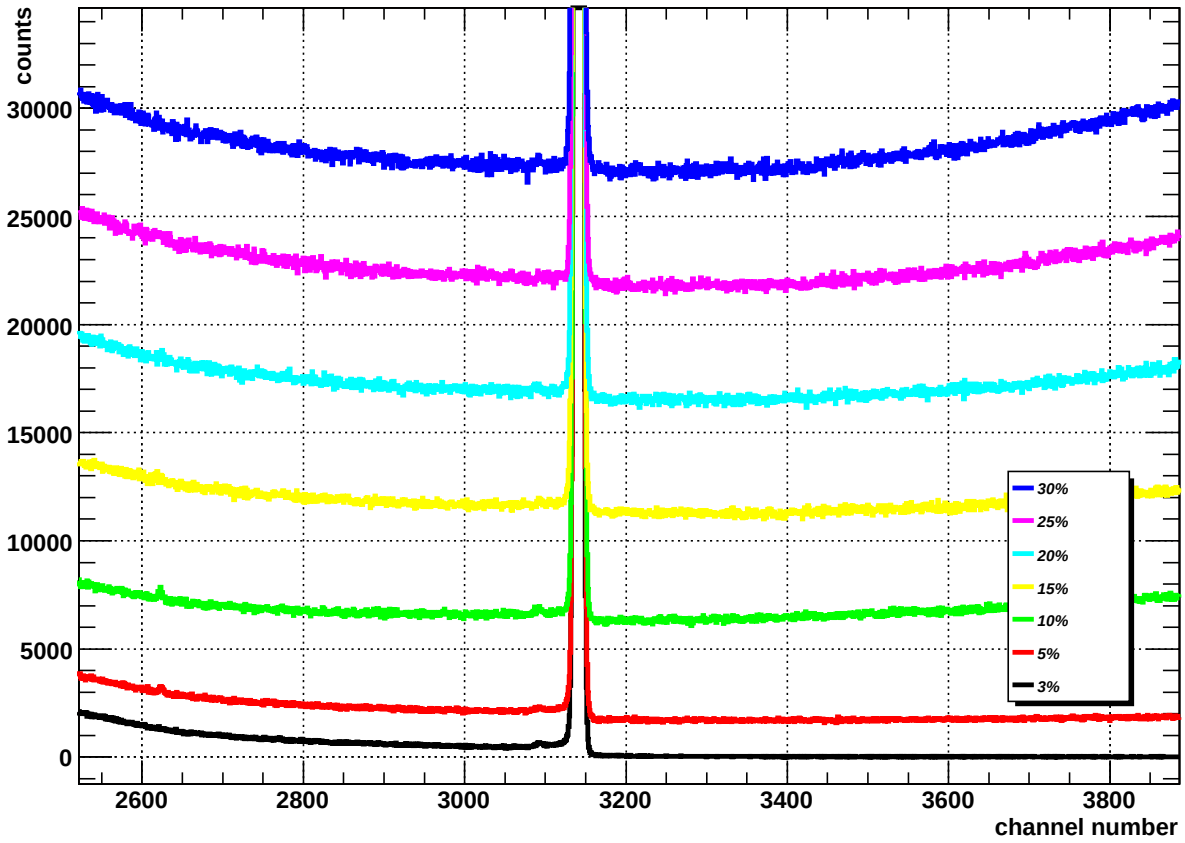

Fig. 25. Part of ^{137}Cs+^{60}Co spectra measured in TS2 series. All the spectra are placed on the same zero level, approximative position of the 662 keV ^{137}Cs peak is channel 3142. For clarity only one '3 %' spectrum is shown on the bottom and the large peak counts are clipped. The step produced by the FEP is clearly visible in the '3 %' spectrum and is present in the other spectra as well, however, there it is masked by high levels of background.

Tab. 8. TS1 (20 spectra) results of the fit routine and TPA, AR and SBS methods.

	$\overline{X}$ [10^3]	$\overline{\sigma}$ [10^3]	σ_1 [10^3]	[‰]	$\overline{X}^{\mathrm{w}}$ [10^3]	$\overline{\sigma}^{\mathrm{w}}_{\mathrm{err}}$ [10^3]	$\overline{\sigma}^{\mathrm{w}}_{\mathrm{sc}}$ [10^3]	$\overline{\sigma}^{\mathrm{w}}_{\mathrm{sc}}/\overline{\sigma}^{\mathrm{w}}_{\mathrm{err}}$
A_{tot}	3 224.54	0.37	1.63	0.51	3 224.54	0.40	0.37	0.91
A_{fit}	3 165.86	0.91	4.05	1.28	3 166.40	0.55	0.89	1.63
A_{TPA}	3 200.48	0.38	1.71	0.53	3 200.48	0.40	0.38	0.94
A_{AR}	3 209.66	0.37	1.65	0.52	3 209.66	0.40	0.37	0.92
$A^{\mathrm{new}}_{\mathrm{tot}}$	3 219.59	0.37	1.66	0.52	3 219.59	0.40	0.37	0.92
A_{SBS}	3 218.79	0.37	1.67	0.52	3 218.79	0.40	0.37	0.93

The columns indicate the values of the unweighted mean $\overline{X}$ of 20 values, its error $\overline{\sigma}$, typical error σ_1 of one measurement in the sequence, its relative error in ‰, weighted mean $\overline{X}^{\mathrm{w}}$, its errors $\overline{\sigma}^{\mathrm{w}}_{\mathrm{err}}$ and $\overline{\sigma}^{\mathrm{w}}_{\mathrm{sc}}$ due to **err**ors and **sc**atter, respectively and their ratio. The values of A_{tot} and $A^{\mathrm{new}}_{\mathrm{tot}}$, actually representing the statistical limits of possible accuracy, are shown for illustration only.

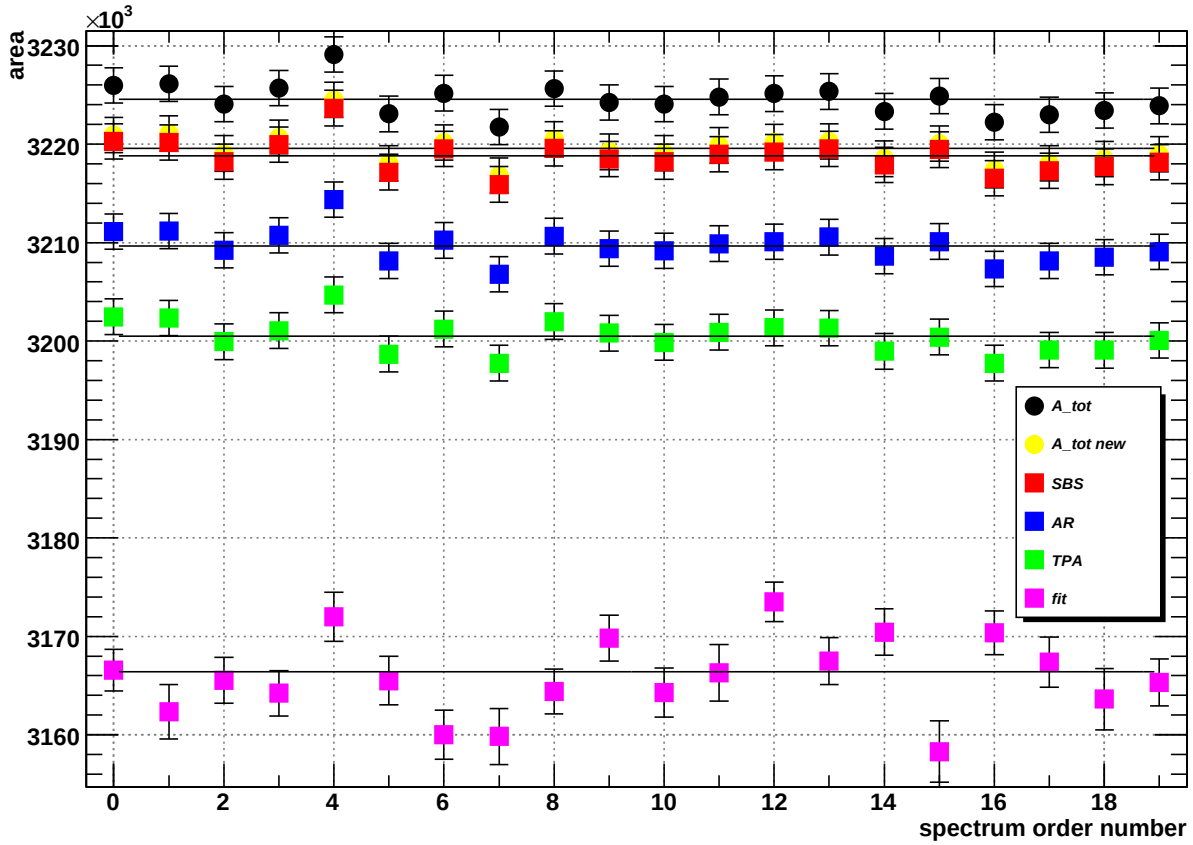

Fig. 26. The values of areas obtained from TS1 series with the help of fitting routine, TPA, AR and SBS methods. For the details of parameters set in individual methods see text. The values of A_{tot} and $A_{\mathrm{tot}}^{\mathrm{new}}$ are shown for illustration only.

TS2 was actually meant as a check of the detector system ability to correct for losses of the FEPs areas due to high count rates (high dead times) which were expected for the ^{83}Rb spectra measurements. In the absence of the ^{60}Co source the count rate in a fixed region containing the ^{137}Cs peak was measured by AccuSpec system [7] as 197 pulses per second. This value of the total area count rate rose to 261 pulses per second for the case of '30 %' spectrum, while the net area count rate was determined as the same as for '3 %' spectrum. Thus the ^{137}Cs 662 keV peak was 'lying' on various levels of background (Fig. 25). As the measure of the detector load the dead time value was taken. If the LFC module (Sect. 5.1) would work correctly, the ^{137}Cs peak areas measured in TS2 should be 'identical' thanks to a proper dead time correction. Without such correction the values of FEP areas would decrease with increasing dead time.

However, besides the loss of the FEP counts due to the dead time, the loss due to the effects of pile-up (chance coincidence) occurs [73, 81], which complicates the situation. With increasing count rate the probability of various pile-ups ('line + line', 'line + Compton continuum' and 'Compton cont. + Compton cont.'; actually photons of any energy undergo the pile-up processes but the most pronounced are the photons belonging to FEPs) increases as well. As no additional

[7] A modification of the TPA method is utilized in used AccuSpec system.

Tab. 9. TS2 results of the summation methods.

Dead T.	TPA			AR			SBS		
[%]	$A\,[10^3]$	$\sigma(A)$	[‰]	$A\,[10^3]$	$\sigma(A)$	[‰]	$A\,[10^3]$	$\sigma(A)$	[‰]
3.05	3 550.6	1.9	0.5	3 550.4	1.9	0.5	3 563.6	1.9	0.5
3.06	3 554.3	1.9	0.5	3 554.3	1.9	0.5	3 567.0	1.9	0.5
5.01	3 557.4	2.0	0.6	3 557.6	1.9	0.5	3 571.1	2.1	0.6
10.02	3 558.9	2.3	0.6	3 559.2	2.0	0.6	3 570.8	2.5	0.7
15.43	3 560.6	2.5	0.7	3 557.7	2.1	0.6	3 568.8	2.8	0.8
20.31	3 563.5	2.7	0.8	3 561.1	2.1	0.6	3 571.7	3.2	0.9
25.35	3 572.9	2.9	0.8	3 571.5	2.2	0.6	3 575.5	3.5	1.0
30.09	3 568.3	3.1	0.9	3 568.2	2.3	0.6	3 573.3	3.8	1.1
k	1.9×10^{-4}			1.7×10^{-4}			8.5×10^{-5}		
$\sigma(k)$	2.6×10^{-5}			2.1×10^{-5}			2.9×10^{-5}		
q	1.00027			1.00034			1.00067		
$\sigma(q)$	3.6×10^{-4}			3.4×10^{-4}			3.7×10^{-4}		
$\sigma(kq)$	-7×10^{-9}			-6×10^{-9}			-8×10^{-9}		

In the upper part the values of areas and their errors (firstly stated as absolute in 10^3 and then as relative errors per mil) shown in the dependence on the increasing dead time. In the lower part the slope k, absolute term q and their errors $\sigma(k)$, $\sigma(q)$ and covariance $\sigma(kq)$ of the linear fits to the normalized data ('$A(3.05\,\%) \equiv 1$') are shown.

measurements were made, these two effects of dead time and pile-up were indistinguishable.

The ^{137}Cs peaks were analyzed with the help of all the three summation methods. The trend 'dead time–^{137}Cs FEP area' was meant to be then taken into account as a dead time correction 'dead time–any peak area' during the calculation of the ^{83}Rb release from ^{83}Rb peaks areas obtained from those methods. As will be seen later the situation with the positions of the three ^{83}Rb peaks is a bit troublesome as the peaks are well-resolved but adjacent so that only several channels in the 'valleys' between them could be used for the background approximation. Thus the same conditions were set for the evaluation of the TS2 areas: summation region $\langle S_l, S_r\rangle = \langle 3114, 3166\rangle$, $n_B = 8$, left and right background regions $\langle L_l, L_r\rangle = \langle 3105, 3111\rangle$ and $\langle R_l, R_r\rangle = \langle 3170, 3178\rangle$, background fit region for SBS $\langle B_l, B_r\rangle = \langle 3190, 3300\rangle$.

The TS2 results are summarized in Tab. 9. Each set of data was further normalized to the FEP area from the 3.05 % dead time spectrum and fitted with linear function in order to approximate the 'dead time–^{137}Cs FEP area' trend. The results are included in Tab. 9 and plotted in Fig. 27. It is seen that all the three methods give positive slopes of this trend so it seems that the LFC module correcting the dead time 'over-corrects' a bit (3–6 ‰) the counts losses. The performance of the summation methods at high levels of background was verified by artificial channel-by-channel addition of a various constant values to the 3.05 % dead time spectrum. Identical peak areas were obtained from all such spectra using every method; the errors of areas for each method increased in the same manner as seen in Tab. 9. Thus the trends can be ascribed to the dead time and pile-up effects and to the LFC correction module itself.

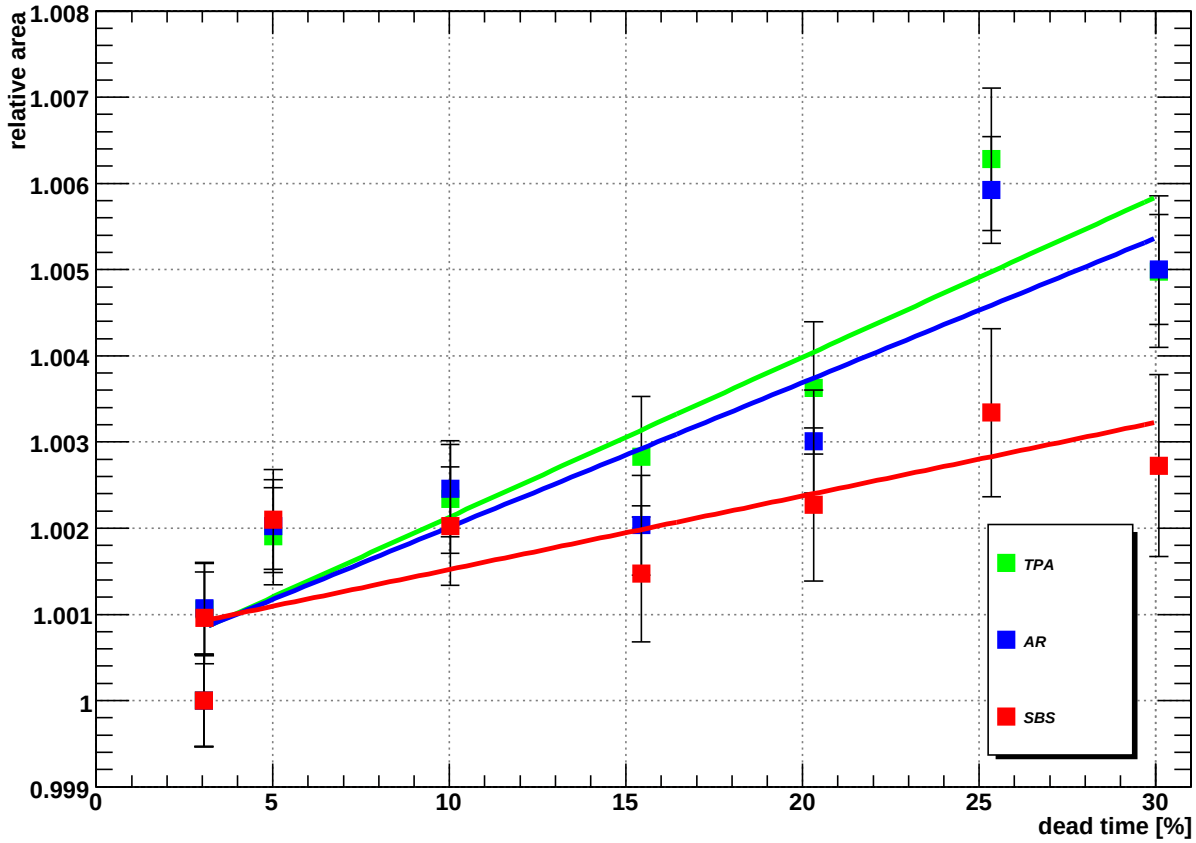

Fig. 27. TS2 results of TPA, AR and SBS methods. The peak areas normalized to the 3.05 % dead time spectrum peak area are shown in dependence on the dead time. The fit with linear function is also shown.

5.3 ^{83}Rb release investigation

5.3.1 ^{83}Rb spectra

The ^{83}Rb decay scheme is shown in Fig. 4. For the analysis of the release the three strongest gamma ray lines were used: 520.39(1), 529.635(9) and 552.63(2) keV with gamma transition intensities of 44.7(22), 29.3(13) and 16.0(7) % per decay [9], respectively. A detail of the ^{83}Rb spectrum with these lines is depicted in Fig. 28.

The ^{83}Rb spectra were measured with the detector setup described in Sect. 5.1. The ^{83}Rb sources in holders were always placed on a thin plastic lid covered with a clean paper. The plastic tube with well-defined length fixed the constant distance between the lid, *i.e.* the source, and the detector end cap. A set of tubes of length 33, 93, 173 and 400 mm was available. Firstly the geometry was set appropriately for the first measurement of a given fresh source to obtain reasonable number of counts per second. Then this 'first' geometry was always kept the same for any further measurement of the given source. As the source activity was decreasing with time, higher exposure times were then set to obtain sufficient statistics.

Within one day, usually several spectra were measured with a given source—this one day series will be further designated as one 'point'. When one spectrum was stored, the geometry

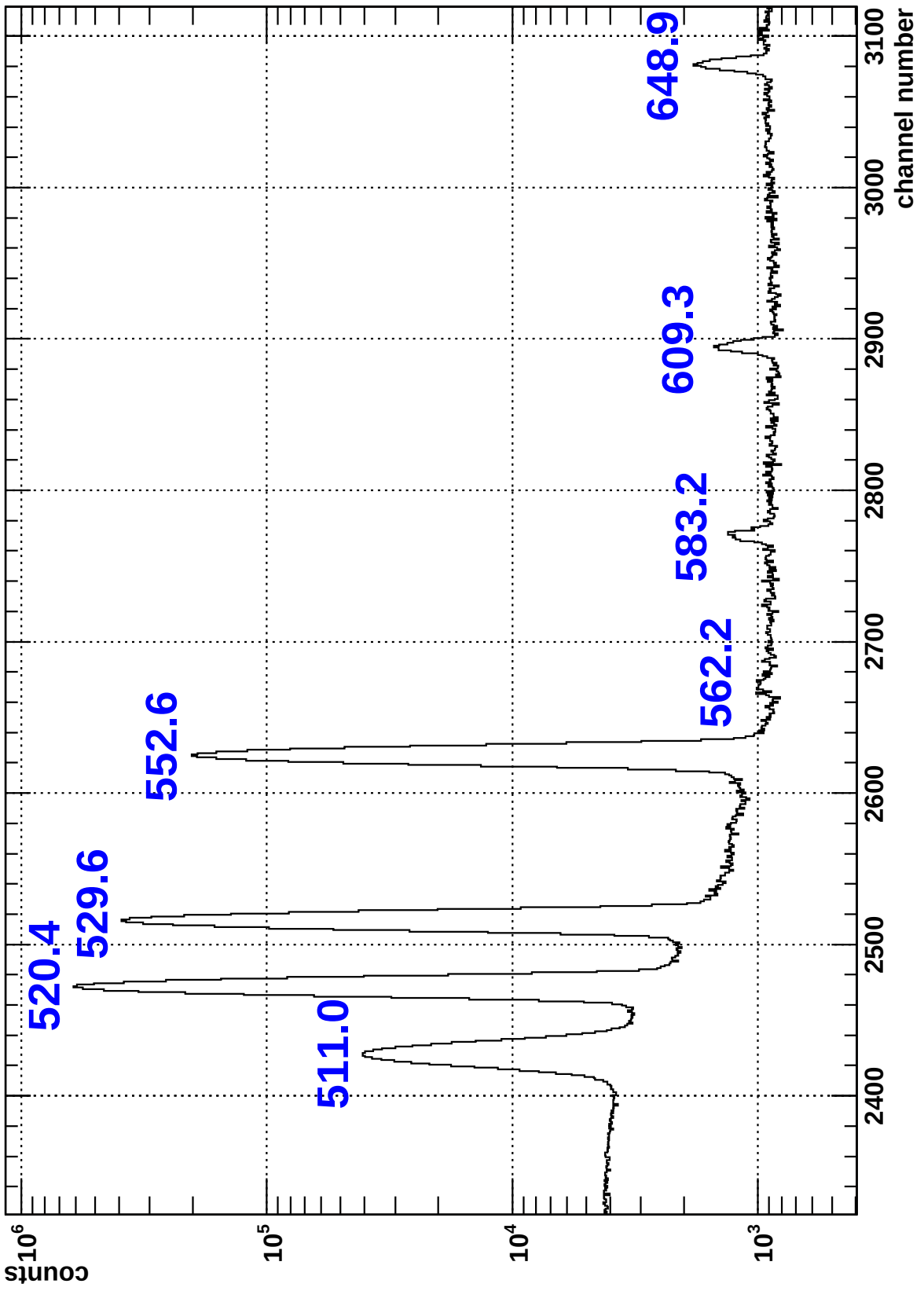

Fig. 28. Detail of the ^{83}Rb spectrum with the three gamma ray lines 520.4, 529.6 and 552.6 keV utilized for the ^{83}Rb release investigation. The peak with energy of 511.0 keV represents the gamma rays induced by positron annihilation. Further, the weak lines 562.2 (^{83}Rb), 583.2 (^{208}Tl), 609.3 (^{214}Bi) and 648.9 keV (^{83}Rb) are visible.

was 'destroyed', set again and the source was positioned on the center mark of the paper. The mutual comparison of such spectra allowed us to exclude from the analysis that measurement which would show some rough discrepancy, possibly due to the source accidentally not well aligned, with the other measurements performed within one point. With the help of Monte Carlo simulations it was shown [82] that the uncertainty caused by the shift of 3 mm off the detector axis of the source placed in the position of 33 mm from the detector is 7.4(4) ‰. Similar shift of 1 mm would cause the uncertainty of 0.9(4) ‰. From simple geometrical considerations ($1/r^2$ law) it follows that a vertical shift of 0.1 mm of the 33 mm 'source–detector' distance can cause the relative difference of the radiation intensities of up to 3.2 ‰.

The application of the TPA and AR summation methods (Sect. 5.2.2) to the ^{83}Rb peaks was straightforward - necessary ranges of channels were carefully set in such a way that the tailings of one peak did not interfere the ranges of summation or background approximation of the other one. The easiest situation was in the case of the third, 552 keV peak which is well separated from the other two peaks. The second 529 keV peak adjoins the 520 keV peak and the strongest 520 keV peak then lies between 511 and 529 keV peaks so some care had to be taken here. Before any summation the fits of the central Gaussian parts of the three peaks in question were carried out in order to obtain the approximate centroid and width values of the peaks. The maximum shift of the peak positions between any of all the ^{83}Rb spectra was about 3 channels. Subsequently the summation regions and background approximation regions (AR method) were set by appropriate numbers of channels about the peaks positions, preventing the interference of the individual peaks by each other or by the 511 keV peak. For the TPA method the n_B number of 'background channels' was fixed to 4 for 520 and 529 keV peaks and to 8 for 552 keV for all the spectra.

The SBS method (Sect. 5.2.3) was applied to three ^{83}Rb peaks in a similar manner as in the case of a single peak. After the subtraction of the background fitted on the high energy side of the third 552 keV peak three independent fits of the 'constant + step' functions were carried out, using the same background regions as the AR method (see Fig. 29). The assumption that after the background subtraction the peaks 520 and 529 keV lie on the constant background produced by the step associated to the third 552 keV peak was slightly disturbed.

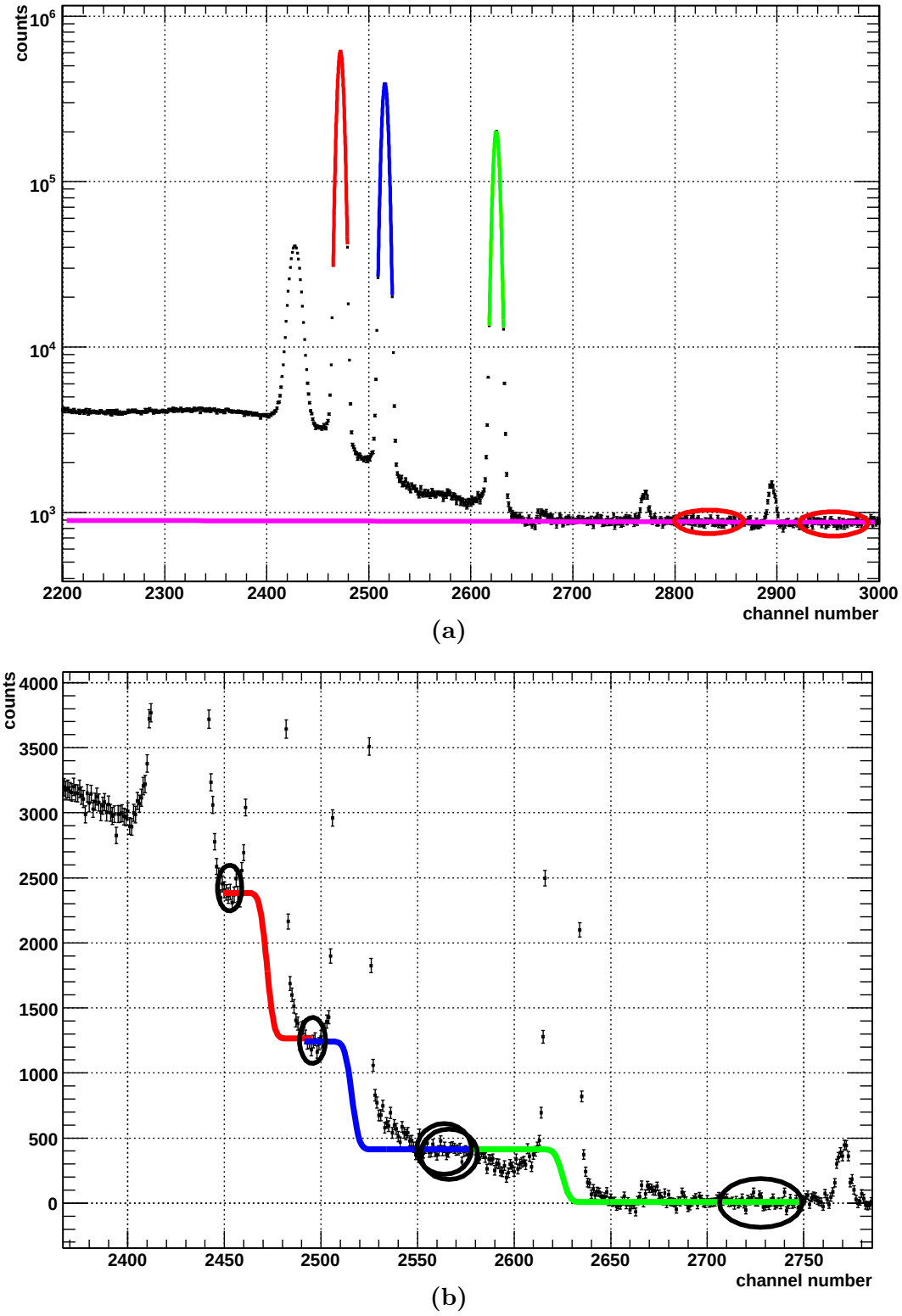

Fig. 29. Application of the SBS approach to ^{83}Rb spectrum. **(a)** The background on the high energy side of the 552 keV peak is fitted with a linear function, ellipses indicate the data ranges used for this fit. The magenta line shows the background, underlying all the peaks, to be subtracted. Red, blue and green lines shows the initial fits with Gaussian functions. **(b)** Three independent fits after the background subtraction are carried out, red line indicates the total function for 520, blue for 529 and green for 552 keV peak, respectively. Ellipses again show the data regions used. The two overlapping ellipses between the 529 and 552 keV peaks mean that the appropriate data ranges are differing by several channels.

5.3.2 Release calculation

The ^{83}Rb release calculation was divided into the following individual steps. The errors of all quantities were calculated in accordance with an error propagation law.

1. The net peak areas were determined with the help of three independent methods whose maximum relative errors are summarized in Tab. 10.

Tab. 10. Maximum relative uncertainties in ‰ of all areas determined by the summation methods applied to ^{83}Rb spectra.

	520 keV	529 keV	552 keV
TPA	3.9	4.8	6.6
AR	3.8	4.7	6.5
SBS	4.0	4.7	6.5

However, the values stated in Tab. 10 refer to the measurements within one point of the source S9 which were obtained with the exposure time of only 5 minutes. All the other exposure times were set as 10, 20, 30, 60 or 240 minutes, respectively, thus the appropriate maximum relative errors of all the other areas were considerably smaller, by a factor of 1.4–6.9. In addition, the peak areas within one point have shown some scatter which has exceeded the individual errors of the values in the majority of cases. This was reflected by higher values of the ratio $\overline{\sigma}^{\mathrm{w}}_{\mathrm{sc}}/\overline{\sigma}^{\mathrm{w}}_{\mathrm{err}}$. The error of weighted mean for the point was taken as the larger one of the two errors $\overline{\sigma}^{\mathrm{w}}_{\mathrm{sc}}$, $\overline{\sigma}^{\mathrm{w}}_{\mathrm{err}}$.

The maximum value of error ratios, *i.e.* the maximum χ^2_{norm} value was 2.4 (three measurements in one point in this worst case). According to the χ^2-test [83] the maximum value allowed for 95 % C.L. in the case of 3 degrees of freedom is 2.0. Thus when the value $\chi^2_{\mathrm{norm}} > 2.0$ was encountered, the spectrum causing the discrepancy was rejected. This effect was probably caused by the unideal reproducibility of the conditions for the individual measurement.

2. For the sake of clarity firstly the results from only one spectrum measured in the frame of one point are considered for this moment. The measurement of a given spectrum was started at some moment t_0 and lasted for the exposure time T_l. The detector load was indicated by the AccuSpec **d**ead time T_d. The output of the summation methods are the values of peak areas together with their errors, A_i and $\sigma(A_i)$, where $i = 1, 2, 3$ stands for the individual ^{83}Rb peaks.

3. The values of peak areas per unit time, B_i, are calculated as

$$B_i = \frac{Ex}{Dt}\,\frac{A_i}{T_l}\,, \tag{50}$$

where the factor

$$Ex = \frac{1 - \exp(-\lambda T_l)}{\lambda T_l}\,, \quad \lambda = \frac{\ln 2}{T_{1/2}} \tag{51}$$

is included in order to take the continuous decay of the ^{83}Rb source into account for long **ex**posure times and the term

$$Dt = k_d\, T_d + q_d \tag{52}$$

accounts for the imperfect instrumental **d**ead **t**ime correction and possibly the pile-up effect. The values k_d and q_d are taken from Tab. 9 for each summation method. The half-life $T_{1/2}$ of ^{83}Rb is known [9] as 86.2(1) d thus with the relative error $\eta\left(T_{1/2}\right) = 1.2\,‰$. This half-life error is taken into account throughout the whole calculation.

4. Actually, within one point not just one but several spectra were measured. Thus the output of the summation methods is actually $A_i^{(p,s)}$, $\sigma(A_i^{(p,s)})$, $i = 1, 2, 3$, where (p, s) stands for '(**p**oint, **s**pectrum)'. The other quantities are then $T_l^{(p,s)}$, $T_d^{(p,s)}$ and $t_0^{(p,s)}$ and through the relations above one gets $B_i^{(p,s)}$ with $\sigma(B_i^{(p,s)})$, $i = 1, 2, 3$.

5. To use the data of all the spectra of one point, the second and the other spectra have to be related to the time $t_0^{(p,1)}$ of the first spectrum of the point. In order to do so the time **int**ervals $t_{\mathrm{int}}^{(p,s)} = t_0^{(p,s)} - t_0^{(p,1)}$ are calculated and while $B_i^{(p,1)}$ remains the same, $B_i^{(p,s)}, s > 1$, change to
$$B_i^{(p,s*1)} = B_i^{(p,s)} \exp\left(\lambda\, t_{\mathrm{int}}^{(p,s)}\right) . \tag{53}$$

6. From the values $B_i^{(p,1)}$ and $B_i^{(p,s*1)}$, $s > 1$, the **w**eighted mean $W_i^{(p)}$ with error $\sigma(W_i^{(p)})$ is then calculated.

7. Further, for each i, *i.e.* for each ^{83}Rb gamma line, the values $W_i^{(p)}$, $p > 1$, are **n**ormalized to the relevant values of the first point $p = 1$: $W_i^{(1)} \to N_i^{(1)} \equiv 100\%$,
$$N_i^{(p)} = \frac{W_i^{(p)}}{W_i^{(1)}}\, 100\,, \quad p > 1\,. \tag{54}$$

8. Subsequently the normalized values $N_i^{(p)}$ are weighted over i (gamma **l**ines) getting $L^{(p)}$ and $\sigma(L^{(p)})$, $p \geq 1$.

9. The time **int**erval between points, $t_{\mathrm{int}}^{(p)} = t_0^{(p,1)} - t_0^{(1,1)}$, is used to calculate the expected ratio of $L^{(1)} \equiv 100\,\%$ in accordance to the law of **r**adioactive decay,
$$R\left(t_{\mathrm{int}}^{(p)}\right) = 100 \exp\left(-\lambda\, t_{\mathrm{int}}^{(p)}\right) . \tag{55}$$
It should be noted that the precision of this expected ratios is directly influenced (limited) by the accuracy $\sigma(L^{(1)})$ of the first measured point $L^{(1)}$.

10. For each point p the values $L^{(p)}$, $\sigma\left(L^{(p)}\right)$ are compared with $R\left(t_{\mathrm{int}}^{(p)}\right)$, $\sigma\left(R\left(t_{\mathrm{int}}^{(p)}\right)\right)$, and the positive **d**ifference
$$D^{(p)} \equiv R\left(t_{\mathrm{int}}^{(p)}\right) - L^{(p)} \stackrel{?}{>} 0\,, \quad p > 1 \tag{56}$$
indicates the ^{83}Rb release. Negative difference is meaningless, however, due to various uncertainties included in the measurements and calculations, the case of $D^{(p)} < 0$, $p > 1$, can also result.

The final ^{83}Rb release values calculated for sources S4–S9 are summarized in Tab. 11 and depicted in Fig. 30. Within one standard deviation ($1\,\sigma$, 68 % C.L.) all the points except one are compatible with zero release. The only exception is the last third point of source S4. However, this could be caused by some slight accidental 'wipe off' of the sample during the manipulation.

Tab. 11. Results of the calculation of ^{83}Rb release [%] for all the sources S4–S9.

	TPA		AR		SBS			TPA	AR	SBS	TPA		AR		SBS	
t_{int} [d]	meas.	σ	meas.	σ	meas.	σ	expec.	σ	σ	σ	diff.	σ	diff.	σ	diff.	σ
S4: 0.317 MBq (ref. date 10.6.2005), first meas. date 10.6.2005																
0	100.00	0.10	100.00	0.10	100.00	0.10	100.00	0.10	0.10	0.10	0.00	0.14	0.00	0.14	0.00	0.14
transport to IP Mainz on air, in UHV of $\simeq 8 \times 10^{-9}$ *mbar of the* β *spectr. source part for* $\simeq 10$ *days, transport back*																
194	21.07	0.07	21.06	0.07	21.05	0.06	21.03	0.04	0.04	0.04	-0.05	0.08	-0.04	0.08	-0.02	0.07
on air																
227	15.90	0.02	15.89	0.02	15.87	0.03	16.12	0.04	0.04	0.04	0.22	0.04	0.23	0.04	0.25	0.05
S7: 0.513 MBq (ref. date 18.10.2005), first meas. date 25.10.2005																
0	100.00	0.28	100.00	0.27	100.00	0.27	100.00	0.28	0.27	0.27	0.00	0.39	0.00	0.38	0.00	0.39
in high vacuum of $\simeq 2 \times 10^{-6}$ *mbar of the* β *spectr. ESA 12 at NPI Řež/Prague for about 30 days*																
31	77.87	0.11	77.70	0.09	77.82	0.11	78.08	0.22	0.21	0.22	0.20	0.24	0.38	0.23	0.26	0.24
S8: 4.5 MBq (ref. date 29.11.2005), first meas. date 1.12.2005																
0	100.00	0.10	100.00	0.09	100.00	0.10	100.00	0.10	0.09	0.10	0.00	0.14	0.00	0.13	0.00	0.14
in high vacuum of $\simeq 2 \times 10^{-6}$ *mbar of the* β *spectr. ESA 12 at NPI Řež/Prague for about 48 days*																
48	67.938	0.07	67.80	0.05	67.79	0.05	67.86	0.08	0.07	0.07	-0.08	0.10	0.06	0.09	0.07	0.09
on air																
63	60.13	0.02	60.21	0.02	60.16	0.02	60.24	0.07	0.07	0.07	0.11	0.07	0.03	0.07	0.07	0.07
in high vacuum of $\simeq 2 \times 10^{-6}$ *mbar of the* β *spectr. ESA 12 at NPI Řež/Prague for about 47 days*																
110	41.21	0.02	41.27	0.02	41.23	0.02	41.21	0.06	0.06	0.06	0.01	0.06	-0.05	0.06	-0.02	0.06
S9: 2.1 MBq (ref. date 17.2.2006), first meas. date 17.2.2006																
0	100.00	0.07	100.00	0.06	100.00	0.07	100.00	0.07	0.06	0.07	0.00	0.10	0.00	0.08	0.00	0.09
alternately on air and in high vacuum of $\simeq 2 \times 10^{-6}$ *mbar*																
28	79.85	0.03	79.93	0.05	79.78	0.03	79.84	0.06	0.05	0.06	-0.02	0.07	-0.10	0.07	0.05	0.07

Columns from left to right: 1) time intervals in days passed from the first measurement of the given source; values and standard deviations of the peak areas per unit time normalized to the first measurement values, obtained via 2,3) TPA, 4,5) AR and 6,7) SBS methods; expected equivalent ratios 8) calculated according to the law of radioactive decay; its standard deviation deduced from the experimental error of the first measurement of the given source processed by 9) TPA, 10) AR and 11) SBS method; the differences between the expected and measured quantities stated with errors of one standard deviation for 12,13) TPA, 14,15) AR and 16,17) SBS methods, respectively. The situation of the source between the measurements is marked in italic.

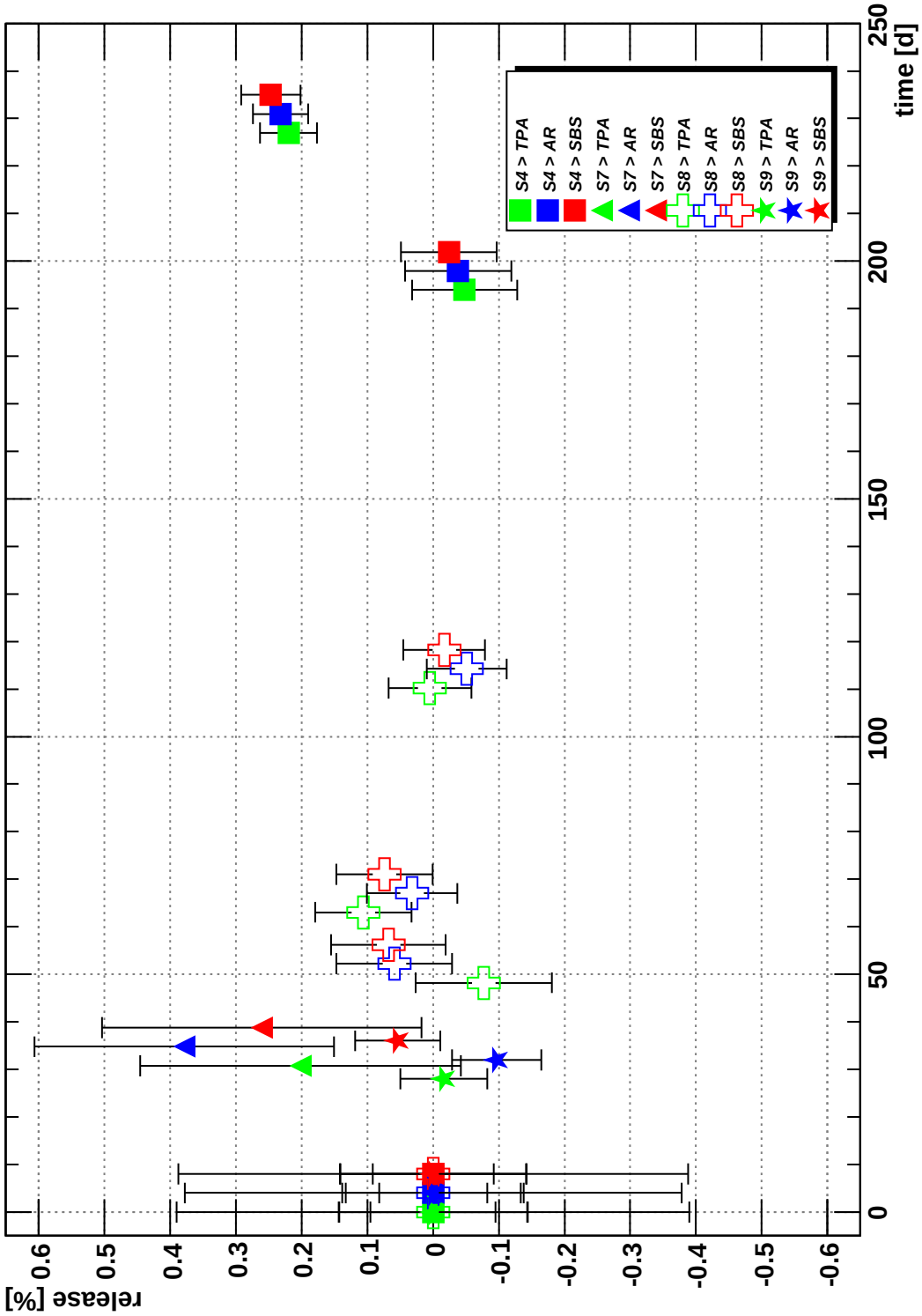

Fig. 30. The final values of the ^{83}Rb release [%] calculated for four ^{83}Rb sources S4–S9 with the help of three methods TPA, AR and SBS, for the details of calculation see text, error bars represents one standard deviation. Source S4 values are indicated by squares, S7—triangles, S8—crosses and S9—stars. TPA method—green, AR—blue and SBS—red color. The x-axes show the time interval passed from the first measurement of each source, the lower one in seconds and the upper one in days. The y-axis indicates the ^{83}Rb release of each source where the total of 100 % is taken as the value obtained from the first measurement. For clarity the values obtained by the AR and SBS methods are displayed shifted by some small fixed amount of time though they refer to the same 'moment'. At point [0, 0] all the sources have their 'original' zero release thus all the markers are superposed here.

6 Conclusion

The aim of this work was to investigate the **u**ltra**h**igh **v**acuum (UHV) stability of the solid ^{83}Rb/^{83m}Kr source being developed for neutrino experiment KATRIN for the monitoring purposes.

Firstly, the second residual gas analysis measurements of non-radioactive Rb samples were carried out and analyzed at JINR Dubna in winter 2005/2006. Their reliability was much better when compared to the previous measurement series thanks to the more proper settings of the operating parameters. From the analysis of mass spectra it was found that no effect, *i.e.* no Rb signal has been observed even with the optimum settings. Such a result indicate that the intended vacuum evaporated ^{83}Rb/^{83m}Kr source could also be stable in UHV conditions.

Secondly, after the vacuum evaporated ^{83}Rb/^{83m}Kr sources were available the ^{83}Rb release was studied by means of gamma spectroscopy. Altogether 4 sources were inspected and one of them even for the period of 7 months. The sources were stored on air and in high vacuum (in ESA 12 spectrometer where the electron spectra were measured), one of them was also in UHV (Mainz spectrometer) for 10 days.

From the gamma measurement of the source activities it was concluded that the release of ^{83}Rb was compatible with zero in the frame of one standard uncertainty. The typical relative standard uncertainty of the activities amounted to 2 ‰. Further improvement of the precision can be achieved only after dedicated experiment studying the systematic error coming from the unideal reproducibility of the conditions for the individual measurement. Actually, the current results comprise only one application of the ^{83}Rb/^{83m}Kr source in UHV condition. This imperfection will be solved in near future as the UHV chamber will be moved from JINR Dubna to NPI Řež/Prague.

The behavior of the open ^{83}Rb/^{83m}Kr source in UHV condition is of high importance for the concept of monitoring in KATRIN experiment. For the detailed investigation of this issue various surface analysis methods could be also utilized, however, only two main goals have to be achieved: the UHV compatibility of the ^{83}Rb/^{83m}Kr source itself and the long-term stability of the ^{83m}Kr conversion electron lines intended for the continuous monitoring of the KATRIN energy scale. This diploma thesis represents the first results as for the source UHV compatibility. Both problems will be further investigated at NPI Řež/Prague.

References

[1] J. Angrik, T. Armbrust *et al.* (KATRIN collaboration), *KATRIN Design Report 2004*, `http://www-ik.fzk.de/~katrin`, 2005.

[2] K. Zuber, *Neutrino Physics*, IOP Publishing Ltd., 2004.

[3] A. Picard, H. Backe *et al.*, Zeit. Phys. **A342**(1992)71.

[4] W. Stoeffl and D.J. Decman, Phys. Rev. Lett. **75**(1995)3237.

[5] D. Vénos, O. Dragoun *et al.*, Nucl. Instr. and Meth. **A560**(2006)352.

[6] O. Dragoun, A Špalek and F.J. Wuilleumier, Czech. J. Phys. **54**(2004)833.

[7] R.G. Helmer and C. van der Leun, Nucl. Inst. Meth. **A450**(2000)35.

[8] R.D. Deslattes, E.G. Kessler, Jr. *et al.*, Rev. Mod. Phys. **75**(2003)35.

[9] R.B. Firestone, V.S. Shirley *et al.*, *Table of Isotopes 8th Edition*, John Wiley & Sons, New York, 1996 (see also LBNL and LUNDS Universitet Isotopes Project, *WWW Table of Radioactive Isotopes*, `http://ie.lbl.gov/toi`, 2004).

[10] W.F. Egelhoff, Jr., Surf. Sci. Rep. **6**(1987)253.

[11] A. Kovalík, V.M. Gorozhankin *et al.*, J. Elec. Spec. Rel. Phenom. **58**(1992)49.

[12] A. Kovalík and V.M. Gorozhankin, J. Phys. **G19**(1993)1921.

[13] A. Roth, *Vacuum Technology*, Elsevier, Amsterdam, 1998.

[14] J.A. Venables, Surf. Sci. **299/300**(1994)798.

[15] O. Dragoun, Department of Nuclear Spectroscopy, Nuclear Physics Institute, ASCR, private communication, 2006.

[16] M. Vobecký, Department of Trace Element Analysis, Institute of Analytical Chemistry, ASCR, private communication, 2005–2006.

[17] R.E. Honig and D.A. Kramer, RCA Review **30**(1969)285.

[18] M.J. Winter, WebElements™ Periodic Table, `http://www.webelements.com`, 2006.

[19] N.N. Greenwood and A. Earnshaw, *Chemistry of the Elements*, Pergamon Press, Oxford, 1984.

[20] BAL-TEC AG., *Products Overview, Technical Data and Operating Manuals*, `http://www.bal-tec.com`, 2006.

[21] Z. Herman, Department of Chemical Physics, J. Heyrovský Institute of Physical Chemistry, ASCR, private communication, 2003–2004.

[22] Gmelins Handbuch Der Anorganischen Chemie, *Rubidium* (System-Num. 24), Verlag Chemie, Berlin, 1937, in German.

[23] J. Kašpar, Department of Nuclear Spectroscopy, Nuclear Physics Institute, ASCR, private communication, 2006.

[24] NIST Chemistry WebBook, *NIST Standard Reference Database Number 69*, `http://webbook.nist.gov/chemistry`, June 2005.

[25] M. Binnewies and E. Milke, *Thermochemical Data of Elements and Compounds*, WILEY-VCH, Weinheim, 1999.

[26] A.M. James and M.P. Lord, *Chemical and Physical Data*, Macmillan Press, London, 1992.

[27] G. Aylward and T. Findlay, *SI Chemical Data*, John Wiley & Sons, Milton, 1994.

[28] R.H. Perry (Ed.), *Perry's Chemical Engineers' Handbook*, McGraw-Hill, New York, 1998.

[29] J.H. Gross, *Mass Spectrometry – A Textbook*, Springer Verlag, Heidelberg, 2004.

[30] P.H. Dawson (Ed.), *Quadrupole Mass Spectrometry and its Applications*, Elsevier, Amsterdam, 1976.

[31] Pffeifer Vacuum, Inc., *Mass spectrometer 2005–2007*, `http://www.pfeiffer-vacuum.com`, 2005.

[32] Pfeiffer Vacuum, Inc., *Products Overview, Technical Data and Operating Manuals*, `http://www.pfeiffer-vacuum.com`, 2002.

[33] Stanford Research Systems, Inc., *RGA100/200/300 Operating Manual*, `http://www.thinkSRS.com`, 2005.

[34] N. Müller, *Tutorials on Quadrupole Mass Spectrometry Basics*, `http://www.qmg700.com/quadinfo`, 2004.

[35] N.R. Reagan, L.C. Frees and J.W. Gray, J. Vac. Sci. Technol. **A5**(1987)2389.

[36] J.R. Gibson, S. Taylor and J.H. Leck, J. Vac. Sci. Technol. **A18**(2000)237.

[37] J.A. Basford, M.D. Boeckmann *et al.*, J. Vac. Sci. Technol. **A11**(1993)A22.

[38] P.R. Stuart, Vacuum **45**(1994)889.

[39] A.C.C. Voo, R. Ng *et al.*, J. Vac. Sci. Technol. **A15**(1997)2276.

[40] P. Řepa, J. Tesař *et al.*, J. Mass Spectrom. **37**(2002)1287.

[41] N. Müller, Vacuum **44**(1993)623.

[42] J.H. Batey, Vacuum **43**(1992)15.

[43] P.A. Redhead, Vacuum **12**(1962)203.

[44] J.P. Hobson, J. Vac. Sci. Technol. **A21**(2003)S7.

[45] J.P. Adrados and J.L. de Segovia, Vacuum **34**(1984)737.

[46] J.L. de Segovia, Vacuum **47**(1996)333.

[47] F. Watanabe, J. Vac. Sci. Technol. **A20**(2002)1222.

[48] S. Kurokouchi and S. Kato, J. Vac. Sci. Technol. **A19**(2001)2820.

[49] J.R.J. Bennett and R.J. Elsey, Vacuum **44**(1993)647.

[50] T. Jirsák and V. Nikolajenko, Vacuum **47**(1996)173.

[51] J.R.J. Bennett, S. Hughes *et al.*, Vacuum **73**(2004)149.

[52] S. Kurokouchi, S. Watanabe and S. Kato, Vacuum **47**(1996)763.

[53] M.G. Rao and C. Dong, J. Vac. Sci. Technol. **A15**(1997)1312.

[54] L. Lieszkovszky, A.R. Filippelli and C.R. Tilford, J. Vac. Sci. Technol. **A8**(1990)3838.

[55] W.E. Austin and J.H. Leck, Vacuum **41**(1990)2001.

[56] P. Turner, S. Taylor *et al.*, Trends Anal. Chem. **23**(2004)281.

[57] J.A. Basford, J. Vac. Sci. Technol. **A9**(1991)1991.

[58] A. Breth, R. Dobrozemsky and B. Kraus, Vacuum **33**(1983)73.

[59] L. Lieszkovszky and J. Borossay, J. Vac. Sci. Technol. **A5**(1987)2819.

[60] Vakuum Praha Co., *Products Overview and Technical Data*, `http://www.vakuum.cz`, 2005.

[61] R. Bašta and P. Kvita, Vakuum Praha Co., private communication, 2003–2006.

[62] P. Řepa, Department of Electronics and Vacuum Physics, Faculty of Mathematics and Physics, Charles University in Prague, private communication, 2003–2005.

[63] U.R. Bance and R.D. Craig, Vacuum **16**(1966)647.

[64] K. Jousten and D. Li, Vacuum **70**(2003)531.

[65] SPI Supplies – Structure Probe, Inc., *HOPG Substrate Material Overview*, `http://www.2spi.com`, 2004.

[66] Z. Hůlek, Pfeiffer Vacuum Austria GmbH, Branch Office Prague, private communication, 2006.

[67] J. Kubáň and K. Mokeš, Pfeiffer Vacuum Austria GmbH, Service Office (Vakuum Servis Co.), Rožnov pod Radhoštěm, private communication, 2006.

[68] Pfeiffer Vacuum, Inc., *Test Report of the Quadrupole Mass Spectrometer Prisma™*, Product No. PT M03 321 121, Order No. 1029771, 2001.

[69] A. Kovalík, Laboratory of Nuclear Problems, JINR Dubna, private communication, 2003–2006.

[70] A.V. Lubashevsky and L.L. Perevoshchikov, Laboratory of Nuclear Problems, JINR Dubna, private communication, 2003–2006.

[71] ROOT, Object-Oriented Data Analysis Framework, `http://root.cern.ch`, 2006.

[72] V. Hnatowicz, *Handbook of Nuclear Data for Neutron Activation Analysis, Vol. 1 (Evaluation of Gamma-Ray Spectra)*, Czechoslovak Atomic Energy Commission, Prague, 1986.

[73] K. Debertin and R.G. Helmer, *Gamma- and X-Ray Spectrometry with Semiconductor Detectors*, North-Holland, Amsterdam, 1988.

[74] G.W. Phillips and K.W. Marlow, Nucl. Instr. and Meth. **137**(1976)525.

[75] R.G. Helmer and M.A. Lee, Nucl. Instr. and Meth. **178**(1980)499.

[76] L. Kokta, Nucl. Instr. and Meth. **112**(1973)245.

[77] P. Quittner, Nucl. Instr. and Meth. **76**(1969)115.

[78] J. Hertogen, J. De Donder and R. Gijbels, Nucl. Instr. and Meth. **115**(1974)197.

[79] G. Kennedy, Nucl. Instr. and Meth. **A299**(1990)349.

[80] D. Vénos, Department of Nuclear Spectroscopy, Nuclear Physics Institute, ASCR, private communication, 2003–2006.

[81] G.F. Knoll, *Radiation Detection and Measurement*, John Wiley & Sons, New York, 2000.

[82] A. Špalek, Department of Nuclear Spectroscopy, Nuclear Physics Institute, ASCR, private communication, 2006.

[83] I.N. Bronshtein, K.A. Semendyayev *et al.*, *Handbook of Mathematics*, Springer Verlag, Heidelberg, 2004.